

Novel Nanoparticle-based Signal Transducers for Improved Sensitivity of Lateral Flow Immunoassays

Dissertation

zur Erlangung des
Doktorgrades der Naturwissenschaften (Dr. rer. nat.)

Der

Naturwissenschaftlichen Fakultät I – Biowissenschaften
der
Martin-Luther-Universität Halle-Wittenberg

vorgelegt von

Herrn Moritz Schüller
geboren am 10.04.1991 in Dresden

Gutachter:

Prof. Dr. Lea Ann Dailey

Prof. Dr. Mark Green

Prof. Dr. habil. Thomas Groth

Öffentlich verteidigt in Halle (Saale) am 05.11.2021

„Die Lippen der Weisheit sind verschlossen, nur nicht für die Ohren des Verständnisses.“

Aus dem Kybalion

Meiner Familie gewidmet.

Zusammenfassung

Wie in der kürzlich aufgetretenen COVID-19-Pandemie zu sehen war, sind Infektionskrankheiten eine andauernde Bedrohung für die persönliche Gesundheit und die Menschheit selbst. Ein Schlüssel zur Bekämpfung von Krankheiten ist die rechtzeitige Identifikation von Infektionen. Der günstigste und schnellste Test ist heutzutage das Lateral-Flow-Immunoassay (LFI). Jedoch ist die Empfindlichkeit dieser Tests im Vergleich zu laborbasierten Methoden gering. Daher war es die Hauptaufgabe dieser Arbeit, die Sensitivität von LFI zu verbessern. Kommerzielle LFI basieren üblicherweise auf der visuellen Interpretation einer farbigen Sonde. In neuerer Forschung wird die Empfindlichkeit durch Verwendung fluoreszierender Sonden oder Verstärkung des Farbsignals durch Farbstoffreaktionen erreicht, die durch die Sonde katalysiert werden.

Die erste Strategie zur Erhöhung der Sensitivität von LFI in dieser Arbeit war die Verbesserung fluoreszenter Sonden. Konjugierte Polymere (CP) sind fluoreszierende Farbstoffe mit vielversprechenden optischen Eigenschaften. Daher wurden zwei verschiedene CP, PDOF und CN-PPV, entweder einzeln oder als Polymerblend, in Nanopartikeln (NP) verkapselt und als fluoreszierende Sonden in LFI verwendet. Zwei verschiedene Verkapselungssysteme, Si-NP und Pdots, wurden auf ihre physikochemischen und optischen Eigenschaften hin untersucht. Kaninchen IgG, als ein Modell-Antikörper (Ab), wurden mit den CP-NP verbunden und mit kommerziellen NP mit niedermolekularem Fluoreszenzfarbstoff (PS-NP) und kolloidalem Gold (Au-NP) in einem ELISA-artigen Test verglichen. Das Signal-Hintergrund-Verhältnis (SBR) war für Si-NP wesentlich höher, als für PS-NP und Au-NP und sogar nochmals höher für Pdots.

Anschließend wurden Parameter des LFI für jedes NP-System individuell optimiert. Jedoch war die Freisetzung der NP von dem Konjugat-Pad ungleichmäßig. Daher wurden die Ab-NP-Konjugate in einem Dipstick-LFI-Format untersucht. Die detektierbare Masse an Pdots war zwei Größenordnungen geringer, als bei den anderen NP-Systemen. Das SBR der CN-PPV-Pdots war dreimal so hoch, wie das der PDOF-Pdots und wurde nur durch das der PDOF-CN-PPV-Pdots übertroffen. Um die Konzeptstudie auf eine anwendungsnahe Problemstellung zu übertragen, wurden anti-Tetracyclin-, anti-*Staphylococcus aureus* Enterotoxin A- und anti-herzstämmiges fettsäurebindendes Protein IgG an Pdots und Au-NP gebunden. Leider zeigte keiner der Ab Immunbindung in Dipstick LFI.

Als zweite Strategie zur Erhöhung der Empfindlichkeit von LFI wurden neue Nanokatalysatoren für farbreaktionsverstärkte LFI (eLFI) untersucht. NP auf Basis von multikationischen Materialien (MCM) und hochentropie-Nanomaterialien (HEN) wurden von Kooperationspartnern bereitgestellt. Die katalytische Aktivität der Verbindungen wurde anhand der Oxidationsreaktion zweier Farbstoffe, TMB und DAB, quantifiziert und mit Fe_3O_4 verglichen, welches als in eLFI verwendbar publiziert wurde. Die fünf Materialien höchster Aktivität wurden mit Kaninchen IgG verbunden und die katalytische Aktivität als Suspension und in ELISA untersucht. Überraschenderweise zeigten alle MCM und HEN verringerte Aktivität nach der Ab-Bindung. Es stellte sich heraus, dass katalytisch aktive Bestandteile von der NP Oberfläche gelöst und während der Aufbereitung der Ab-Konjugate entfernt wurden. Laufende Studien werden zeigen, unter welchen Bedingungen MCM und HEN optimale katalytische Aktivität zeigen.

Abstract

Infectious diseases, like seen in the recent COVID-19 pandemic, are a constant threat for the personal health and mankind itself. A key to fight diseases is the early identification of illness or infection. The most inexpensive and rapid point-of-care test today is the lateral flow immunoassay (LFI). However, the sensitivity of these tests is low compared to lab-based methods. Therefore, the main objective of this thesis was to improve the sensitivity of LFI. Commercial LFI are commonly based on visual interpretation of a colored probe. In recent research, increased sensitivity was achieved by utilisation of fluorescent signal transducers or enhancement of the colorimetric signal by dye reactions that are catalysed by the NP probe.

The first strategy for increased LFI sensitivity was the improvement of fluorescent signal transducers. Conjugated polymers (CP) are fluorescent dyes with promising optical properties. Thus, two different CP, PDOF and CN-PPV, were encapsulated in nanoparticles (NP), either alone or as polymer blend and used as fluorescent probes in LFI. Two different encapsulation systems, Si-NP and Pdots, were evaluated for physicochemical and optical properties. The CP-NP were conjugated to rabbit IgG as model antibody (Ab) and compared to commercial small-molecule fluorescent dye NP (PS-NP) and colloidal gold (Au-NP) in an ELISA-like assay. The signal-to-background ratio (SBR) was much higher for Si-NP, compared to PS-NP and Au-NP and even higher for Pdots.

Successively, LFI parameters were optimised for each NP system. It was observed, that the NP release from the conjugate pad was inconsistent. Therefore, the Ab-NP conjugates were evaluated in a dipstick LFI format. The mass of Pdots necessary for detection was two orders of magnitude lower, compared to the other NP systems. The SBR of CN-PPV-Pdots was about three times higher, compared to PDOF-Pdots and only exceeded by PDOF-CN-PPV-Pdots. To transfer the proof-of-concept to real applications, Pdots and Au-NP were conjugated to anti-tetracycline-, anti-*staphylococcus aureus* enterotoxin A-, and anti-heart fatty acid binding protein IgG. Unfortunately, none of the Ab showed immunobinding in dipstick LFI.

As second strategy for improved sensitivity of LFI, novel nanocatalysts for dye-reaction enhanced LFI (eLFI) were evaluated. NP based on multi-cationic materials (MCM) and high-entropy-nanomaterials (HEN) were provided by collaborators. The catalytic activity of the compounds was quantified for oxidation of two dyes, TMB and DAB, and compared to Fe₃O₄, that was published to be applicable to eLFI. The five most active materials were then conjugated to rabbit IgG and the activity was assessed in dispersion and in an ELISA. Surprisingly, all MCM and HEN showed reduced activity after conjugation.

It was found that catalytically active components were solubilized from the NP surface and were washed away during the Ab conjugation workup. Ongoing studies will determine under which conditions MCM and HEN may show optimal catalytic activity.

Table of contents

Zusammenfassung	iv
Abstract.....	vi
Table of contents	viii
List of Figures	xii
List of Tables.....	xvii
List of Abbreviations.....	xviii
Chapter 1: Introduction	1
1.1 LFI	2
1.2 Fluorescent LFI.....	4
1.3 CP in LFI.....	6
1.4 Dye-reaction-enhanced LFI	8
1.5 Nanocatalysts as signal transducers in LFI	9
1.6 Study questions and aims of the thesis	10
Chapter 2: CP-based fluorescent nanoparticles: CP-NP optimisation, physicochemical characterisation and antibody conjugation.....	11
2.1 Introduction.....	12
2.1.1 Fluorescent signal transducer specifications for high sensitivity of LFI.....	12
2.1.2 CP-NP vs other fluorescent signal transducers in LFI.....	13
2.1.3 Dye loading and optical performance	15
2.1.4 NP size and surface properties	18
2.1.5 Surface modification with detection moieties	19
2.1.6 Study questions and hypotheses	22
2.2 Materials and Methods	23
2.2.1 Materials.....	23
2.2.2 Optical characterisation of CP in solvent (THF).....	23
2.2.3 Preparation, purification and product yield: Si-NP and Pdots	24
2.2.3.1 Carboxylation of Pluronic© F127	24
2.2.3.2 Si-NP preparation	24
2.2.3.3 Pdot preparation	25
2.2.4 Physicochemical characterisation: Si-NP, Pdots, PS-NP and Au-NP.....	25

2.2.5	Characterisation of optical properties: Si-NP, Pdots and PS-NP	25
2.2.6	Antibody conjugation: Si-NP, Pdots, PS-NP and Au-NP	26
2.2.6.1	Conjugation of Si-NP, Pdots and PS-NP	26
2.2.6.2	Adsorption of Ab to the Au-NP surface	26
2.2.7	LFI dipstick tests	26
2.2.8	Fluorescence-linked immunosorbent assay (FLISA) of IgG-NP-conjugates	27
2.3	Results and Discussion	28
2.3.1	Optical characterisation of CP in solvent (THF)	28
2.3.2	Si-NP production and optimisation	29
2.3.2.1	Synthesis and characterisation of F127-COOH	29
2.3.2.2	Si-NP production	31
2.3.2.3	Si-NP purification	33
2.3.3	Pdots production	34
2.3.4	Comparison of physicochemical properties: Si-NP, Pdots, PS-NP and Au-NP	35
2.3.5	Comparison of optical properties: Si-NP, Pdots and PS-NP	36
2.3.6	Optimisation of antibody conjugation conditions with CN-PPV-Pdots	39
2.3.7	Assessment of antibody conjugation (IgG) using FLISA: Si-NP, Pdots, PS-NP and Au-NP	40
2.4	Conclusion	41
Chapter 3: CP-based fluorescent nanoparticles as signal transducers in LFI: Preliminary investigations with the model proteins rabbit IgG and goat anti-rabbit IgG		43
3.1	Introduction	44
3.1.1	LFI structure and critical parameters	44
3.1.1.1	Choice of membrane	44
3.1.1.2	LFI geometry	45
3.1.2	Performance of fluorescent LFI in the literature	45
3.1.3	Detection and quantification methods	47
3.1.4	Advantages/disadvantages of fluorescent LFI	48
3.1.5	Target specifications of LFI, study questions and hypotheses	49
3.2	Materials and Methods	50
3.2.1	Materials	50
3.2.2	General LFI parameters: IgG	50
3.2.3	Comparison of NC membranes	50
3.2.4	Effect of running buffer composition	51
3.2.5	NP redispersion from conjugate pad	51
3.2.6	Dipstick assay with rabbit IgG	52

3.2.7	Conjugation of anti-tetracycline-, anti-SAE- and anti-hFABP IgG to CN-PPV-Pdots and Au-NP and assessment of NP.....	52
3.3	Results and Discussion	53
3.3.1	Comparison of NC membranes.....	53
3.3.2	Test line concentration and detection.....	54
3.3.2.1	Test line concentration optimization.....	54
3.3.2.2	Test line detection: Mobile phone and ImageJ versus LFIReader.....	55
3.3.3	Effect of running buffer composition.....	56
3.3.4	NP redispersion from conjugate pad.....	58
3.3.4.1	Pdots.....	58
3.3.4.2	Si-NP.....	59
3.3.5	Dipstick assay with rabbit IgG.....	60
3.3.6	Preliminary data with anti-tetracycline, anti-SAE and anti-hFABP IgG: Selected LFI and ELISA-like microplate assay results	62
3.3.6.1	Antibody conjugation to Pdots	62
3.3.6.2	Dipstick LFI with anti-tetracycline, anti-SAE and anti-hFABP IgG-CN-PPV-Pdots.....	63
3.3.6.3	ELISA-like microplate assay with anti-tetracycline, anti-SAE and anti-hFABP IgG-Au-NP	63
3.4	Conclusion.....	65
Chapter 4:	High-entropy nanozymes as colorimetric signal transducers in eLFI.....	67
4.1	Introduction.....	68
4.1.1	Nanozymes	68
4.1.2	Nanozymes in LFI	69
4.1.3	High-entropy materials: What are they?.....	71
4.1.4	High-entropy materials: Possible applications.....	72
4.1.5	High-entropy materials: Possible biomedical applications as nanozymes	73
4.1.6	Target specifications of NP, study questions and hypotheses.....	74
4.2	Materials and methods	75
4.2.1	Materials.....	75
4.2.2	Nanozyme preparation	75
4.2.3	Dispersion and physicochemical characterisation.....	75
4.2.4	Peroxidase-like activity of dispersions with different compositions	76
4.2.5	Antibody conjugation (rabbit IgG) to selected materials.....	77
4.2.6	ELISA performance	77
4.3	Results.....	78

4.3.1 Dispersion and physicochemical characterisation	78
4.3.2 Peroxidase-like activity of dispersions with different compositions	79
4.3.2.1 Peroxidase-like activity of dispersions of varying concentration.....	79
4.3.2.2 Intra and interday variability of peroxidase-like activity of MCM and HEN dispersions with different dispersant.....	82
4.3.2.3 Peroxidase-like activity of dispersions of same Fe(II) content.....	84
4.3.3 Antibody conjugation (rabbit IgG) to selected materials	85
4.3.3.1 Physicochemical properties of conjugates.....	86
4.3.3.2 Interday variability of peroxidase-like activity of selected dispersions of rabbit IgG-conjugated MCM and HEN	86
4.3.4 ELISA performance.....	87
4.3.4.1 Concentration-dependence of peroxidase-like activity of selected rabbit IgG- conjugated MCM and HEN bound in an ELISA	87
4.3.4.2 Interday variability of peroxidase-like activity of selected rabbit IgG- conjugated HEN bound in an ELISA.....	89
4.3.4.3 Batch-to-batch-variation of selected HEN.....	91
4.3.4.4 Troubleshooting: Understanding the catalytic activity at each processing step	92
4.3.5 Effect of dispersant on catalytic activity	94
4.4 Conclusion.....	96
Chapter 5: Summary and perspectives	97
5.1 Summary	98
5.2 Perspectives.....	100
Chapter 6: References	102
Acknowledgements	117
Curriculum vitae.....	118
Declaration of authorship.....	119

List of Figures

Figure 1: Schematic layout and working principle of an LFI. A sample containing an antigen is applied to a porous pad and wicked through a storage of signal transducers, forming an immunocomplex. The complex moves through an NC membrane by capillary force and is bound by antibodies adsorbed at the test line. Remaining signal transducer is bound by a secondary antibody fixed on the control line and excess liquid is wicked by an absorption pad.	2
Figure 2: Analytic principle of the sandwich (a) and the competitive (b) LFI.	3
Figure 3: Energy-core-distance-diagram of an electron, illustrating the process of fluorescence (a) and non-fluorescence relaxation mechanisms of the excited electronic state (b) including internal conversion (IC) from an excited singlet state (S_1) to the singlet ground state (S_0) or inter-system crossing (ISC) between singlet and triplet (T_1) states with following vibrational relaxation (VR) or phosphorescence (P). Bi-molecular relaxation processes are excluded for easy reading. Figures are based on W.-D. Stohrer, Die konzeptionellen und theoretischen Grundlagen der Photochemie, in: Photochemie, Wiley-VCH Verlag GmbH & Co. KGaA, Weinheim, FRG, 2005: pp. 43–64. https://doi.org/10.1002/3527603247.ch2	4
Figure 4: Conjugation of pi-bonds along the backbone of a CP (a) and the three generations of CP (b).	6
Figure 5: Principle of the eLFI. After lateral flow and immunosorption (1), a dye substrate is applied and the change of dye colour is catalysed by the signal transducer (2).	8
Figure 6: Energy transfer from excited PDOF to CN-PPV and subsequent fluorescence emission in a CP blend.	13
Figure 7: Overview of existing NP signal transducers in LFI. ⁶²	14
Figure 8: Brightness as function of loading dose, represented by the optical density at excitation wavelength, for $\Phi=1$ and $OD_{Em}=OD_{Ex}$ (solid line) or $OD_{Em}=0$ (segmented line), calculated with Equation 4 and tangent at $OD_{Ex}=0$ (dotted line), calculated with Equation 7	17
Figure 9: Scheme depicting the zeta potential as the charge Q at the distance from the particle surface d of the slipping plane of the shear layer of a moving particle.	18
Figure 10: Available conjugation sites at the antibody (a) and linkable functional groups on the NP surface (b).	19
Figure 11: Possible strategies to conjugate antibodies to NP.	20
Figure 12: Reaction scheme of coupling of a carboxylic group to an amine mediated by EDC with and without NHS.	21

Figure 13: Normalised fluorescence spectra of PDOF (a) and CN-PPV (b) in THF. Dotted and straight lines are excitation and emission spectra, respectively at a concentration of 0.5 µg/mL.	28
Figure 14: Reaction scheme for carboxylation of Pluronic® F127.	29
Figure 15: ¹ H-NMR spectrum of Pluronic® F127 (a) and F127-COOH (b), recorded at 400 MHz in CDCl ₃	30
Figure 16: Preparation scheme of Si-NP.	31
Figure 17: Zeta potential (a) and hydrodynamic diameter (b) of Si-NP prepared with and without F127-COOH (CP loading dose= 0.1%). Values represent the mean ± standard deviation of n=3 batches. *p< 0.05; **p< 0.01 (Welch-test) TEM images of Si-NP prepared with and without F127-COOH (c).	32
Figure 18: Composition of PDOF-Si-NP suspension with LD=4% after production. Solid content of crude Si-NP compared to that of washed Si-NP plus the dry mass in filtrate fractions (a). Values represent mean ± standard deviation of n=3 Si-NP batches. TGA analysis of the washed NP fraction of a single Si-NP batch following lyophilisation (b).	33
Figure 19: Preparation of Pdots.	34
Figure 20: Number mean hydrodynamic diameter (a) and zeta potential (b) for different NP. Loading doses were 4% (Si-NP) and 83% (Pdots) Values represent mean ± standard deviation of n=3 Si-NP and Pdot batches. One batch of PS-NP and Au-NP was measured in triplicate. **p< 0.01 (Welch-test)	35
Figure 21: Hydrodynamic diameter of Si-NP (a) and Pdots (b) depending on CP loading dose. Values represent the mean ± standard deviation of n=3-5 batches. *p < 0.05 (Welch-test). .	36
Figure 22: Absorption (dashed lines) and fluorescence (solid lines) spectra of THF solution (black) or Si-NP (thin lines) and Pdots (thick lines) loaded with PDOF (a) or CN-PPV (b). CP loading doses were 4% (Si-NP) and 83% (Pdots). Absorption (dashed line) and fluorescence (solid line) spectra of PS-NP (c). Absorption spectrum of Au-NP (d).	37
Figure 23: Combined excitation-emission fluorescence spectrum of PDOF-CN-PPV-Pdots. CP loading dose was 83% in total with a 1:1 ratio of PDOF and CN-PPV. The first order Rayleigh peak was removed by the evaluation software FluorEssence.	37
Figure 24: QY (a and b) and brightness (c and d) of Si-NP (a and c) and Pdots (b and d) depending on CP loading dose of PDOF (blue) or CN-PPV (red). Values represent the mean ± standard deviation of n=3 batches.	39
Figure 25: Dipstick LFI signal performance of CN-PPV-Pdots conjugated at pH=6.5 (a) or pH=7.4 (b). SBR versus IgG amount used for conjugation expressed as percentage of NP surface, that would be covered by the Ab in case of complete reaction. Values are mean and standard deviation of 3 individual test strips.	40

Figure 26: Performance of NP-IgG-conjugates in a FLISA system. Signal-to-background ratio (SBR) of wells coated with capture Ab to wells coated only with BSA. Fluorescent readout of PDOF-Si-NP (blue open circle) and PDOF-Pdots (blue) (both $\lambda_{Ex}/\lambda_{Em}=378/437$ nm) compared to PS-NP (green; $\lambda_{Ex}/\lambda_{Em}=365/406$ nm) and Au-NP (black; $\lambda=534$ nm) (a). CN-PPV-Si-NP (red open circle), CN-PPV-Pdots (red) (both $\lambda_{Ex}/\lambda_{Em}=454/650$ nm) and PDOF-CN-PPV-Pdots (red-blue) ($\lambda_{Ex}/\lambda_{Em}=378/650$ nm) compared to PS-NP (green) Au-NP (black) ($\lambda_{Abs}=534$ nm) (b). Values are mean and standard deviation of means of 3 plates à 3 wells.....41

Figure 27: SBR of PDOF-Si-NP and Au-NP dipstick LFI versus concentration of capture antibody at test line. Data points are mean values and standard deviations of 3 individual strips.54

Figure 28: SBR of PDOF-, CN-PPV- and PDOF-CN-PPV-Pdots in a dipstick LFI with signal detected either by an iPhone XR under illumination in a UV-chamber and successive evaluation with ImageJ software (a) or by the LFReader and successive evaluation with LFStudio software (b).56

Figure 29: Signal-to-background ratio of dipstick LFI run with NP suspensions containing surfactants of different concentration. Values are mean and standard deviations of 3 individual strips.....57

Figure 30: Recovery of IgG-PDOF-Pdots from the conjugate pad without (a) and with (b) pre-treatment of the sample pad with a mixture of 1% Triton X-100, 1% PEG400 and 1% BSA (w/w) in water for different amounts of additive mixture in the conjugate suspension. The additive mixture was composed of Triton X-100, BSA, PEG400, glycerol and sucrose in a 1:1:1:1:1 (w/w) ratio. Values are mean and standard deviations of 3 individual strips.59

Figure 31: Recovery of IgG-PDOF-Si-NP from the conjugate pad for different concentrations of Tween 20 in the conjugate suspension (a). Values are mean and standard deviations of 3 individual strips. Dissected NC membrane after redispersion of PDOF-Si-NP showing uneven release and flow of the NP (b). Direction of NP flow was from bottom to top.....60

Figure 32: Examples of dipstick LFI with PDOF-Pdots (a), CN-PPV-Pdots (b) and PDOF-CN-PPV-Pdots (c) under a UV lamp ($\lambda_{Ex}=365$ nm). Example of Au-NP dipstick LFI under ambient light (d). The direction of flow was bottom to top.60

Figure 33: SBR versus NP mass in dipstick-LFI of rabbit IgG-NP conjugates. PDOF-Si-NP (blue open circle) and PDOF-Pdots (blue) compared to PS-NP (green) and Au-NP (black) (a). CN-PPV-Si-NP (red open circle), CN-PPV-Pdots (red) and PDOF-CN-PPV-Pdots (blue-red) compared to PS-NP (green) and Au-NP (black) (b).....61

Figure 34: Dipstick LFI with CN-PPV-Pdots. SBR of test line (black) and control line (red) versus concentration of tetracycline (a), staphylococcus aureus enterotoxin A (b) and heart fatty acid binding protein (c). Values are mean and standard deviation of 3 individual strips.63

Figure 35: ELISA-like microplate assay of anti-tetracycline, anti-SAE and anti-hFABP IgG-conjugated Au-NP.....	64
Figure 36: Experimental design for the investigation of MCM and HEN catalytic activity.....	75
Figure 37: Hydrodynamic diameter of NP dispersed in 0.1% Tween 20, 0.1% PS-g-PEG-COOH or 0.005% PS-g-PEG-COOH. Data shows mean and standard deviation of two replicates.....	78
Figure 38: Reaction scheme of oxidation of DAB (a) and TMB (b).	79
Figure 39: Absorption of solutions of TMB (a, c, e) or DAB (b, d, f) oxidised by H ₂ O ₂ in the presence of 40 (a, b), 4 (c, d) or 0.4 (e, f) µg/mL NP dispersed in 0.1% Tween 20. Absorption of wells without H ₂ O ₂ and absorption of wells with H ₂ O ₂ , but no catalyst, were both subtracted from the sample absorption values. Data shown is the mean and standard deviation of 3 individual wells distributed over 3 individual plates from a single MCM or HEN batch.....	81
Figure 40: Reaction speed e.g., slope of absorption versus time, for oxidation of TMB (a, c e) and DAB (b, d, f) catalysed by NP dispersed in 0.1% Tween 20 (a, b), 0.1% PS-g-PEG-COOH (c, d) or 0.005% PS-g-PEG-COOH). Background values of wells with MCM or HEN, (without H ₂ O ₂) were subtracted. Each bar of one group shows an individual NP dispersion replicate on an individual plate. Values are mean values and standard deviation of three individual wells per plate. Each middle bar of a group shows one NP dispersion on three replicate plates with three replicate wells each and values are reported as mean and standard deviation of means.	83
Figure 41: Acceleration of TMB (a, c) or DAB (b, d) oxidation by H ₂ O ₂ in the presence of MCM and HEN over reaction with only H ₂ O ₂ . Values of wells without H ₂ O ₂ were subtracted. The NP amount was adjusted to the molar content of Fe(II) or Fe(III) (a, b) or surface area of Fe(II) or Fe(III) (c, d) in the np-Fe ₃ O ₄ NP. Values are mean and standard deviation of 3 individual wells from a single material batch.	85
Figure 42: Acceleration of TMB (a, c) or DAB (b, d) oxidation by H ₂ O ₂ in the presence of MCM and HEN over reaction with only H ₂ O ₂ . 40 µg/mL IgG-conjugated NP were dispersed in 0.1% PS-g-PEG-COOH (a, b) or 0.005% PS-g-PEG-COOH) (c, d). Reaction speed of wells without H ₂ O ₂ was subtracted from the values. Each bar of one group shows an individual NP conjugate replicate on an individual plate. Values are mean and standard deviation of three individual wells per plate.....	87
Figure 43: ELISA of 5 (g, h), 10 (e, f), 25 (c, d) and 50 (a, b) µg IgG-conjugated NP in wells coated with anti-rabbit IgG (solid or segmented lines) or only coated with BSA (dotted lines). Absorption over time with TMB (a, c, e, g) or DAB (b, d, f, h) substrate. Values are mean and standard deviation of three individual wells.....	88

Figure 44: Reaction speed, e.g. slope of absorption versus time, for oxidation of TMB (a, c) and DAB (b, d) catalysed by IgG conjugates of NP dispersed in 0.1% PS-g-PEG-COOH (a, b) or 0.005% PS-g-PEG-COOH (c, d). The wells were coated with anti-rabbit IgG and were incubated with 500 µg/mL rabbit IgG-NP conjugates. Reaction speed of wells coated with BSA only and incubated with 500 µg/mL rabbit IgG-NP conjugates was subtracted from the values. Each bar of one group shows an individual NP conjugate replicate on an individual plate. Values are mean values and standard deviation of three individual wells per plate.90

Figure 45: Batch-to-batch variation of selected HEN. Increase in speed of oxidation of TMB (a, c) or DAB (b, d) by H₂O₂ catalysed by HEN NP over oxidation with H₂O₂ only. HEN were dispersed in 0.1% (a, b) or 0.005% (c, d) PS-g-PEG-COOH. NP concentration was 40 µg/mL for HEN or IgG-HEN-conjugate suspensions or 500 µg/mL for IgG-HEN-conjugate suspensions in ELISA. Data shown are mean values and standard deviations of three replicate wells.91

Figure 46: Increase in speed of oxidation of TMB (a, c) or DAB (b, d) by H₂O₂ catalysed by MCM and HEN NP over oxidation with H₂O₂ only. NP were dispersed in 0.1% (a, b) or 0.005% (c, d) PS-g-PEG-COOH. NP suspensions were used untreated, washed with 50 mM TRIS pH=7.4 containing 0.1% Tween 20, or conjugated to rabbit IgG. NP concentration was 40 µg/mL for NP- or IgG-NP-conjugate suspensions or 500 µg/mL for IgG-NP-conjugate suspensions in ELISA. Data shown are mean values and averaged standard deviations of five replicate plates with three replicate wells each, except for (ZnCuMg)(FeMnCr)₂O₄, which was three replicate wells on one plate.92

Figure 47: Hydrodynamic diameter of MCM and HEN dispersed in 0.05 M TRIS pH=7.4 before and after washing with 0.05 M TRIS pH=7.4 by repeated centrifugation and redispersion. Values of (ZnCu)(FeMnCr)₂O₄ are mean and standard deviation of 3 individual NP dispersions.93

Figure 48: Increase in reaction speed of oxidation of TMB (a, c and e) or DAB (b, d and f) by H₂O₂ catalysed by MCM and HEN NP, dispersed in H₂O (a and b), PBS (c and d) or 50 mM TRIS pH=7.4 (e and f), over oxidation with H₂O₂ only. NP suspensions were used untreated, or washed with the respective dispersant three times by centrifugation sedimentation and redispersion. The supernatants were combined, freeze-dried and diluted with water to match the concentration in the untreated suspensions. NP concentration was 40 µg/mL. Values are mean and standard deviations of three wells.95

List of Tables

Table 1: Examples for autofluorescence in biological matrices.....	13
Table 2: Advantages and disadvantages of CP-NP compared to other fluorescent labels in LFI.	14
Table 3: Comparison of published optical properties of fluorescent dyes used in LFI.....	28
Table 4: Key characteristics of Si-NP and Pdot preparation methods. *Mean and standard deviation of 4 batches.....	34
Table 5: Comparison of optical properties of fluorescent NP. CP loading doses were 4% (Si-NP) and 83% (Pdots). *Values represent the mean \pm standard deviation of n=3 Si-NP and Pdot batches. CP concentration for QY measurement was 1 $\mu\text{g}/\text{mL}$ (PDOF-NP) and 4 $\mu\text{g}/\text{mL}$ (CN-PPV-NP).....	38
Table 6: Fluorescence signal intensities of blank NC membranes at excitation and detection wavelengths of the QIAGEN LFReader. Values are averages over 1 cm of the membrane..	53
Table 7: Summary of properties of anti-tetracycline, anti-SAE and anti-hFABP IgG-CN-PPV-Pdots in comparison to rabbit IgG-PDOF-Pdots.....	62
Table 8: eLFI systems published with comparison to colorimetric LFI.	70
Table 9: Concentrations of nanozymes in assessment of catalytic activity to match the molar content of Fe(II) or Fe(III) or the molar content of Fe(II) or Fe(III) on the NP surface in the sample to $\text{np-Fe}_3\text{O}_4$	76
Table 10: Number mean hydrodynamic diameter and zeta potential of the same MCM, HEN and $\text{bm-Fe}_3\text{O}_4$ NP dispersions before and after conjugation to rabbit IgG.	86

Abbreviations

Ab	Antibody
bm	ball-milled
BSA	Bovine serum albumin
CCD	Charge-coupled device
CFU	Colony forming units
CN-PPV	Poly-(2,5-di-hexyloxy-cyanoterephthalylidene)
COPD	Chronic obstructive pulmonary disease
CP	Conjugated polymer
Cry1Ab	Pesticidal crystal protein Cry1Ab
DAB	[1,1'-Biphenyl]-3,3',4,4'-tetramine
DLS	Dynamic light scattering
DMSO	Dimethyl sulfoxide
DNA	Deoxyribonucleic acid
<i>E. coli</i>	<i>Escherichia Coli</i>
EDC	1-Ethyl-3-(3-dimethylaminopropyl)carbodiimide
eLFI	Dye-reaction-enhanced lateral flow immunoassay
ELISA	Enzyme-linked immunosorbent assay
F127-COOH	Pluronic© F127 with terminal carboxylic acid groups
FLISA	Fluorescence-linked immunosorbent assay
FRET	Förster resonance energy transfer
hCG	Human chorionic gonadotropin
HEA	High-entropy alloys
HEM	High-entropy materials
HEN	High-entropy nanoparticles
HEPES	2-[4-(2-Hydroxyethyl)piperazin-1-yl]ethanesulfonic acid

hFABP	Heart fatty acid binding protein
HOMO	Highest occupied molecule orbital
HRP	Horseradish peroxidase
IC	Internal conversion
IgG	Immunoglobulin G
ISC	Inter-system crossing
LD	Loading dose
LED	Light-emitting diode
LFI	Lateral flow immunoassay
LOD	Limit of detection
LOQ	Limit of quantification
LUMO	Lowest unoccupied molecule orbital
m	Multiplet
MCM	Multi-cationic material
mPEG-HS	Methoxy-polyethylenglycol-thiol
MWCO	Molecular weight cut-off
NC	Nitrocellulose
NHS	<i>N</i> -hydroxysuccinimide
NMR	Nuclear magnetic resonance spectroscopy
np	non-processed
NP	Nanoparticle
OD	Optical density
P	Phosphorescence
PBS	Phosphate-buffered saline
PBST	Phosphate-buffered saline containing 0.05% (w/v) Tween 20
PCR	Polymerase chain reaction

PDOF	Poly-(9,9-di- <i>n</i> -octyl-fluorenyl-2,7-diyl)
Pdot	Polymer dot
PEG	Poly(oxyethylene), Polyethylene glycol
PEG400	Poly(oxyethylene), number average molar mass is 400 g/mol
PPG	Poly[oxy(1-methylethylene)], Polypropylene glycol
PS	Poly(1-phenylethene), Polystyrene
QD	Quantum dot
QY	Quantum yield
RE	Rare-earth
RNA	Ribonucleic acid
ROS	Reactive oxygen species
RT	Room temperature
S	Singlet state
s	singlet
SAE	<i>Staphylococcus aureus</i> enterotoxin A
SEC	Size exclusion chromatography
Si-NP	Silica-shell cross-linked nanoparticle
SBR	Signal-to-background ratio
SMD	Small-molecule dye
T	Triplet state
TEM	Transmission electron microscopy
TGA	Thermogravimetric analysis
THF	Tetrahydrofuran
TMB	3,3',5,5'-Tetramethyl[1,1'-biphenyl]-4,4'-diamine
TRIS	2-Amino-2-(hydroxymethyl)propane-1,3-diol
UC-NP	Up-converting nanoparticle

UV	Ultraviolet
VR	Vibrational relaxation
phen	Phenanthroline
ZP	Zeta potential

Chapter 1

Introduction

1.1 LFI

Although human knowledge and technology is advancing, mankind is constantly threatened by chaotic changes in the genome, e.g. cancer, bacterial or viral mutation. The latter is a threat recently encountered as the pandemic of COVID-19 with 79.2 million cases and 1.7 million deaths worldwide in one year as of end of December 2020.¹ While the first occurrence of *Yersinia pestis*, the pathogen causing the epidemic plague, is evident 4800-3700 b.c., strategies to face epidemics and pandemics are still under development.² The way of handling epidemic diseases changed from exclusion of sick people in medieval times over control and confinement in early modern times to recent strategies of statistic prediction, vaccination and isolation.³ A basic requirement for successful containment of epidemic diseases is the fast identification of infected persons for quick isolation and treatment.⁴ It was shown for the current pandemic, that a negative correlation between the number of tests per inhabitant and mortality exists, meaning, that a higher number of tests could decrease the number of deaths.⁵ Thus, there is a demand for cheap and rapid testing methods. The most sensitive assay to test for viral pathogens to-date is real-time PCR with the ability to detect as few as 10 copies of RNA.⁶ However, it takes more than an hour to run the assay, as well as special equipment and experienced lab personnel, requirements that are unpractical for field studies and less developed environments. The most easy-to-use method, on the other hand, is the lateral flow immunoassay (LFI), which can give a result in less than 20 min even without sophisticated equipment or lab staff. A general scheme of an LFI is depicted in **Figure 1**.⁷

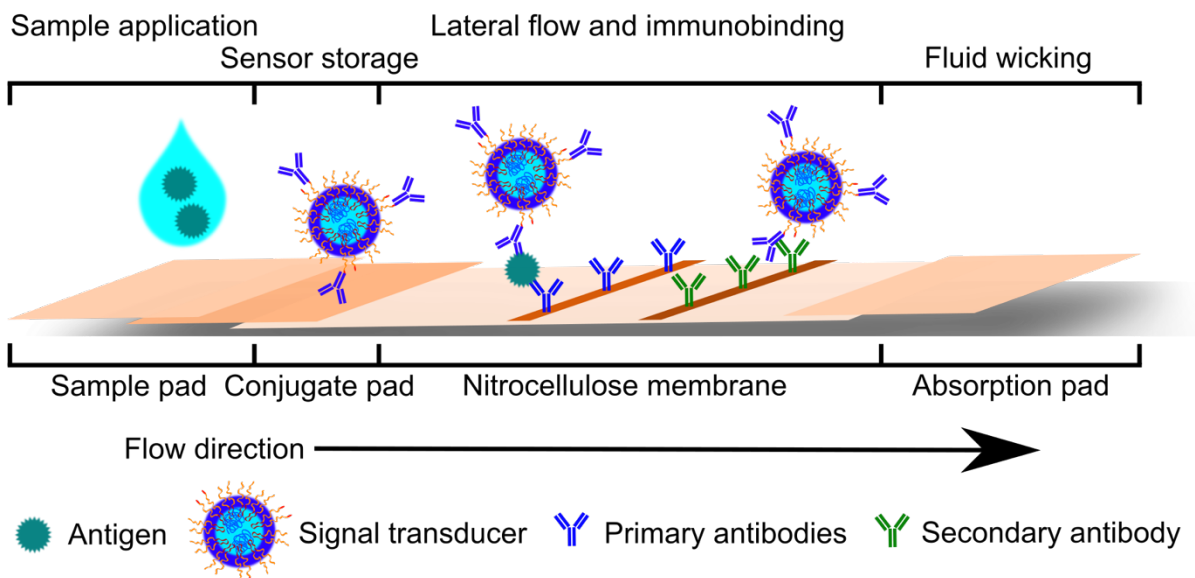


Figure 1: Schematic layout and working principle of an LFI. A sample containing an antigen is applied to a porous pad and wicked through a storage of signal transducers, forming an immunocomplex. The complex moves through an NC membrane by capillary force and is bound by antibodies adsorbed at the test line. Remaining signal transducer is bound by a secondary antibody fixed on the control line and excess liquid is wicked by an absorption pad.

The working principle is simple: A sample fluid containing an antigen is dropped on a fibrous pad and capillary forces wick the liquid through a depot of signal transducers that have the ability to both bind to an antigen-site and be detectable. The complex of antigen and signal transducer moves through a nitrocellulose (NC) membrane. Antibodies (Ab), that are adsorbed on the test region of the membrane (primary Ab), bind the sample antigen and fix the antigen-signal-transducer-complex to a distinct location. The liquid is further sucked into the absorbent pad, but the signal transducers are retained in the test region. Usually, an excess of signal transducers flow past the test line and subsequently bind to an Ab, specific to the Ab on the NP probe (secondary Ab) in the so-called control region. Binding of the signal transducers in the control region is important to verify the successful capillary flow.

In an alternate LFI design, the signal transducer is stored separately from the test strip as a dispersion. No conjugate or sample pad are necessary in this case. For application, the strip is dipped in a mixture of the dispersion and the sample. This format is called dipstick LFI.⁸

The principle was first published as a US patent in 1989.⁹ However, many innovations were necessary beforehand, for example the quantification of Ab-analyte binding with radio-labelled insulin, the fixation of Ab on a solid NC support or the use of colloidal labels for visual interpretation of the assay.¹⁰⁻¹³ Since discovery, LFI have been developed for a huge variety of analytes.¹⁴ The analytic principle can be divided in two groups, depending on the nature of the analyte: Sandwich immunoassays are used for big analytes, like proteins, viruses or bacteria, that feature at least two Ab binding sites (**Figure 2a**). In this format, a sandwich complex of Ab, antigen and labelled Ab is formed in the test region and a high signal intensity indicates the presence of a high concentration of analyte. Competitive immunoassays are used for small analytes that have only one Ab binding site (**Figure 2b**). The formation of a sandwich complex is not possible in this case. Instead of an Ab, that is specific to the analyte, the analyte itself is fixed to the test region of the NC membrane. The signal transducer, decorated with an Ab, might bind to the fixed antigen. If the analyte is present in the sample, the binding sites of the signal transducer are blocked and the signal at the test region is reduced.

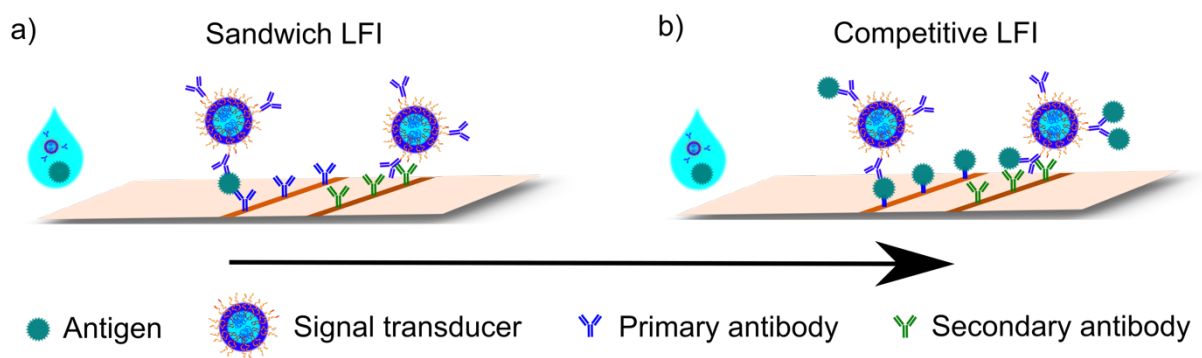


Figure 2: Analytic principle of the sandwich (a) and the competitive (b) LFI.

The European Commission recommended the use of LFI to face the COVID-19 pandemic.¹⁵ However, in a field study on patients in a hospital in Brussels, only 32 out of 106 infected patients had a positive test result using a colloidal gold-based (Au-NP) antigen-LFI.¹⁶ This is alarming, as patients who are falsely classified healthy potentially spread the virus. Thus, there is an urgent need for more sensitive LFI. To increase sensitivity, a wide range of different signal transducers and detector systems was developed to allow higher intensity or reduce the background signal, thus increase the signal-to-background ratio (SBR). In addition to sensitivity-enhancement, recent research focuses on increase of specificity, cost reduction, compatibility with biological sample matrices, quantification and simultaneous detection of several analytes.¹⁷

1.2 Fluorescent LFI

Fluorescence is the emission of a photon $h \cdot \nu_2$ from the vibrational ground state of an excited electronic state S_1 of a molecule under relaxation to a higher vibrational state of the electronic ground state S_0 .¹⁸ (**Figure 3a**) The excited state was generated beforehand by absorption of a photon of higher energy $h \cdot \nu_1$ to a high vibrational state of S_1 and relaxation by vibrational relaxation (VR) to the vibrational ground state of S_1 .

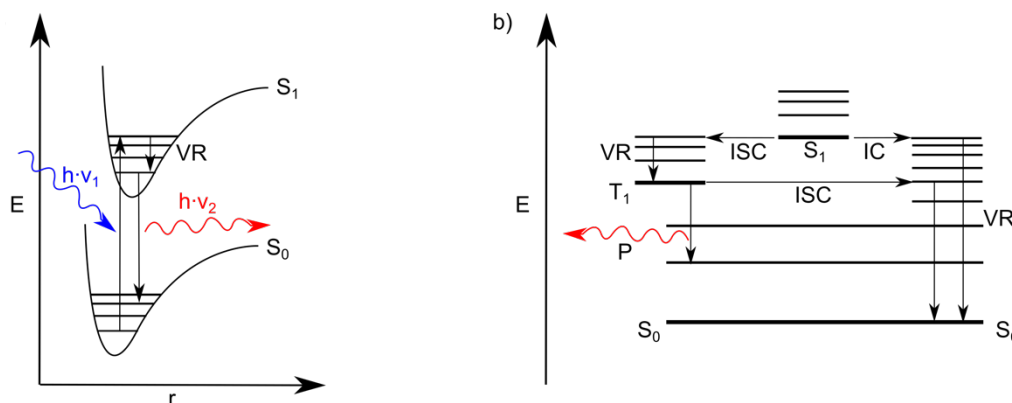


Figure 3: Energy-core-distance-diagram of an electron, illustrating the process of fluorescence (a) and non-fluorescence relaxation mechanisms of the excited electronic state (b) including internal conversion (IC) from an excited singlet state (S_1) to the singlet ground state (S_0) or inter-system crossing (ISC) between singlet and triplet (T_1) states with following vibrational relaxation (VR) or phosphorescence (P). Bi-molecular relaxation processes are excluded for easy reading. Figures are based on W.-D. Stohrer, *Die konzeptionellen und theoretischen Grundlagen der Photochemie*, in: *Photochemie*, Wiley-VCH Verlag GmbH & Co. KGaA, Weinheim, FRG, 2005: pp. 43–64. DOI: 10.1002/3527603247.ch2.

When fluorescent labels are used as signal transducers in LFI, the difference in energy between the excitation and emission light, the Stokes-shift, filters the excitation wavelength from the emitted light before detection, thus reducing the background signal in comparison to measurement without filtering or to absorption measurement. This is especially useful, as it was shown, that, in case of high background scattering, the SBR in fluorescence spectrometry does not strictly increase with light intensity and illumination duration, but has a maximum. But if the background signal is low, the SBR does increase with intensity and illumination time, thus eliminating the need to optimise for these parameters and simplifying the measurement.¹⁹ As a result, the LFI sensitivity might be improved.

The basic requirement for fluorescence is the absorption of a photon to generate the excited state. As the life-time of the excited state is very short, fluorescence is a fast process and the intensity is proportional to the probability of absorption.¹⁸ The proportion of absorbed light intensity I_{Abs} to initial light intensity I_0 , e.g. probability of absorption, in dilute solutions is given by the Lambert-Beer-Law. **(Equation 1)**

$$\frac{I_{Abs}}{I_0} = 1 - 10^{-\varepsilon * c * d} \quad (1)$$

It shows, that the amount of absorbed light has a positive correlation with not only the concentration of dye c and the pathlength d , but also with the extinction coefficient ε , a wavelength-dependent intrinsic property of the dye molecule. Thus, a high extinction coefficient is necessary for intense fluorescence.

However, fluorescence is not the only possible way for the relaxation of the excited electronic state of a molecule. In fact, a number of radiative and non-radiative decays exist.²⁰ **(Figure 3b)** The number of excited states that relax by fluorescence per total number of excited states is called the quantum yield (QY). It is an intrinsic property of the dye molecule, as well as influenced by the chemical environment. Given the limited sensitivity of a photon detector, both QY and ε are desired to be high for detection of small amounts of dye, e.g. high LFI sensitivity. In a complex environment, like a dye nanoparticle formulation, the intensity of the fluorescence is further reduced through absorption, diffraction, refraction or scattering of the emitted light. Thus, the type of fluorescent dye, as well as formulation, highly influence the LFI sensitivity.

Fluorescent LFI were first published in a US patent in 1998.²¹ To date, several manufacturers commercially distribute fluorescent LFI for various analytes.^{22–25} In studies comparing antigen LFI with PCR for the current COVID-19 disease, only 32 COVID-19 positive results were detected with a Au-NP LFI test out of 102 PCR-positive patients (i.e., 31%), but 77 positive results out of 82 PCR-positive patients were observed using a time-resolved fluorescent LFI (94%).^{16,26} However, in the quartile of PCR-positive patients with lowest viral load, the fluorescent LFI detected only 13 out of 18 cases (72%). This indicates, that the sensitivity of fluorescent LFI has to be further improved.

1.3 CP in LFI

Conjugated polymers (CP) are polymers that feature conjugated double bonds along the polymer backbone. Therefore, the pi-electrons of these bonds are delocalised over the length of the polymer. (**Figure 4a**)

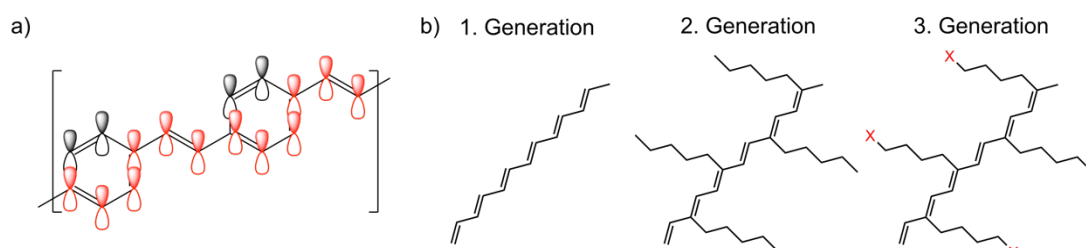


Figure 4: Conjugation of pi-bonds along the backbone of a CP (a) and the three generations of CP (b).

As a result, CP may show a variety of interesting properties, such as electrical conductivity, high absorption of light and intense fluorescence. Historically, the preparation of CPs dates back to the 1950s, where pyrolysis or chemical reduction of poly(vinylchloride), poly(vinylbromide) or poly(vinylalcohol) yielded products, that were not very well defined and exhibited poor electrical conductivity. Giulio Natta prepared highly crystalline poly(vinylene) already in 1958, but the product was impractical due to its physical properties and processability.²⁷ However, the first usable CP to be synthesized by polymerization with a well-defined structure were polypyrrole and polyaniline in the 1960s.²⁸ Alan Heeger and Alan MacDiarmid were awarded the nobel prize for these findings in 2010, together with Hideki Shairakawa, who was the first to investigate the preparation of poly(vinylene) thin films.²⁹ The first conjugated polymers were homopolymers and had a large band gap between the highest occupied molecule orbital (HOMO) and lowest unoccupied molecule orbital (LUMO), resulting in a low conductivity and short wavelength fluorescence. A major finding of the 2010 Nobel laureates was the dramatic increase in conductivity of the CP by doping with halogens.

To achieve intrinsic conductivity and at the same time extend the range of fluorescence to near-infrared, alternating co-polymers of monomers with electron-rich and electron-poor regimes in the backbone were created.³⁰ In these polymers, the band gap is reduced by a push-pull-principle.

The conjugated bonds lead to high stiffness of the polymer backbone, as well as intra- and intermolecular pi-pi-stacking, both of which reduce solubility and therefore processability of the material. That is why a second generation of conjugated polymers was produced, that were decorated with bulky alkyl side chains to increase the solubility. The third generation of conjugated polymers features functional groups on the side chains for improved physical or chemical properties.³¹ **(Figure 4b)** The tunability of HOMO and LUMO, high electrical conductivity, good processability and functionalisability of modern CP opens a wide scope of applications. In a vast growing number of publications, CP are used for self-healing printable electronics, optoelectronics, like light-emitting diodes (LED) or solar cells, energy storage, micromechanics, corrosion control, photocatalysts, biosensors and imaging probes, just to name a few.^{32–39} The main advantages of CP over other dyes in LFI are basically the same as in bioimaging. High extinction coefficients and QY lead to a high sensor brightness, low fluorescence bleaching increases duration of readability of the signal and tunability of HOMO and LUMO allow for choice of excitation and emission wavelengths to tolerate various biological matrices.⁴⁰

The first application of CP as fluorescent dye in LFI was published in 2018 for the simultaneous detection of three different tumor markers.⁴¹ Three CP with different luminescence colours, PF-TC6FQ (red), PFCN (green) and PFO (blue), were used, one for one tumor marker each. Thus, the analyte present in the sample was not only coded by the location of the test line on the strip, but also by a distinct colour. The CP were formulated as NP with a packed CP core, stabilised by amphiphilic polystyrene with carboxylic-acid-conjugated polyethylene groups grafted to the backbone (PS-g-PEG-COOH). The carboxy-moieties were used to conjugate the Ab to the NP. Because of the small size and excellent optical properties of the CP NP, the group named the particles polymer dots (Pdots), based on the quantum dots (QD). The limit of detection (LOD) for prostate specific antigen (PSA) was reported to be 2.05 pg/mL, while the latest published LOD of a Au-NP LFI from 2016 was 300 pg/mL PSA.⁴²

The same group later published a system, in which secondary Ab-conjugated Pdots were fixed on the test line. The immunocomplex of antigen and primary Ab-conjugated Pdots moved through the membrane and was bound to the test region.

The excitation wavelength used for detection was specific to the Pdots on the test line. Due to close proximity of the two Pdots and overlapping emission and excitation spectra, the primary Ab-conjugated Pdots were excited by Förster resonance energy transfer (FRET) in case of a positive readout. However, the LOD for PSA of the system was 320 pg/mL, which was disappointingly higher compared to the earlier publication.⁴³

As the sensitivity of the assay is dependent on the formation of the Ab-antigen-complex, the comparison of the reported LOD with conventional LFI in literature might not be valid. To prove the advantage of CP in LFI, the same combination of analyte and antibody for CP-based fluorescent LFI and Au-NP LFI still has to be investigated.

1.4 Dye-reaction-enhanced LFI

The advantage of colorimetric LFI over fluorescent LFI is the easy visual readout, which does not require optical instrumentation, such as special light sources or optical filters. However, fluorescent LFI are much more sensitive. The signal intensity of colorimetric LFI is limited by the extinction coefficient of the label and to improve the sensitivity, the absorption of the signal transducers has to be amplified. In a dye-reaction-enhanced LFI (eLFI), the signal transducer has catalytic activity towards the colour-changing reaction of a dye substrate.⁴⁴ After lateral flow of the labeled sample and capture at the test line, a dye substrate is applied to the NC membrane and a colour change is observed. (**Figure 5**) Adopted from the well-established enzyme-linked immunoassay (ELISA) method, the dye reaction often is an oxidation by H₂O₂.

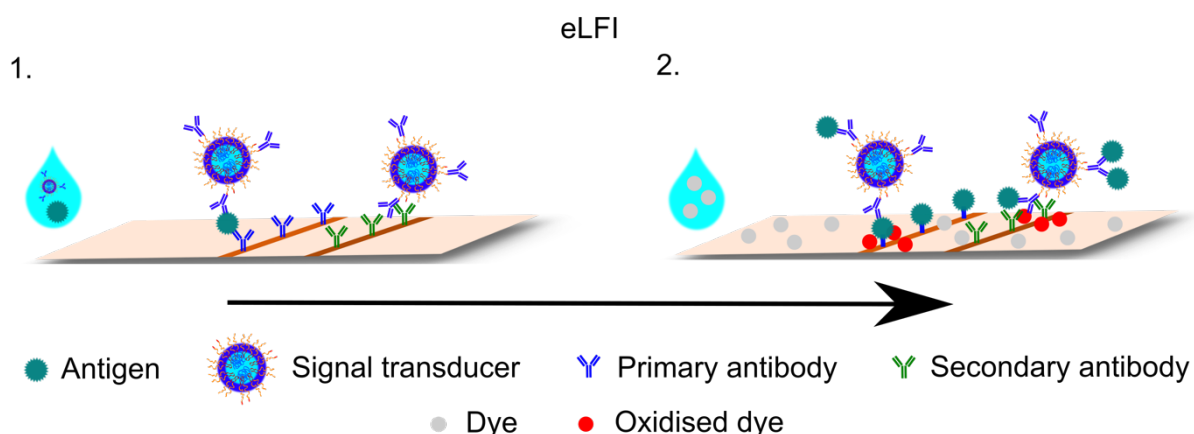


Figure 5: Principle of the eLFI. After lateral flow and immunosorption (1), a dye substrate is applied and the change of dye colour is catalysed by the signal transducer (2).

Given the nature of a catalyst to accelerate a reaction, the colour change is most intense in the area of bound labels at the test line and correlates with the amount of the signal transducer.

The first eLFI was published in 2005 for detection of hepatitis B surface antigen with an HRP-conjugated antibody as signal transducer.⁴⁵ After immunosorption, oxidation of 3,3',5,5'-tetramethyl[1,1'-biphenyl]-4,4'-diamine (TMB) led to a 30-fold increase of sensitivity, compared to the Au-NP LFI. However, the method used only one molecule of HRP per antibody and the signal amplification could be possibly improved by conjugation of several catalyst moieties on one antibody. In 2009, the use of HRP-decorated Au-NP reporters in eLFI was published for detection of DNA.⁴⁶ The test line signal was still visible for 0.2 nM DNA sample, a 25-fold lower signal intensity compared to Au-NP LFI (5 nM), but after optimisation of the HRP-NP-conjugation process, the test line became visible even for 0.01 pM DNA samples.⁴⁷ Thus, the detectable concentration by visual readout could be improved 500,000-fold by eLFI, compared to Au-NP LFI. As the signal of eLFI can be observed at high analyte concentrations without successive dye reaction or with successive dye reaction at low analyte concentrations, the dynamic range of eLFI can be very broad.⁴⁸ The major disadvantages of enzymes as catalysts, like HRP, are the ease of denaturation and therefore elimination of catalytic activity, as well as high production costs. Therefore, recent research focuses on finding cheap and stable nanocatalysts.

1.5 Nanocatalysts as signal transducers in LFI

To overcome some of the disadvantages of natural enzymes, catalytically active artificial inorganic nanomaterials were designed. Based on their natural predecessors and nano-scale size, they were called "nanozymes".⁴⁹ They have been sub-divided according to the type of catalysed reaction of the eponymous enzyme into peroxidase-like, oxidase-like or antioxidant nanozymes. While the latter is used for therapeutic approaches, the first two are used as signal transducers in eLFI.⁵⁰ Compared to enzymes, nanozymes are easily produced at low cost in high quantities, have superior stability and may even catalyse reactions uncommon in natural processes.⁵¹ The superior stability of nanozymes is not only beneficial for storage of the assay, but can be utilised to mask natural enzymes in biological matrices by denaturation, leaving the nanozyme intact.⁵² The signal intensity in eLFI is strongly influenced by the catalytic activity of the signal transducer and increases with the particle surface. Similar to HRP-decorated Au-NP, carrier-NP might be decorated with nanozymes to increase the active surface area per signal transducer.⁵³ However, nanozymes have the advantage, that the surface can be increased by variation of the NP geometry. For example, porous particles, concave platelets and nanosheets were used in LFI.⁵⁴⁻⁵⁶ Of course, the catalytic activity is also an intrinsic property of the NP material. Therefore, the discovery of new materials with superior activity is desired.

1.6 Study questions and aims of the thesis

An increase in sensitivity of point-of-care-assays is needed. Both fluorescent LFI and dye reaction-enhanced LFI have proven to be suitable strategies to lower detection limits. Still, the sensitivity of the assays has to be increased to give accurate results with low concentrations of analyte. A key factor to increased sensitivity is the signal transducer and an improvement of it is desirable.

For fluorescent LFI, the signal transducer can be improved by use of fluorescent dyes with improved optical performance. Conjugated polymers can have very good optical properties, thus being excellent candidates as fluorescent dyes in LFI. Due to their high molecular weight and hydrophobicity, they have to be formulated in nanoparticles to work as signal transducers. Therefore, it has to be determined, which NP container is most suitable for CP. (Chapter 2) While studies showed improved LFI sensitivity of various fluorescent LFI in comparison to colorimetric LFI, no direct comparison between gold-based colorimetric LFI and CP-based fluorescent LFI exists for the same matched pair of antibody and antigen. This comparison has to be made to verify improved performance and was addressed in Chapter 3.

For dye-reaction-enhanced LFI, the sensitivity of the assay is dependent upon the catalytic activity of the signal transducer. Nanozymes are catalysts, that have some advantageous properties over enzymes, such as increased storage stability and improved tolerance for high reactant concentrations. High-entropy materials can be produced as nanoparticles (HEN) and have shown improved catalytic activity over conventional catalysts. Their complex composition allows for a multitude of variations to fine-tune the catalytic performance. Chapter 4 describes the first investigations of HEN as nanocatalysts for use in ELISA assays. The aim of the investigation was to determine which HEN compositions have a higher catalytic activity, compared to published nanozymes, to assess the possible use in LFI.

Chapter 2

CP-based fluorescent nanoparticles:
CP-NP optimisation, physicochemical characterisation
and antibody conjugation

2.1 Introduction

2.1.1 Fluorescent signal transducer specifications for high sensitivity of LFI

Even though LFI are in general considered user friendly, the signal transducers used have to meet quite a number of criteria. This is due to the many interactions of the sensor with not only the analyte, but also medium, LFI membrane, capture antibodies and signal detection method. The desirable qualities are:

- High brightness
- Large Stokes shift
- Long shelf-life
- Low toxicity
- Dispersibility in sample matrix or running buffer
- Inertness to sample matrix
- Fast, selective and strong binding to analyte
- Weak interaction with LFI membrane
- Unhindered flow through membrane pores
- Fast and strong binding to capture antibody
- Low signal decay

For dye-loaded fluorescent NP signal transducers these qualities can be tuned by variation of a number of NP properties:

- Dye loading dose
- Encapsulating material
- Size and shape
- Surface chemistry
- Type of detection molecule
- Type of NP binding to the detection molecule

The signal-to-background ratio (SBR) is one of the main factors that influences LFI sensitivity. Thus, a high NP brightness and low background signal intensity are desirable. NP brightness correlates both with extinction coefficient, as well as QY. The background signal intensity increases, if the detector measures at a wavelength close to the excitation light.⁵⁷ Therefore, a large Stokes-shift of the fluorophore leads to decreased background intensity, thus higher signal-to-background ratio. A large stokes shift furthermore reduces the autofluorescence intensity of a biological sample fluid. An overview over excitation and emission wavelengths of biological components is given in **Table 1**.^{58,59}

Table 1: Examples for autofluorescence in biological matrices.

Fluorophore	λ_{Ex} [nm]	λ_{Em} [nm]
Aromatic amino acids	240-280	280-350
Xanthine	≈ 320	420-430
Fatty acids	330-350	470-480

As part of the study, it was of interest to understand how NP brightness and Stokes-shift influence the SBR in immunoassays. Thus, three different fluorophore systems are investigated. PDOF has a very high extinction coefficient and QY, while CN-PPV has a very large Stokes-shift. The blend of both (PDOF-CN-PPV) has an extinction coefficient and QY in between the two and, through absorption at the short wavelength of PDOF and Förster resonance energy transfer (FRET) to CN-PPV with subsequent fluorescence emission, increased Stokes-shift. (**Figure 6**) As both fluorophores are polymers and have the excited states mobile over large parts of the conjugated backbone, FRET between polymer chains is promoted. The high efficiency of FRET in CP is well-known and has been readily exploited in bio-sensing.⁶⁰

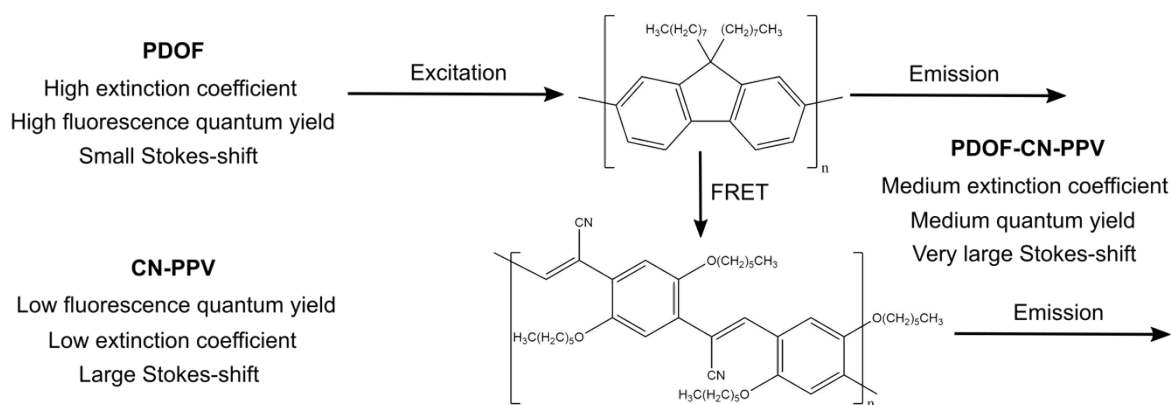


Figure 6: Energy transfer from excited PDOF to CN-PPV and subsequent fluorescence emission in a CP blend.

2.1.2 CP-NP vs other fluorescent signal transducers in LFI

Using NP as signal transducer was first reported in 1980 and has become a vivid field of research.^{13,14,61,62} In comparison to single molecules, NP may contain a huge number of reporters, increasing the signal intensity.⁶³ Common NP systems include coloured NP, magnetic NP, luminescent NP and others. (**Figure 7**) Coloured NP are the oldest kind of NP signal transducers in LFI and the most easy to analyse, as the readout is visual.^{13,64}

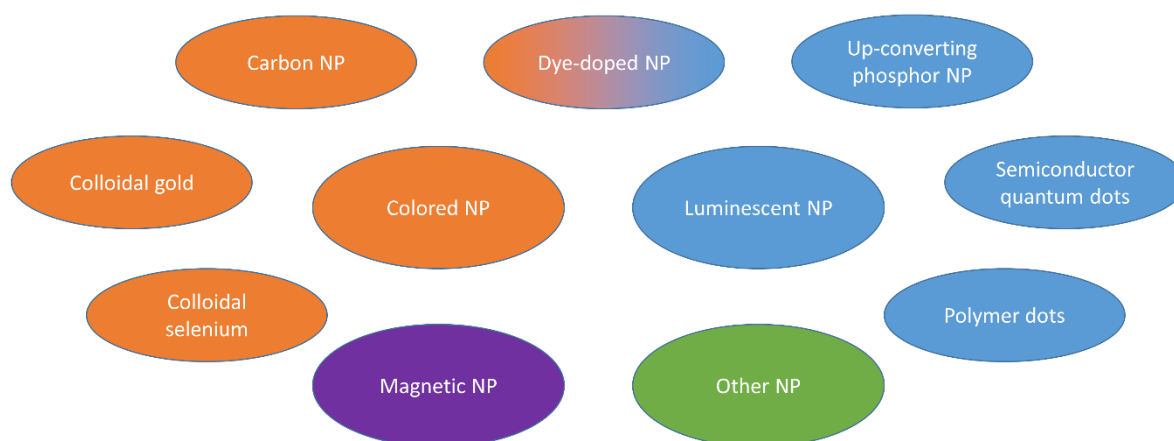


Figure 7: Overview of existing NP signal transducers in LFI.⁶²

A problem with visual interpretation of the signal is quantification as well as the small cross-section of the membrane that is accessible for readout. While the membrane has a thickness of at least 100 μm , only 10 μm are used for optical interpretation due to refraction of light by the membrane material.⁶⁵ Magnetic NP do not suffer signal reduction by refraction and can therefore be detected in the whole membrane volume of interest. Luminescent NP allow detection at a different regime of either time or wavelength compared to excitation to reduce the background signal intensity. Although very bright, small molecule dye (SMD) luminescent NP often suffer from photobleaching, limiting the quantification of the readout. Less bleaching is observed for up-converting NP (UC-NP), which also increase signal-to-background ratio through use of the rare anti-Stokes-shift, as well as for fluorescent semiconductor NP, so called quantum dots (QD). The disposal of QD-LFI is problematic for both kind of signal transducers, as the NP are mostly made of toxic materials.⁶⁶ As a new approach, CPs may serve as fluorescent dye for NP. In contrast to QD materials, CP are usually not toxic but offer high extinction coefficients and QY. An overview over advantages and disadvantages of CP-NP compared to other fluorescent signal transducers in LFI is given in **Table 2**.

Table 2: Advantages and disadvantages of CP-NP compared to other fluorescent labels in LFI.

	Intensity	Background signal	Bleaching	Toxicity	Biodegradability
SMD	Low	Low-High	High	Low	Low-High
SMD-NP	High	Low-High	High	Low	Low-High
UC-NP	Low	Low	Low	High	Low
QD	High	Low	Low	High	Low
CP-NP	High	Low	Low	Low	Low

Some NP encapsulation strategies that can be used with small molecule dyes are not possible with CP. For example, polystyrene nanoparticles (PS-NP) are commonly loaded with fluorescent dyes by a swelling-deswelling approach.⁶⁷ The high molecular weight of CP does not allow diffusion of the CP into the swollen PS particles. However, three main strategies for encapsulation of CP have been established, namely the nano-precipitation-, mini-emulsion- and self-assembly-method.⁶⁸ Independent of the method used, the CP is usually encapsulated within a surfactant, that stabilises the suspension and allows surface modification. For *in-vivo* bioimaging applications, the surfactants are preferably degradable, to improve clearance of the NP.^{69,70} In contrast, a very stable NP is necessary for LFI to increase shelf-life. As such, silica-shell cross-linked NP (Si-NP) were published to encapsulate CP with preservation of optical properties and modifiable surface.⁷¹ In these particles, the CP was located within the hydrophobic core of the micelle of an amphiphilic tri-block copolymer, Pluronic® F127. The micelle was confined by a layer of porous silica, that was formed at the interface between the copolymer blocks, greatly enhancing the NP stability. In a different approach, CP were co-precipitated with an amphiphilic polystyrene-*b*-polyethyleneglycole block copolymer.⁴¹ The resulting NP, so-called polymer dots (Pdots), had a solid CP core surrounded by the amphiphilic molecules, likely stabilised by the similar polarity of the CP and polystyrene subunits. Both Si-NP and Pdots showed promising properties in literature and are therefore worthwhile investigating in LFI.

2.1.3 Dye loading and optical performance

An easy option to increase brightness is incorporation of multiple dye molecules in a single particle. For example, fluorescent Ru(phen)₃²⁺ doped silica particles were found to enhance the luminescence intensity 23,000-fold compared to a single dye molecule.⁶³ But the improvement of particle brightness by increase of dye concentration is limited and fluorescence intensity is known to drop over a certain concentration.⁷² The main mechanisms for fluorescence quenching with increasing fluorophore concentration are aggregation-induced quenching and absorption of the exciting light (primary inner filter effect), as well as reabsorption of the emitted light (secondary inner filter effect) by the dye molecules.¹⁸ The brightness of NP in relation to CP concentration inside the NP, e.g. loading dose (LD), is therefore affected by an increase through higher absorption of exciting light, as well as a decrease by the inner filter effect.

The amount of excitation light absorbed is given by Beer-Lambert law. (**Equation 1**) The Lambert-Beer law is an empiric finding and holds true for dilute solutions in which scattering of the light does not occur. However, in case of small NP with $d \ll \lambda/\pi$ the main scattering mechanism is by Rayleigh scattering and the fraction of such is negligible in comparison to absorbed light.⁷³ Thus, the Lambert-Beer law can be well accepted for comparison of particles of similar geometry.

After absorption of light by the dye molecules, the amount of emitted fluorescent light is reduced by non-radiative relaxation, expressed as the quantum yield Φ (**Equation 2**). In fluorescence spectroscopy, the fluorescence intensity is further reduced by the primary and secondary inner filter effect as described in **Equation 3**.¹⁸ The exponent contributes to the decrease in intensity by absorption at excitation and emission wavelength that has to pass through each half the path length of the cuvette. However, in an LFI, the emitted light is detected from the whole intersection of the NC membrane and the primary inner filter effect does not apply. Still, the secondary inner filter effect may reduce the intensity of emitted light. Thus, the brightness of the NP depending on concentration of dye is given by **Equation 4**.

The resulting function has a local maximum which describes the optimal dye loading concentration with maximal brightness. (**Figure 8**, solid line) However, if the extinction coefficient at emission wavelength is negligible, as expected for dyes with large Stokes-shift, the function has no maximum, but is steadily increasing. (**Figure 8**, segmented line) Furthermore, as the path length of light through NP typically does not exceed some hundred nm, the optical density in a particle is small. For example, in case of a NP that is composed of 100% PDOF with an extinction coefficient of $\epsilon_{\text{Ex}}=97.9$ L/g/cm, an approximated density of $\delta=1.05$ g/cm³ and a hypothetical path length of $d=100$ nm, the optical density is only $\text{OD}_{\text{Ex}}=0.01$. Even if the optical density at emission wavelength would be as high as it is at excitation wavelength, 25 NP would have to be stacked to reach the brightness maximum. For small optical densities the brightness appears to be more or less linearly depending on dye concentration. To find a linear equation, that approximates the relation between brightness and dye concentration for small optical densities, **Equation 4** has to be derived for the concentration at $c=0$. The general derivation of **Equation 4** for concentration gives **Equation 5**. Inserting $c=0$ gives **Equation 6** and integration leads to the line function given by **Equation 7**. (**Figure 8**, dotted line) Likewise, it is published, that the brightness of a fluorophore is proportional to $\epsilon_{\text{Ex}} \cdot \Phi$.⁷⁴ As shown in the above considerations, this holds true for small optical densities, e.g. small particles or single dye molecules, but the bigger the particle, the bigger the deviation of the brightness from the linear relation. As shown for the example of PDOF NP, the NP investigated in this thesis are small enough, that brightness is expected to increase with dye loading dose.

$$\frac{I_{Abs}}{I_0} = 1 - 10^{-\varepsilon_{Ex} * c * d} = 1 - 10^{-OD_{Ex}} \quad (1)$$

$$I_{Fl} = I_{Abs} * \phi \quad (2)$$

$$I_{Obs} = I_{Fl} * 10^{-\frac{\varepsilon_{Ex} * c * d + \varepsilon_{Em} * c * d}{2}} \quad (3)$$

$$\frac{I_{Obs}}{I_0} = (1 - 10^{-\varepsilon_{Ex} * c * d}) * \phi * 10^{-\varepsilon_{Em} * c * d} \quad (4)$$

$$\frac{d\left(\frac{I_{Obs}}{I_0}\right)}{dc} = \ln(10) * \varepsilon_{Ex} * d * \phi * 10^{-\varepsilon_{Em} * c * d - \varepsilon_{Ex} * c * d} - \ln(10) * \varepsilon_{Em} * d * \phi * (1 - 10^{-\varepsilon_{Ex} * c * d}) * 10^{-\varepsilon_{Em} * c * d} \quad (5)$$

$$\frac{d\left(\frac{I_{Obs}}{I_0}\right)}{dc} \Big|_{c=0} = \ln(10) * \varepsilon_{Ex} * d * \phi \quad (6)$$

$$\frac{I_{Obs}}{I_0} = \ln(10) * \varepsilon_{Ex} * d * \phi * c \quad (7)$$

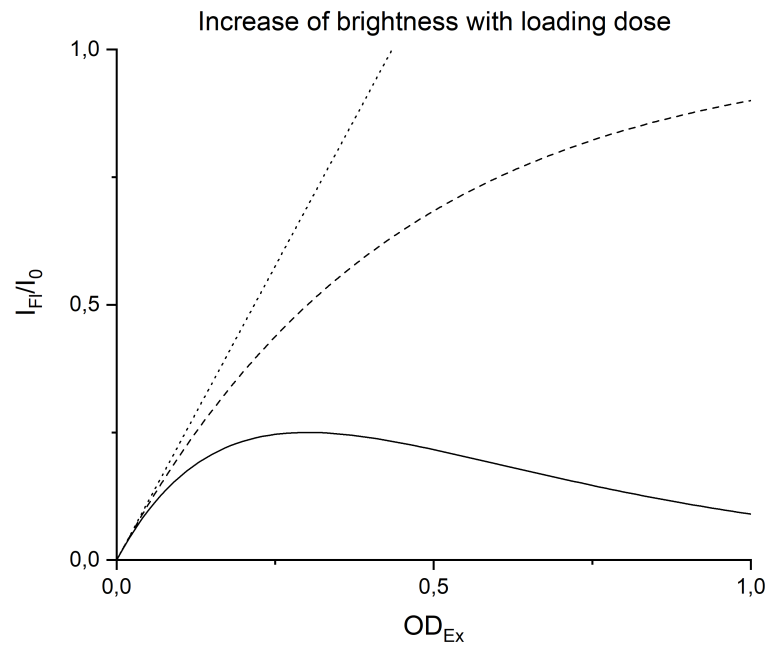


Figure 8: Brightness as function of loading dose, represented by the optical density at excitation wavelength, for $\phi=1$ and $OD_{Em}=OD_{Ex}$ (solid line) or $OD_{Em}=0$ (segmented line), calculated with **Equation 4** and tangent at $OD_{Ex}=0$ (dotted line), calculated with **Equation 7**.

2.1.4 NP size and surface properties

The NP size might have an impact on signal intensity of LFI. For example, gold NP for detection of potato virus X showed a LOD of 80 ng/mL for particle a size of 6.4 nm, but a LOD of only 3 ng/mL for a size of 33.4 nm.⁷⁵ A gold based LFI for detection of nucleotides showed increased signal intensity of NP sizes of 80 nm over 40 nm, but decreased intensity for 150 nm over 80 nm.⁷⁶ Fluorescently labelled phages with biotinyl moieties flowing through a glass fibre membrane coated with NeutrAvidin showed different binding to the membrane dependant on size and aspect ratio. The maximum number bound to the area of interest was 150, 375 and 350 for phages with dimensions of 13x200 nm, 6x900 nm and 6x2000 nm, respectively. The size-dependence of signal intensity with spherical NP in fluorescence-based LFI has not been studied yet.

The flow through the membrane is possible for a wide range of NP sizes, as existing LFI utilize NP with diameters between 15 and 800 nm.⁷⁷ However, using iron oxide magnetic beads, it was observed that clogging of the membrane was much more likely for NP with irregular shape, large diameter and broad size distribution compared to small regular shaped particles with narrow size distribution.⁷⁸ Apart from geometry, the surface chemistry determines aggregation behaviour to a great extent. To prevent aggregation, both electrostatic repulsion and steric hinderance are possible. A measure for electrostatic repulsion of dispersed matter is the zeta potential, the coulomb potential at the shear plane of a moving particle. **(Figure 9)**

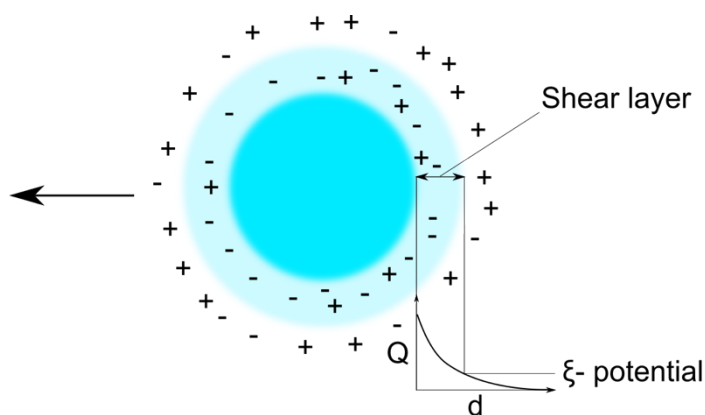


Figure 9: Scheme depicting the zeta potential as the charge Q at the distance from the particle surface d of the slipping plane of the shear layer of a moving particle.

In biological matrices the ion strength is high due to dissolved electrolytes. An increase in ion strength decreases the thickness of the shear layer, reducing electrostatic repulsion. Thus, if only electrostatic repulsion contributes to the colloidal stability, the zeta potential has to be at least about $30 \pm \text{mV}$.⁷⁹ Both pH of the dispersant and material of the NP influence the zeta potential.⁸⁰

Furthermore, an increase of the absolute value of the zeta potential is achieved by incorporation of surface groups with high dipole momentum or ionic groups. Alternatively, bulky surface groups can be attached to the NP surface to prevent aggregation through steric hinderance without substantially changing the zeta potential. For the use in biological matrices the most common are surface modifications are poly(ethylene glycol), poly(maleic anhydride), lipid bilayers, protein coatings, glycans and aptamers.⁸¹ The use of bulky groups is not restricted to prevention of aggregation, but can also increase signal quality in LFI. For example, methoxy-polyethylene glycol-thiol (mPEG-HS) was used to backfill gold NP covalently conjugated to antibodies. The samples with mPEG-HS-decorated surfaces showed slightly higher signal intensity per area compared to NP without backfilling.⁸² The presumed mechanism behind the increase of signal quality was the reduction of non-specific binding, an effect that is common for this surface chemistry, as PEG moieties are known to reduce adsorption of proteins.⁸³

2.1.5 Surface modification with detection moieties

In addition to optimal optical properties, the signal transducer should have a functionalised surface for conjugation of the detecting moiety, typical an antibody. The possible conjugation chemistry is depending on the functional group on the antibody surface that is desired to be conjugated. **(Figure 10a)** Depending on the conjugation strategy a certain functional group on the NP surface is necessary. **(Figure 10b)**

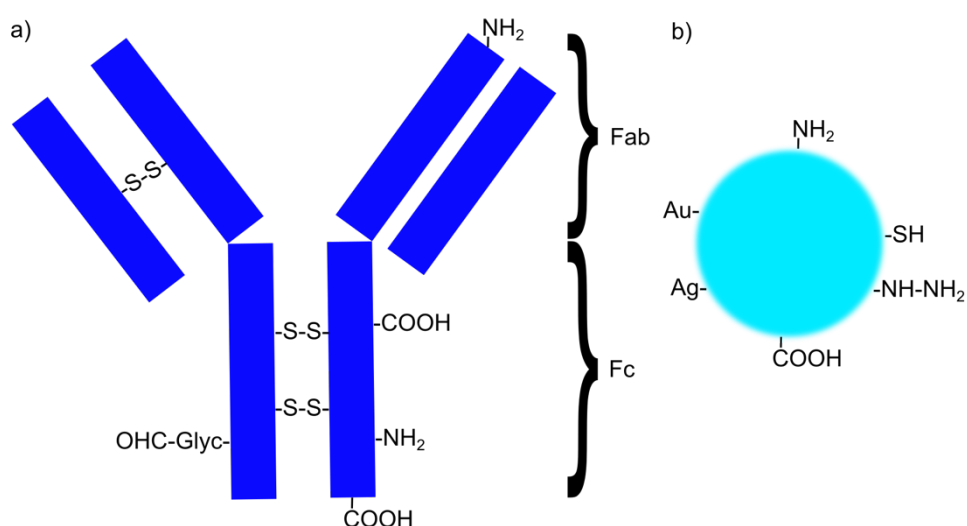


Figure 10: Available conjugation sites at the antibody (a) and linkable functional groups on the NP surface (b).

The antibody can be either directly attached to the NP or bound via a linker molecule that acts as steric spacer and may add an additional functionality to the antibody or NP. Both directional and non-directional conjugation strategies are possible. (**Figure 11**)

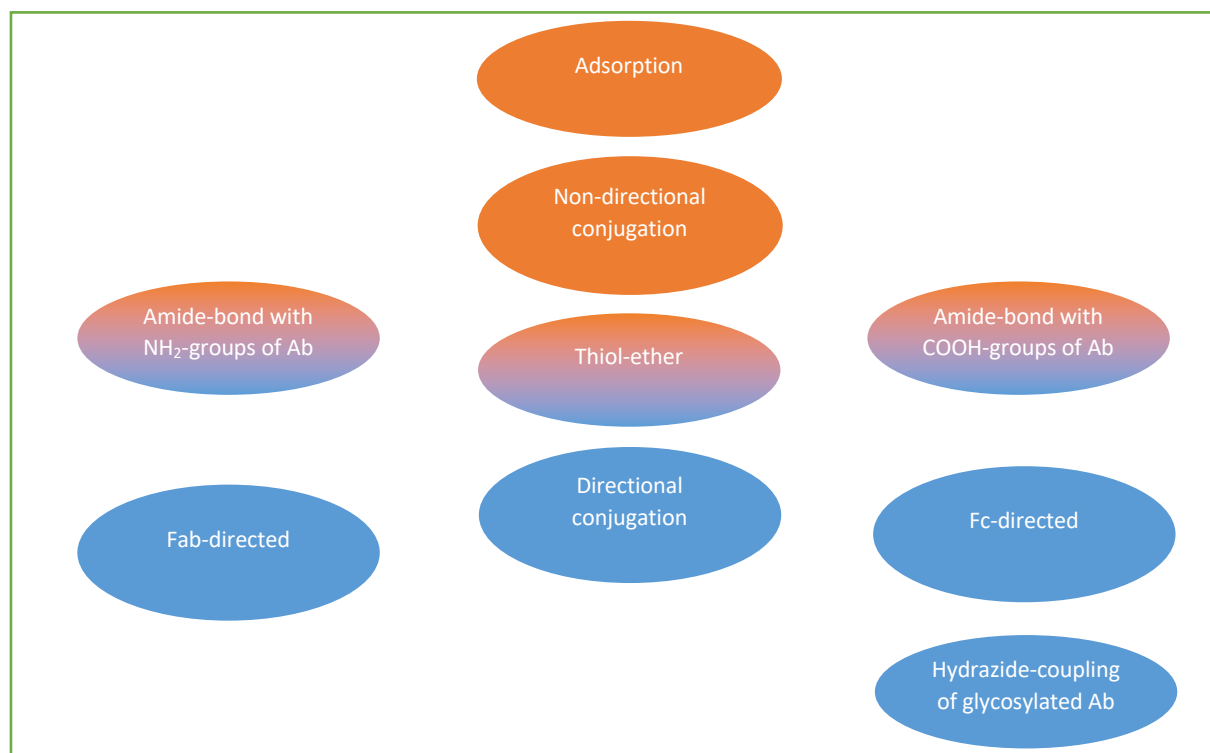


Figure 11: Possible strategies to conjugate antibodies to NP.

While passive adsorption of the detection moiety to the NP is a very simple method, covalent binding approaches can lead to higher sensitivity of the LFI. For example, a LFI for the detection of dengue NS1 protein based on gold NP showed a smaller LOD for covalently conjugated compared to passively adsorbed antibodies with 13 ng/mL and 34 ng/mL, respectively.⁸² A common conjugation reaction of antibodies to NP is the formation of an amide bond between carboxylic groups on the NP and amine groups on the antibodies, mediated by 1-ethyl-3-(3-dimethylaminopropyl) carbodiimide (EDC).^{84–86} The conjugation takes place in two steps, an activation step and the coupling step. (**Figure 12**) First, EDC reacts with the carboxylic group to form an *O*-acylisourea. This compound might be reacted with *N*-hydroxysuccinimide (NHS) to form a more stable ester, if isolation of the intermediate is desired. Either of the compounds then reacts with an amine-group to form an amide-bond between antibody and NP or a linker molecule and either of both.

The two stages of reaction might be separated by a washing step to remove excessive EDC or as a one-pot reaction with a chance of polymerisation of some antibody, as antibodies bear both amine- and carboxylic groups.

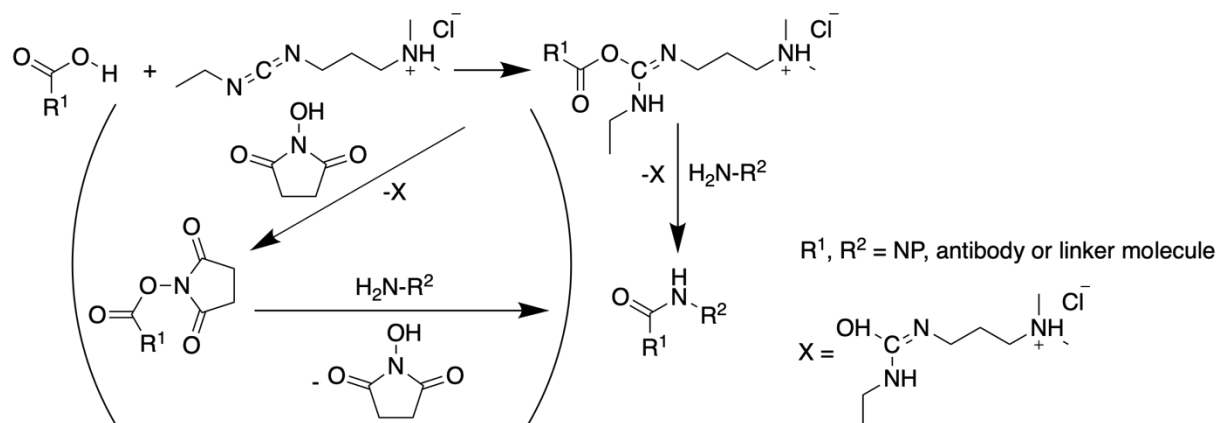


Figure 12: Reaction scheme of coupling of a carboxylic group to an amine mediated by EDC with and without NHS.

In the case of a one-pot reaction, the polymerisation of antibodies is reduced if the pH of the coupling reaction is different from the isoelectric point of the antibody, as the antibody zeta potential leads to electrostatic repulsion. The reaction conditions also play a major role on yield and orientation of conjugate formation and therefore have to be either adopted from literature or assessed experimentally. For example, superparamagnetic NP with carboxylic acid functional groups have been conjugated using different ratios of EDC and antibody to NP, as well as different pH for activation and coupling. It was found, that, if the other conditions were kept optimal, a pH for the activation step of 5.0 was favourable over a pH of 6.0 leading to a number of conjugated antibodies per NP of 5200 and 4300, respectively.⁸⁷ Likewise, when the coupling pH was increased from 5.0 to 6.5, the number of antibodies per NP decreased from 5200 to 1400. When the number ratio of EDC to carboxylic groups was decreased from 2.0 to 0.5, the antibody coverage decreased from 5200 to 800 antibodies per NP. If the antibody amount was decreased from 100 µg/mg NP to 20 µg/mg NP, the number of conjugated antibodies per NP decreased from 5200 to 3000. The orientation of the antibodies was also affected by the reaction conditions. The highest accessibility of the Fab domain was achieved by high antibody amount, high EDC to carboxylic group ratio, low activation pH and low coupling pH. The highest accessibility of the Fc region was not only found for the same conditions as for the Fab regions, but also for low antibody amount, low EDC to carboxylic group ratio, high activation pH and high coupling pH.

For a lateral flow immunoassay, the Fab domain of the antibody has to be accessible and the reaction conditions therefore be chosen accordingly. It has to be noted though, that the use of a spacer for the coupling reaction increases accessibility of both antibody regions.^{88,89} For a high yield of the conjugation reaction it is furthermore necessary to make sure the NP suspension is free of reactive species other than those bound to the NP surface. If the NP preparation is not intrinsically excluding unbound functional groups, they have to be removed in a reaction work up.

2.1.6 Study questions and hypotheses

For a sensitive LFI an intense optical response of the signal transducer is desired. Therefore, the first question that has to be answered is if CP are bright fluorophores and if encapsulation within different NP architectures has an effect on brightness. To address this, two NP architectures were chosen for study: silica-shell cross-linked polymeric micelles (Si-NP) and Pdots.^{41,71} The CP chosen for investigation were PDOF and CN-PPV, as well as a blend of the two. PDOF was chosen for its high brightness, although its Stokes' shift is smaller than CN-PPV. CN-PPV in contrast has a moderate brightness, but a larger Stokes' shift.

Secondly, good flow through the LFI membrane, as well as attachment of a detection moiety are necessary as well. In this study, it was investigated whether CP encapsulated in NP have the right size and surface chemistry for sufficient flow through the LFI membrane. Existing NP systems for LFI typically use NP in size ranges from 15 nm to 800 nm.⁷⁷ Literature reports for both Si-NP and Pdots indicate that their size and surface properties will be in the ideal range for optimal LFI performance.^{41,71}

Perhaps more critical is the investigation of how the fluorophore loading in the Si-NP and Pdots can be increased to increase NP brightness. For small molecule fluorescent dyes, it was shown that an increased number of dye molecules per NP does increase the brightness.⁶³ The hypothesis is therefore, that an increase in CP loading increases brightness as well.

Once the CP NP properties were optimised, a model antibody comprised of the IgG fraction of rabbit serum was used to assess conjugation efficiency to the NP surface. Even though the IgG does not bind a single specific antigen, it bears the same functional groups as other antibodies, which is crucial to investigate the coupling reaction. Efficacy of the conjugation reaction and the different NP systems as signal transducers was assessed in a simplified ELISA using anti-rabbit IgG as the capture antibody, as well as in an LFI dipstick test. Two reference NP systems were used in these studies: 1) commercially available carboxylated polystyrene NP (PS-NP; 50 nm) labelled with an undisclosed small molecule dye ($\lambda_{\text{Ex}}=366$, $\lambda_{\text{Em}}=406$) and 2) gold NP (Au-NP; $\lambda_{\text{Abs}}=534$ nm). The PS-NP were used to compare the performance of CP NP to another fluorescently labelled NP system and the Au-NP were chosen for comparison with the standard signal transducers in LFI assays. From the data generated in this chapter, optimised CP NP would be taken forward into Chapter 3 to investigate NP performance in a model LFI using anti-rabbit IgG as capture antibody.

2.2 Materials and Methods

2.2.1 Materials

Poly-(9,9-di-*n*-octyl-fluorenyl-2,7-diyl) (PDOF), poly-(2,5-di-hexyloxy-cyanoterephthalylidene) (CN-PPV), tetrahydrofuran (THF), Pluronic® F127, anhydrous *N,N*-dimethylacetamide, succinic anhydride, diethyl ether, tetramethoxysilane, phosphate buffered saline (PBS), 1-ethyl-3-(3-dimethylaminopropyl)carbodiimide (EDC), 1-Hydroxy-2,5-pyrrolidinedione (NHS), 2-(*N*-morpholino)ethanesulfonic acid (MES), Rabbit IgG from Rabbit serum, ethanolamine, sodium tetraborate, bovine serum albumin (BSA), sodium azide and colloidal gold (Au-NP) 40 nm in 0.1 mM PBS were bought from SigmaAldrich. Polystyrene-graft-(ω -carboxylic acid polyethylene glycol) (PS-g-PEG-COOH) with $M_n(\text{PS})\text{-}g\text{-}M_n(\text{PEG})=6\text{kDa-g-}3.7\text{kDa}$ and 10 branches of PEG per PS backbone was acquired from Polymersources, CA. Fluoresbrite® BB carboxylate microspheres 0.05 μm (PS-NP) were from Polysciences Europe. The Spectra/POR 6 dialysis membrane was acquired from Spectrumlabs. The LFI components Immunopore RP and CF6 were from GE Healthcare LifeSciences, UK.

2.2.2 Optical characterisation of CP in solvent (THF)

All measurements were performed using a Horiba FluoroMax 4 and quartz cuvettes with a light path length of 1 cm. Excitation and emission spectra were recorded at a fluorophore concentration of 10 $\mu\text{g/mL}$. The second-order solvent scattering peak in the CN-PPV spectra was masked by subtraction of the pure solvent spectrum. For determination of maximum extinction coefficient THF solutions were prepared at concentrations of 0.2, 0.4, 1, 4, 10 and 20 $\mu\text{g/mL}$ (PDOF) and of 0.05, 0.1, 0.5, 1, 2.5, 5, 10, 25 and 50 $\mu\text{g/mL}$ (CN-PPV). Concentration was plotted against absorption values and fitted linear with the equation $\text{Abs}=m \cdot c$ [$\mu\text{g/mL}$]. The fitting parameters were $m=0.0978$, $R^2=0.999$ (PDOF) and $m=0.0258$, $R^2=0.999$ (CN-PPV). The slope of the fitting line was used as the extinction coefficient. QY were measured as absolute values using an integrating sphere at a concentration of 1 $\mu\text{g/mL}$ for PDOF and 4 $\mu\text{g/mL}$ for CN-PPV. Emission spectra of the CP solutions and pure THF were recorded including the Rayleigh-peak. The QY was calculated from the area under the curves of Rayleigh-peaks (A_{Ex}) and emission peaks (A_{Em}) according to **Equation 8**:

$$\Phi = \frac{A_{Em}(CP) - A_{Em}(THF)}{A_{Ex}(THF) - A_{Ex}(CP)} \quad (8)$$

The values were internally corrected for wavelength-dependent reflectivity of the sphere by the evaluation software FluorEssence using a correction file specific to the integrating sphere used.

2.2.3 Preparation, purification and product yield: Si-NP and Pdots

2.2.3.1 Carboxylation of Pluronic F127

Pluronic® F127 (6.3 g, 0.5 mmol) was dried under reduced pressure at 100 °C for 24 h. Dry *N,N*-dimethylacetamide (60 mL) was added under nitrogen atmosphere and heated to 70 °C to form a clear solution. Succinic anhydride (0.2 g, 2.0 mmol) was added under vigorous stirring at 70 °C. The reaction mixture was heated to 90 °C and further stirred under nitrogen atmosphere for 24 h. The mixture was cooled to room temperature and precipitated against excess cold diethyl ether two times in a dropwise manner. The precipitates were dissolved in deionised water and dialysed against deionized water for 48 h using a Spectra/POR 6 dialysis membrane with MWCO of 1 kDa. The solution was then freeze-dried to obtain the bis-carboxylic acid modified Pluronic® F127 (F127-COOH) (3.2 g, 51%). ¹H NMR (400 MHz, CDCl₃) δ= 4.26 (*m*, 4H, -COO-CH₂-), 3.64 (*m*, 400H, -CH₂-CH₂-), 3.54 (*m*, 112H, -CH₂-CH-), 3.39 (*m*, 56H, -CH-), 2.64 (*m*, 8H, -OOC-CH₂-CH₂-COO-), 1.14 (*s*, 168H, -CH₃) ppm.

2.2.3.2 Si-NP preparation

Pluronic® F127 (80 mg) and F127-COOH (20 mg) was mixed with a solution of the CP in THF (i.e. 15, 200 and 500 µL for loading doses of 0.1, 2 and 4%, respectively, 5 g/L) and THF was added to a total volume of 1.2 mL. The mixture was heated to 45 °C and stirred for 30 min. The solution was cooled to room temperature and tetramethoxysilane (65 µL) was added while stirring. The mixture was rapidly injected in deionised water (10 mL) under ultrasonication and sonicated for 13 min. The suspension was stirred in an open flask for 4 days in a low-airflow environment to complete hydrolysis and to evaporate the THF. Following evaporation, the mixture volume was replenished to 10 mL with deionised water and filtered through a 0.2 µm syringe filter to remove large particulates.

Si-NP without F127-COOH were prepared with 100 mg Pluronic® F127 instead.

To remove excess surfactant, 5 mL of the NP suspension were transferred into a centrifuge filter tube with MWCO=100 kDa and 10 mL water were added. The mixture was reduced to 2 mL by ultrafiltration and water added to a total suspension volume of 15 mL.

The filtration procedure was repeated 3 times and water added to a final volume of 5 mL afterwards. 1 mL of the crude and washed suspension was pipetted in previously weighted centrifuge tubes, freeze dried and weighted again to calculate the total solids content. The NP yield was calculated as total solids content divided by theoretical total solids content.

2.2.3.3 Pdot preparation

PDOF or CN-PPV in THF (200 μ L, 1 mg/mL) and PS-g-PEG-COOH in THF (20 μ L, 2 mg/mL) were mixed together in 5 mL THF. The mixture was sonicated for 15 s and subsequently injected into 10 mL of water under violent sonication. THF was removed by heating the mixture to 70 °C and purging with dry nitrogen for 25 min. The suspension was cooled to room temperature and deionised water was added to a final volume of 10 mL. The mixture was slowly filtered through a 0.22 μ m syringe filter to remove dust and precipitated polymer.

2.2.4 Physicochemical characterisation: Si-NP, Pdots, PS-NP and Au-NP

The hydrodynamic diameter and zeta potential of NP was measured by DLS using the Malvern Zetasizer ZS Nano with a 633 nm laser and a scattering angle of 173°. The samples were diluted in deionised water to give a number of counts per second of less than 150000. The sizes reported are mean values of number distributions calculated by the Zetasizer Nano software v3.30. For zeta potential measurements 10 mM KCl was used as the electrolyte. The electrophoretic mobilities were transposed to zeta potentials by the Zetasizer Nano software using the Smoluchowski approximation.⁹⁰

2.2.5 Characterisation of optical properties: Si-NP, Pdots and PS-NP

QY and spectra were measured as described in Chapter 2.2.2. Suspensions were diluted prior to QY measurement to optical density values between 0.05 and 0.1. The CP content of the NP suspensions was determined by absorption measurement using THF solutions of the polymers as calibration curve. The encapsulation efficiency was calculated as CP content divided by amount of CP used for NP production. The effective loading dose was defined as the measured CP content divided by the total solids content of washed NP suspensions.

2.2.6 Antibody conjugation: Si-NP, Pdots, PS-NP and Au-NP

2.2.6.1 Conjugation of Si-NP, Pdots and PS-NP

NP suspension (40 µg NP), a solution of PEG400 in water (40 µL, 50 g/L) and HEPES buffer (40 µL, 1 M, pH=7.4) were mixed and water was added to a total volume of 2 mL. Solutions of freshly prepared NHS in water (10 µL, 1 g/L) and EDC in water (40 µL, 1 g/L) were added and stirred for 5 min. A solution of rabbit IgG in water (367 µL, 36.7 µg, 0.1 g/L) was added and the mixture was stirred for 2 h at RT. A solution of BSA in water (10 µL, 100 µg, 10 g/L) was added and the suspension was stirred for 30 min.

The resulting NP conjugate was purified by size exclusion chromatography (SEC) using Sephacryl 300-HR as stationary and HEPES buffer (20 mM, pH=7.4) containing 1% PEG400 as mobile phase. The NP containing fractions were concentrated to 1 mL by ultrafiltration (MWCO=100 kDa) and BSA (10 mg) was added.

For optimisation of the conjugation conditions, rabbit IgG solutions of 550.5, 367, 183.5, 50, 25 or 10 µL (55.1, 36.7, 18.4, 5, 2.5 or 1 µg, 0.1 g/L), corresponding to 75%, 50%, 25%, 75, 35 or 1% of theoretical antibody surface coverage of NP were used. Alternatively, for investigation of the effect of pH on the conjugation reaction, MES buffer (40 µL, 1 M, pH=6.5) was used instead of HEPES together with rabbit IgG solutions of 367, 183.5, 73.4, 25, 12.5 or 5 µL (73.4, 36.7, 14.7, 5, 2.5 or 1 µg, 0.2 g/L), corresponding to 100%, 50%, 20%, 7%, 3% or 1% of theoretical antibody surface coverage of NP.

2.2.6.2 Adsorption of Ab to the Au-NP surface

Au-NP were surface-modified with Ab according to literature.⁹¹ Briefly, rabbit IgG (12.45 µg, 83 pmol) in borate buffer (100 µL, 2 mM, pH=9) were mixed with a gold NP suspension (1.25 mL, 0.15 pmol, 58.2 µg) in borate buffer (0.25 mL, 2 mM, pH=9) for 2 min. The suspension was centrifuged (3220 x g, 4 °C, 30 min), the upper layer was removed and the Au-NP were redispersed in PBS (1 mL) containing BSA (10 mg) and sodium azide (0.5 mg).

2.2.7 LFI dipstick tests

Nitrocellulose membrane Immunopore RP (4x25 mm) was fixed on an adhesive plastic backing together with CF6 wicking pad (4x25 mm), overlapping 8 mm. A line of anti-rabbit IgG (0.2 g/L) with a width of 1 mm was drawn on the nitrocellulose membrane at a distance of 4 mm to the wicking pad with a fountain pen and the membrane dried for 10 min at room temperature.

Wells of a 96-well plate were filled with a mixture of IgG-Pdot conjugates (10 μ L), diluted to a conjugated polymer concentration of 2 μ g/mL with HEPES buffer (20 mM, pH=7.4) containing 1% PEG400, and a solution of 1% Triton X-100, 1% BSA and 1% PEG400 (50 μ L). The strips were dipped in the mixture for 5 min and successively dried in vacuum at room temperature. The signal intensity was read with a QIAGEN LFReader at $\lambda_{Ex}/\lambda_{Em}$ =365/430 nm.

2.2.8 Fluorescence-linked immunosorbent assay (FLISA) of IgG-NP conjugates

Anti-rabbit IgG in 0.1 M borate buffer (50 μ L, 1 μ g, 20 μ g/mL, pH=9) was pipetted in wells of a 96-well plate. The plate was covered with Parafilm and incubated at 4 °C overnight. The coating solution was removed and the wells were washed twice with 200 μ L PBS containing 0.05% (w/w) Tween 20 (PBST). Remaining binding sites were blocked by adding a solution of BSA in PBS (150 μ L, 50 g/L), covering with Parafilm and incubating for 2 h at room temperature. The plate was washed twice with 200 μ L PBST. IgG-NP-conjugate diluted in PBST containing 1 mg/mL BSA (100 μ L, 3, 2, 1, 0.5, 0.1 and 0 mg/L, 300, 200, 100, 50, 10 and 0 ng) was added. The plate was covered with Parafilm and incubated at room temperature for 2 h. The plate was washed three times with 200 μ L PBST and filled with 200 μ L PBST. Blank wells were prepared without addition of anti-rabbit IgG, but blocking with BSA in PBS (150 μ L, 50 g/L). The signal intensities were measured with a Biotek Cytation5 plate reader using the bottom optics. Si-NP, Pdots and PS-NP were measured in fluorescence endpoint/kinetic mode with a slit width of 20 nm and excitation/emission wavelengths of 378/437 nm (PDOF-Si-NP and -Pdots), 454/650 nm (CN-PPV-Si-NP and -Pdots) and 365/406 nm (PS-NP). The Au-NP were measured in absorption endpoint/kinetic mode at a wavelength of 534 nm. The signal-to-background ratio (SBR) was calculated as ratio of the mean intensity of wells containing capture antibody to the mean intensity of wells containing no capture antibody of same NP concentration.

2.3 Results and Discussion

2.3.1 Optical characterisation of CP in solvent (THF)

PDOF in THF solution was excited between 290 and 420 nm with a maximum at 381 nm and emitted in the blue region between 390 and 550 nm. The emission spectrum had a global maximum at 417 nm, a local maximum at 440 nm and a shoulder at 468 nm (**Figure 13a**). The THF solution of CN-PPV was excited between 290 and 550 nm with a global maximum at 442 nm and a local maximum at 332 nm. CN-PPV fluorescence emission took place in the yellow-to-red region between 450 and 750 nm with a maximum at 545 nm (**Figure 13b**). CN-PPV showed a Stokes shift of 128 nm, more than twice that of PDOF (61 nm).

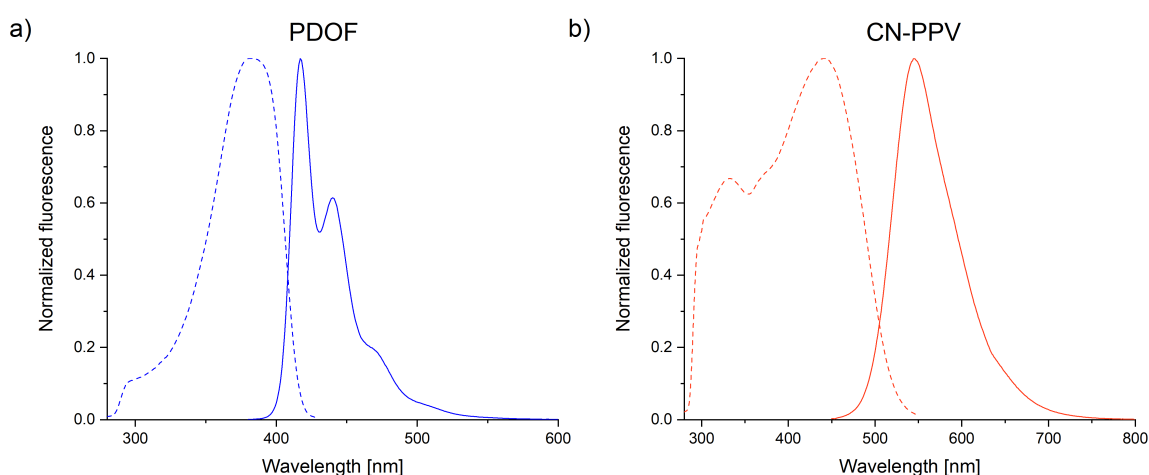


Figure 13: Normalised fluorescence spectra of PDOF (a) and CN-PPV (b) in THF. Dotted and straight lines are excitation and emission spectra, respectively at a concentration of 0.5 $\mu\text{g/mL}$.

As shown in Chapter 2.1.3, the brightness of NP sensors increases with extinction coefficient and QY of the fluorophore. The maximum extinction coefficient of PDOF ($97.9 \text{ L}\cdot\text{g}^{-1}\cdot\text{cm}^{-1}$) was almost four times the extinction coefficient of CN-PPV ($25.8 \text{ L}\cdot\text{g}^{-1}\cdot\text{cm}^{-1}$). A comparison of optical properties to other well-known dyes used in LFI is listed below. (**Table 3**)

Table 3: Comparison of published optical properties of fluorescent dyes used in LFI.

Dye	ϵ [$\text{L}\cdot\text{g}^{-1}\cdot\text{cm}^{-1}$]	QY [%]	Solvent	Reference
Phycoerythrin	6.4	82	PBS	92,93
$\text{Ru}(\text{phen})_3^{2+}$	24.0	58	Ethanol/Methanol (4:1)	63,94,95
CN-PPV	25.8	17.7	THF	
Cyanine-5 NHS	38.0	40	Ethanol	96,97
PDOF	97.9	98.6	THF	
Nile red	126.6	42	DMSO	98,99

The QY of the CP in THF solution was determined to be 98.6% at 1 $\mu\text{g/mL}$ for PDOF (48% in literature at 24 $\mu\text{g/mL}$ ¹⁰⁰) and 17.7% at 4 $\mu\text{g/mL}$ for CN-PPV (52% for 1 $\mu\text{g/mL}$ in toluene in literature^{101,102}).

2.3.2 Si-NP production and optimisation

For use as signal transducers, the produced NP are desired to have a high CP loading dose. The preparation method should also be easy, fast and give a pure product. For industrial manufacture it is furthermore important to have a high yield and minimum use of solvent and energy to reduce costs.

2.3.2.1 Synthesis and characterisation of F127-COOH

NP surfaces must be functionalised in order to perform as signal transducers in immunoassay applications. The requirement for functionalisation is reactive groups on the NP surface. In the current approach, F127-COOH was incorporated during nanoprecipitation. While all poloxamers, PEG-PPG-PEG triblock copolymers like Pluronic® F127, spontaneously form micelles in aqueous media, Pluronic® F127 is predicted to show the largest micelle core size of all solid poloxamers.¹⁰³ In CP-NP preparation, a large micellar core is advantageous, as more dye molecules can be incorporated in one NP. A higher number of dye molecules, in turn, increase fluorescence brightness, as shown in Chapter 2.1.3. F127-COOH was synthesised through Fischer esterification of the Pluronic® F127 OH-groups using the di-carboxylic acid anhydride succinic anhydride according to literature.⁷¹ (**Figure 14**)

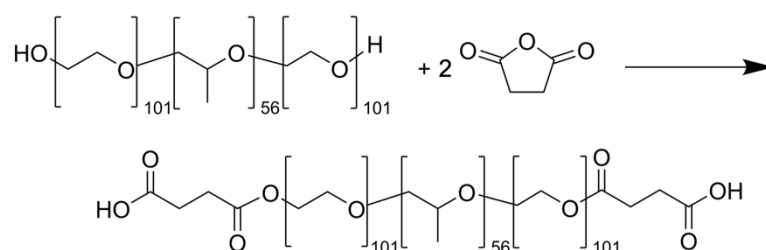


Figure 14: Reaction scheme for carboxylation of Pluronic® F127.

Use of the acid anhydride instead of the acid not only increased reaction speed, due to the higher electropositivity of the anhydride carbonyl carbon, but also did not produce water as reaction product. This improved the reaction yield to theoretically 100% conversion of OH-groups, because the back reaction of ester splitting requires water as reactant and was therefore prevented. A complete conversion of OH-groups was necessary because unreacted Pluronic® F127 is not easily removed during the reaction work up.

To further decrease water content and increase the yield, the Pluronic® F127 was dried by heating under reduced pressure prior to the reaction. More sophisticated drying procedures were unnecessary, as a small amount of water was needed for hydrolysis of a small percentage of the anhydride to produce an acidic catalyst. The reaction was performed at elevated temperatures of 90 °C to enhance the reaction kinetics. As the polyethylene glycol component of Pluronic® F127 is known to oxidise when in contact with air, an effect more prominent at elevated temperatures, the reaction was carried out under nitrogen atmosphere.¹⁰⁴ Small molecule by-products and impurities were removed by precipitation and subsequent dialysis of the polymer. The precipitation step was primarily responsible for yield reduction and led to a final yield of 51±2% (mean plus standard deviation of two batches).

The complete conversion of OH-groups was visible in ¹H-NMR, where new signals appeared at 4.26 and 2.64 ppm in comparison to Pluronic® F127 (**Figure 15**). The integral of the methyl group signal at 1.14 ppm was set to 168 for a number of 56 propylene glycol repetition units.¹⁰⁵ The integral of the signal of methylene groups of the succinic acid ester at 2.64 ppm was 8.00, matching a number of two functional groups per Pluronic® F127 molecule and indicating complete conversion. The same applied for the methylene group of Pluronic® F127 next to the ester group at 4.26 ppm with an integral of 4.02.

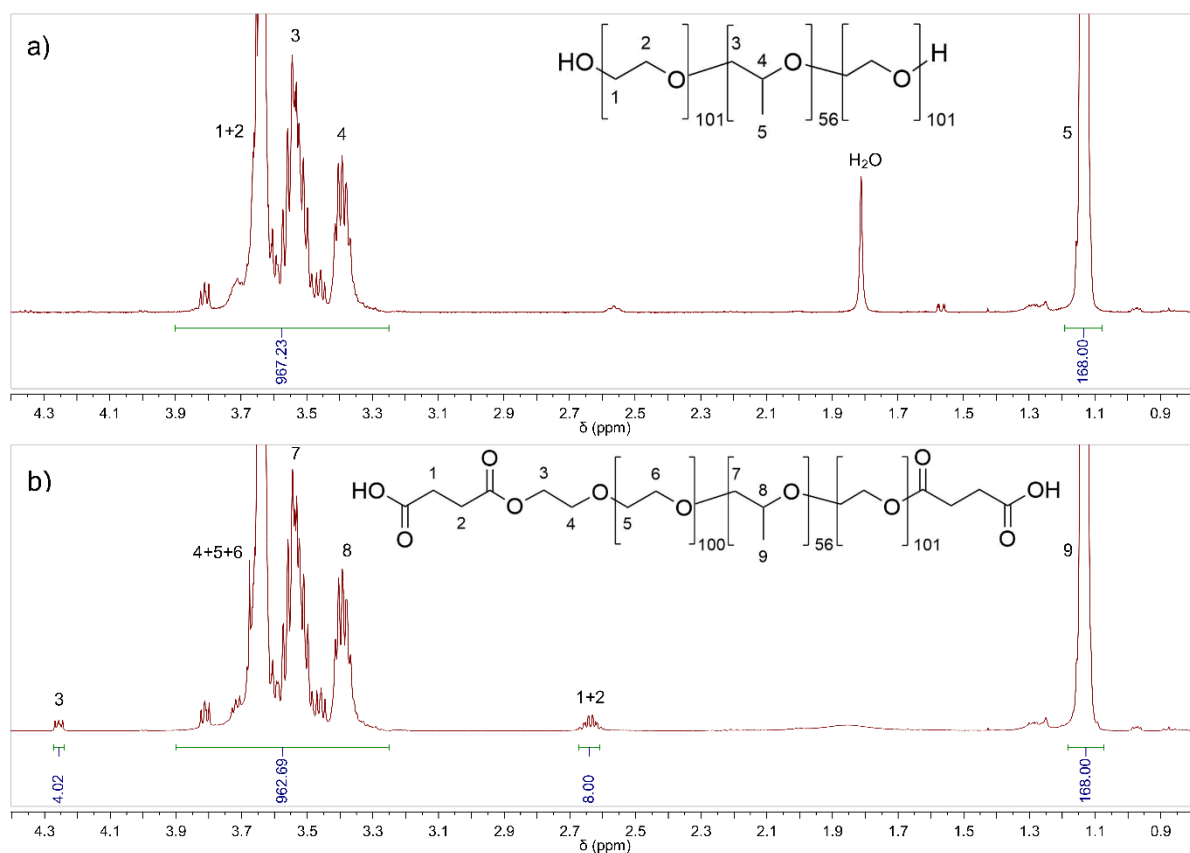


Figure 15: ¹H-NMR spectrum of Pluronic® F127 (a) and F127-COOH (b), recorded at 400 MHz in CDCl₃.

2.3.2.2 Si-NP production

To produce Si-NP, the organic phase containing the surfactant Pluronic® F127, the CP and tetramethoxysilane were injected into distilled water to form an oil-in-water (O/W) emulsion with a liquid tetramethoxysilane core stabilised by F127-COOH (**Figure 16**). The silane hydrolysed at the interface with water to form silicone dioxide, thereby cross-linking the surfactant molecules. THF was removed by stirring in an open container for 96 h at room temperature. This period was also necessary to complete hydrolysis of the tetramethoxysilane.^{71,106,107}

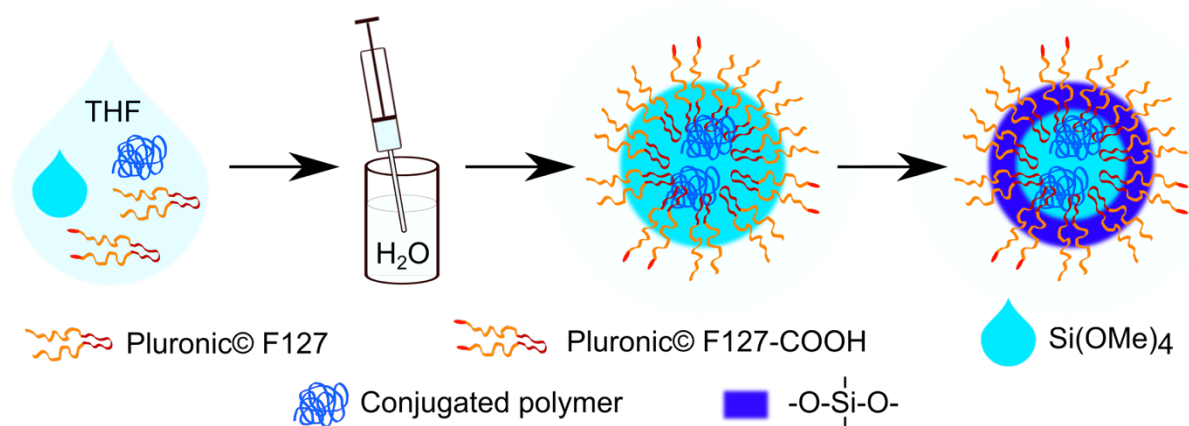


Figure 16: Preparation scheme of Si-NP.

Si-NP were prepared with both carboxylated and non-carboxylated Pluronic® F127 and then characterised to assess whether the carboxylic groups were present on the Si-NP surface. The zeta potential values of Si-NP prepared with F127-COOH were moderately but significantly ($P < 0.05$) more electronegative than non-carboxylated Si-NP, indicating the presence of carboxylic groups on the Si-NP surface. **(Figure 17a)** The size of Si-NP prepared with F127-COOH was significantly smaller compared to Si-NP without carboxylic groups ($P < 0.01$). **(Figure 17b)** TEM revealed that the decrease in size was due to a smaller core diameter. **(Figure 17c)** The difference in size was most likely caused by a difference in size of the Pluronic® F127 micelles before cross-linking. While Pluronic® F127 micelles were reported to have a hydrodynamic diameter of 27 ± 1 nm, F127-COOH micelles were found to be only 20 ± 4 nm in size.^{108,109} All Si-NP reported in later sections were prepared with F127-COOH and could therefore be considered to carry carboxylic surface groups.

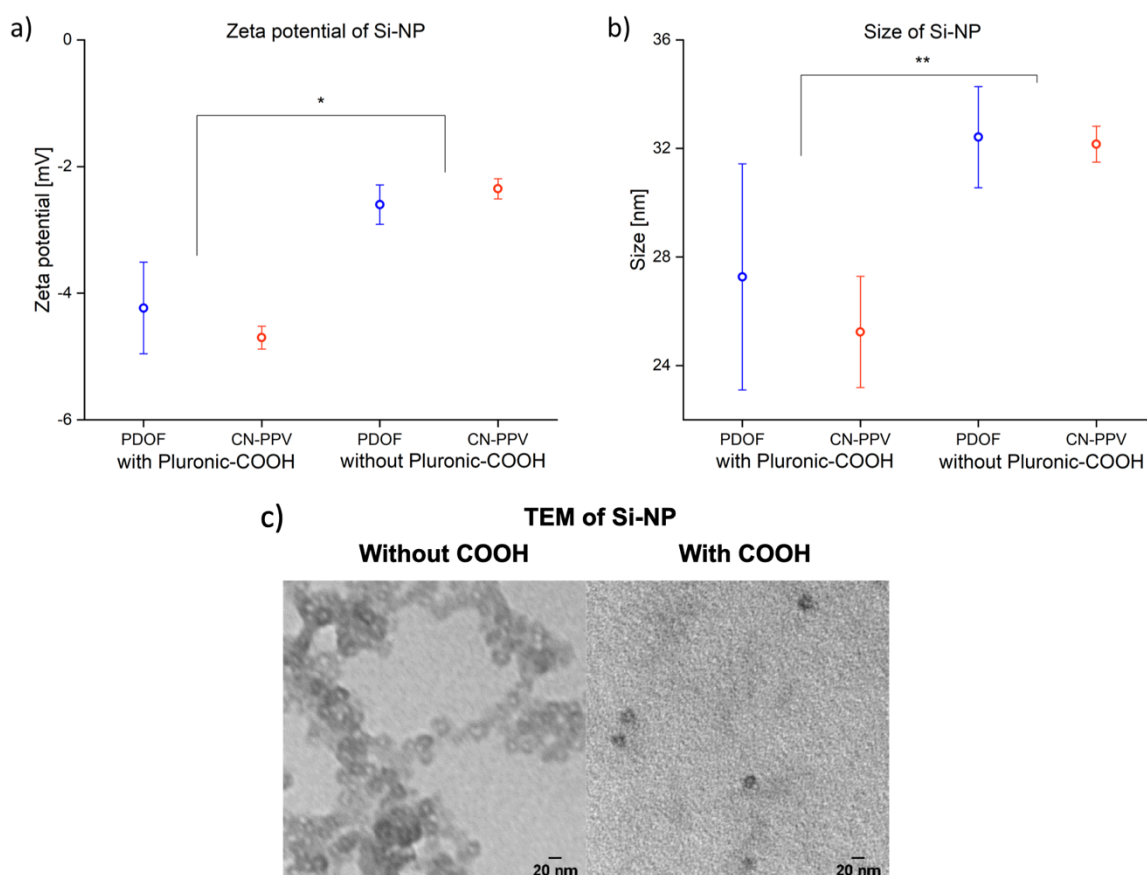


Figure 17: Zeta potential (a) and hydrodynamic diameter (b) of Si-NP prepared with and without F127-COOH (CP loading dose = 0.1%). Values represent the mean \pm standard deviation of $n=3$ batches. $*p < 0.05$; $**p < 0.01$ (Welch-test) TEM images of Si-NP prepared with and without F127-COOH (c).

2.3.2.3 Si-NP purification

As the content of Pluronic® F127 in Si-NP was very high, it was hypothesised that excess surfactant might reduce the efficiency of the subsequent antibody conjugation to the NP surface. But no study investigating the amount of free Pluronic® F127 in the NP suspension has been published until now. To assess the amount of free Pluronic® F127 in the system following Si-NP preparation, the crude suspension was washed four times with distilled water and the washing liquid was separated from the NP fraction using centrifugation filtration (MWCO 100 kDa). Each fraction was then freeze-dried and the solid content assessed by gravimetry. Following rigorous washing, only $36.5 \pm 9.2\%$ of Si-NP suspension dry mass consisted of the Si-NP fraction (**Figure 18a**). The washed NP were subsequently analysed by thermogravimetric analysis (TGA) which revealed that $\sim 59\%$ of the Si-NP mass consisted of Pluronic® F127, with $\sim 32\%$ SiO₂, $\sim 7\%$ CP and $\sim 2\%$ residual water (**Figure 18b**). It was therefore crucial to remove excess surfactant from Si-NP suspensions prior to antibody conjugation, a step unnecessary for Pdots, as the content of surfactant was low in general. Therefore, in all subsequent experiments, Si-NP were subjected to rigorous washing prior to further processing.

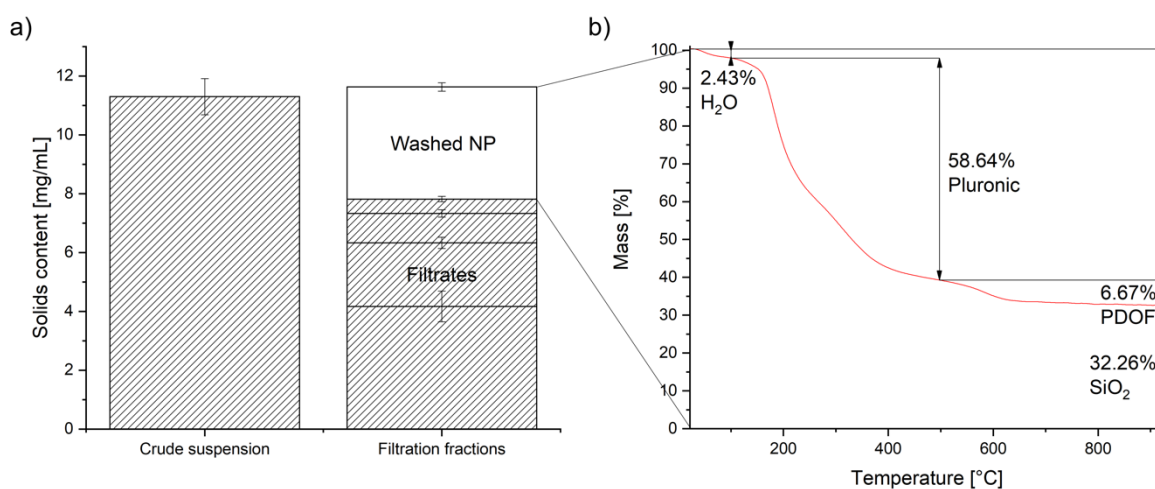


Figure 18: Composition of PDOF-Si-NP suspension with LD=4% after production. Solid content of crude Si-NP compared to that of washed Si-NP plus the dry mass in filtrate fractions (a). Values represent mean \pm standard deviation of $n=3$ Si-NP batches. TGA analysis of the washed NP fraction of a single Si-NP batch following lyophilisation (b).

2.3.3 Pdot production

Pdots were formed by nanoprecipitation of CP upon injection of a dilute CP and polymeric surfactant solution in THF into water (**Figure 19**). The THF was removed by stripping with nitrogen at elevated temperatures. The preparation was completed in 1 h, which was substantially faster than Si-NP manufacture. The removal of organic solvent could not be accelerated by elevated temperatures for Si-NP, as Pluronic® F127 solutions tend to gel upon temperature increase.¹¹⁰ Gelation was also observed, if the CP loading dose in Si-NP was higher than 4%, while Pdots could be produced at loading doses up to 83.3%.

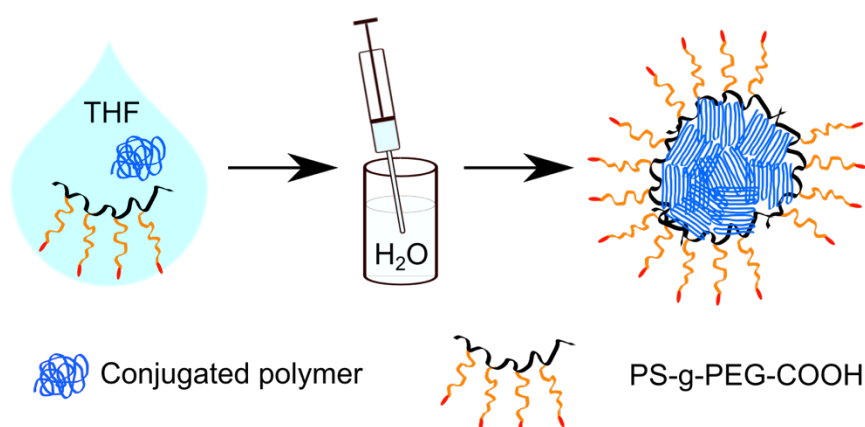


Figure 19: Preparation of Pdots.

A comparison of the key characteristics of the encapsulation methods is presented in **Table 4**. The comparison suggests, that the Pdots are advantageous over Si-NP from a preparative point of view.

Table 4: Key characteristics of Si-NP and Pdot preparation methods. *Mean and standard deviation of 4 batches.

	Si-NP	Pdot
Preparation time [h]	98	1
Yield (based on CP) [%]	62.4±12.4*	89.3±5.8*
max. theoretical CP loading dose [%]	4	83
CP concentration [µg/mL]	500	20

2.3.4 Comparison of physicochemical properties: Si-NP, Pdots, PS-NP, Au-NP

All examined NP showed about similar sizes of 30-45 nm. (**Figure 20**) Therefore, all NP systems had an appropriate size for signal transducers in LFI. CP loading did not influence the NP size, regardless of whether PDOF or CN-PPV was used (**Figure 20a**).

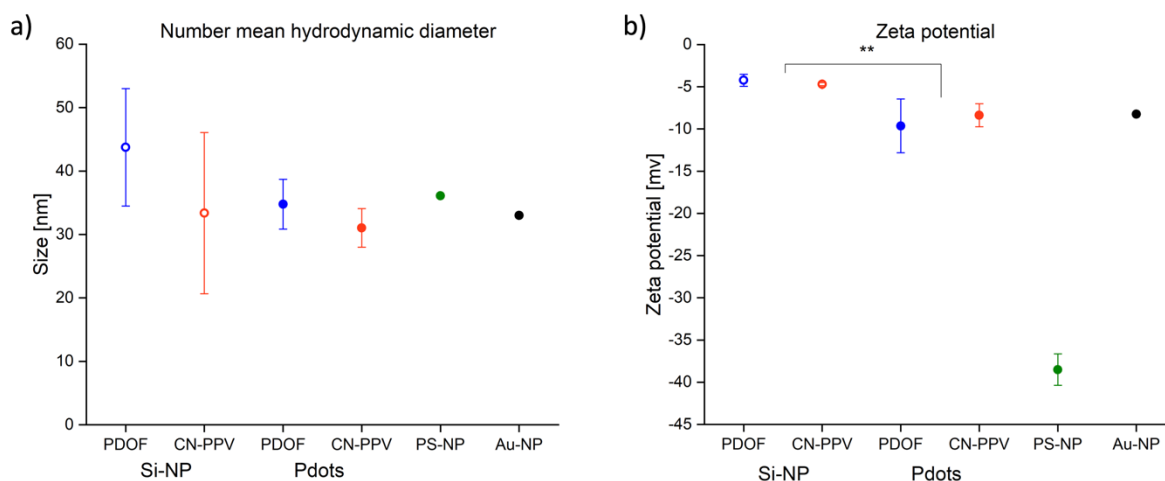


Figure 20: Number mean hydrodynamic diameter (a) and zeta potential (b) for different NP. Loading doses were 4% (Si-NP) and 83% (Pdots) Values represent mean \pm standard deviation of $n=3$ Si-NP and Pdot batches. One batch of PS-NP and Au-NP was measured in triplicate. $**p < 0.01$ (Welch-test)

The zeta potential was measured as both an indication of the number of carboxylic groups on the Si-NP, Pdot and PS-NP surface, as well as an indication of the colloidal stability. The Pdots and the Au-NP showed a similar ZP between -10 and -8 mV, while the ZP of Si-NP was significantly less electronegative, compared to Pdots. ($P < 0.01$, **Figure 20b**) The ZP of PS-NP was the most negative with approximately -39 mV. In general, a more neutral ZP is attributed with lower number of carboxylic groups and colloidal stability.^{111,112} However, PEGylated NP are reported as stable colloids, independent of ZP.¹¹³ Thus, all NP had an adequate colloidal stability for use in LFI.

Loading doses of up to 4% and 83% were used for Si-NP and Pdots, respectively, because high fluorophore loading doses are desired for signal transducers. As stated previously, loading doses of more than 4% led to gelation of Si-NP. No aggregation was observed with lower loading, but NP size was increased for LD=4%, compared to LD=0.1% ($P < 0.05$). (**Figure 21a**) CP loading dose did not affect the size of Pdots. (**Figure 21b**)

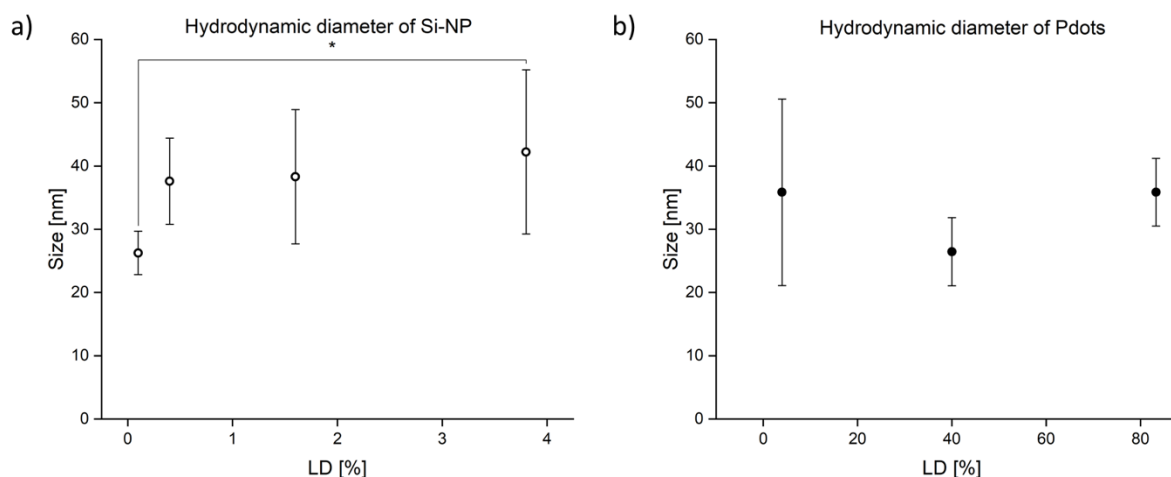


Figure 21: Hydrodynamic diameter of Si-NP (a) and Pdots (b) depending on CP loading dose. Values represent the mean \pm standard deviation of $n=3-5$ batches. * $p < 0.05$ (Welch-test).

2.3.5 Comparison of optical properties: Si-NP, Pdots and PS-NP

The absorption and emission spectra of PDOF- and CN-PPV-loaded Si-NP and Pdots exhibited the same shape and location of maxima independent of NP type. (**Figure 22**) PDOF NP showed a red-shift of the emission maximum of about 20 nm compared to THF in solution, but no shift in absorption maximum. CN-PPV showed a red-shift of the absorption maximum for Si-NP and Pdots of 20 and 10 nm, respectively. The emission maximum, however, was red-shifted by 80 nm for both Si-NP and Pdots compared to CN-PPV in THF. A similar red-shift was reported in literature for CN-PPV loaded Si-NP with a loading dose of 0.2%.¹⁰⁷ A red-shift of absorption and emission spectra is commonly observed for CP upon encapsulation in NP.¹¹⁴ The emission spectrum of PDOF-CN-PPV-Pdotes was the sum of the emission spectra of PDOF- and CN-PPV-Pdotes for excitation wavelengths smaller than 420 nm, but had the shape of only the CN-PPV-Pdot spectrum for excitation with lower-energy light. (**Figure 23**) The CN-PPV emission peak was blue-shifted compared to CN-PPV-Pdotes and -Si-NP to 620 nm. It was more intense than the PDOF emission peak over the whole excitation range, as well as much higher for excitation below 420 nm compared to higher excitation wavelengths. Thus, efficient energy transfer from the strong-absorbing PDOF to CN-PPV was indicated.

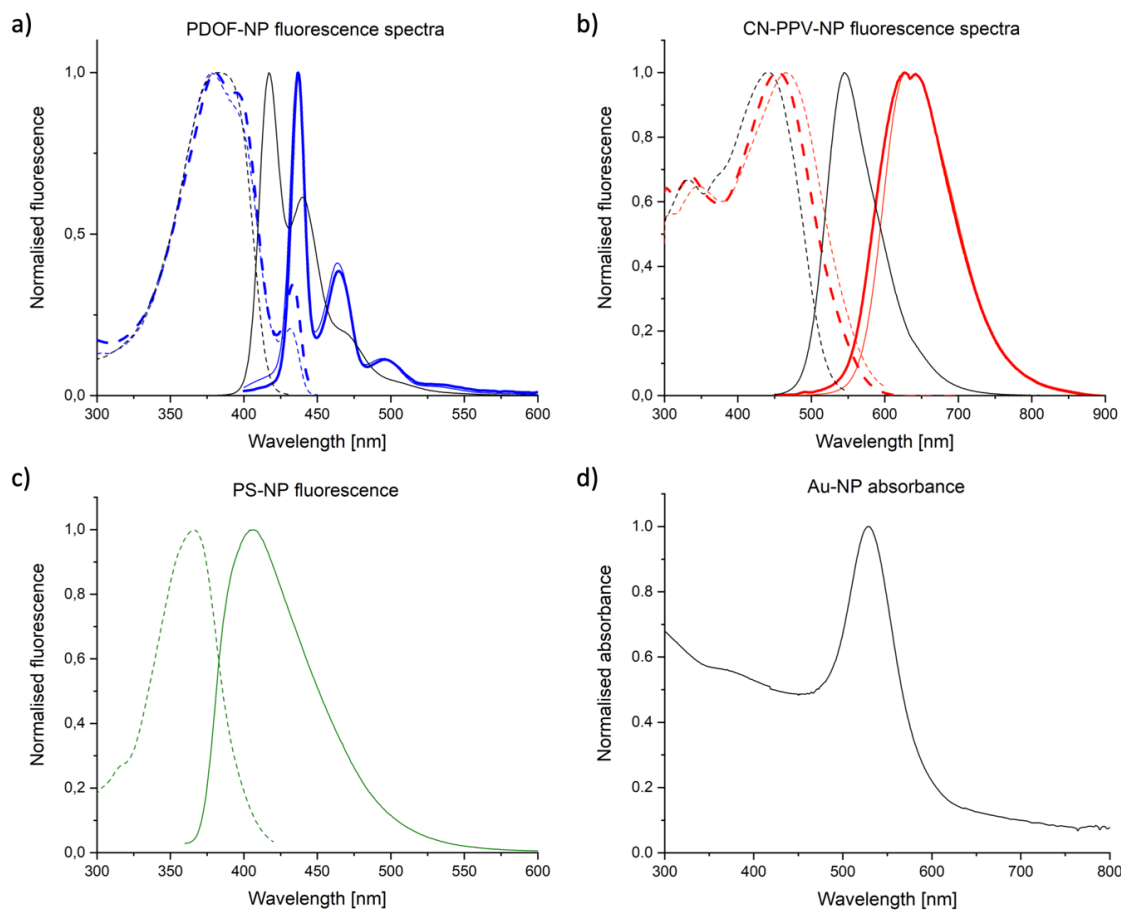


Figure 22: Absorption (dashed lines) and fluorescence (solid lines) spectra of THF solution (black) or Si-NP (thin lines) and Pdots (thick lines) loaded with PDOF (a) or CN-PPV (b). CP loading doses were 4% (Si-NP) and 83% (Pdots). Absorption (dashed line) and fluorescence (solid line) spectra of PS-NP (c). Absorption spectrum of Au-NP (d).

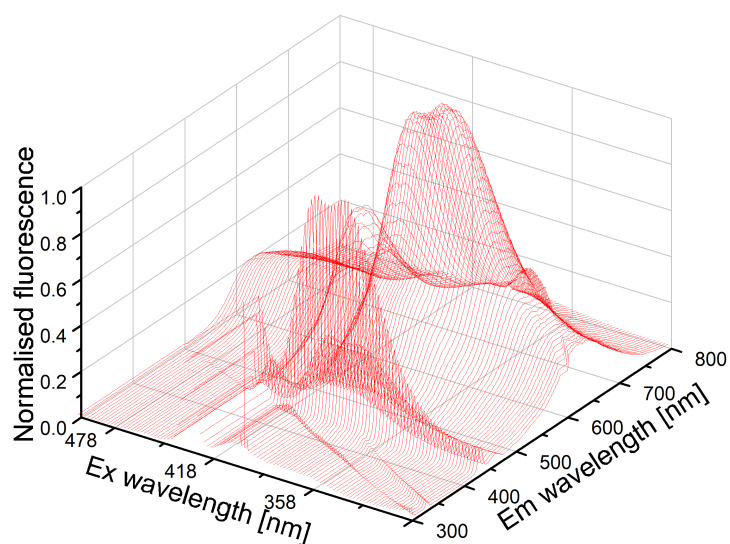


Figure 23: Combined excitation-emission fluorescence spectrum of PDOF-CN-PPV-Pdots. CP loading dose was 83% in total with a 1:1 ratio of PDOF and CN-PPV. The first order Rayleigh peak was removed by the evaluation software FluorEssence.

Compared to commercial PS-NP, the Stokes shifts of Si-NP and Pdots were higher (**Table 5**). On the other hand, PS-NP showed a much higher QY. However, as the loading dose of the NP was unknown, the brightness had to be evaluated in an LFI.

Table 5: Comparison of optical properties of fluorescent NP. CP loading doses were 4% (Si-NP) and 83% (Pdots). *Values represent the mean \pm standard deviation of $n=3$ Si-NP and Pdot batches. CP concentration for QY measurement was 1 $\mu\text{g/mL}$ (PDOF-NP) and 4 $\mu\text{g/mL}$ (CN-PPV-NP).

	Si-NP		Pdots			PS-NP
	PDOF	CN-PPV	PDOF	CN-PPV	PDOF-CN-PPV	
λ_{Ex} [nm]	378	465	380	454	380	366
λ_{Em} [nm]	438	628	437	627	627	406
ϕ [%]	31.3 \pm 5.0*	13.7 \pm 2.6*	38.0 \pm 7.2*	9.5 \pm 0.9*	>9.9**	64.8

*mean and standard deviation of 3 individual batches **emission ≥ 750 nm was not included in the calculation due to appearance of a scattering peak

A high fluorescence brightness is desired for signal transducer NP. According to **Equation 7**, the NP brightness increases with the product of QY and loading dose. The QY is expected to decrease with increasing loading dose due to the inner filter effect and has to be determined in relation to loading dose to find the optimum CP loading. For the range of CP loading dose tested, the QY was found to decrease with increasing loading dose for both PDOF and CN-PPV in Si-NP, as well as Pdots. (**Figure 24a and 24b**) The brightness, however, increased with loading dose for all samples. (**Figure 24c and 24d**) Therefore, a CP loading dose of 4% (Si-NP) and 83% (Pdots) was expected to result in the brightest NP and was taken forward for further experiments. For the optimum loading dose, Pdots showed a much higher brightness compared to Si-NP.

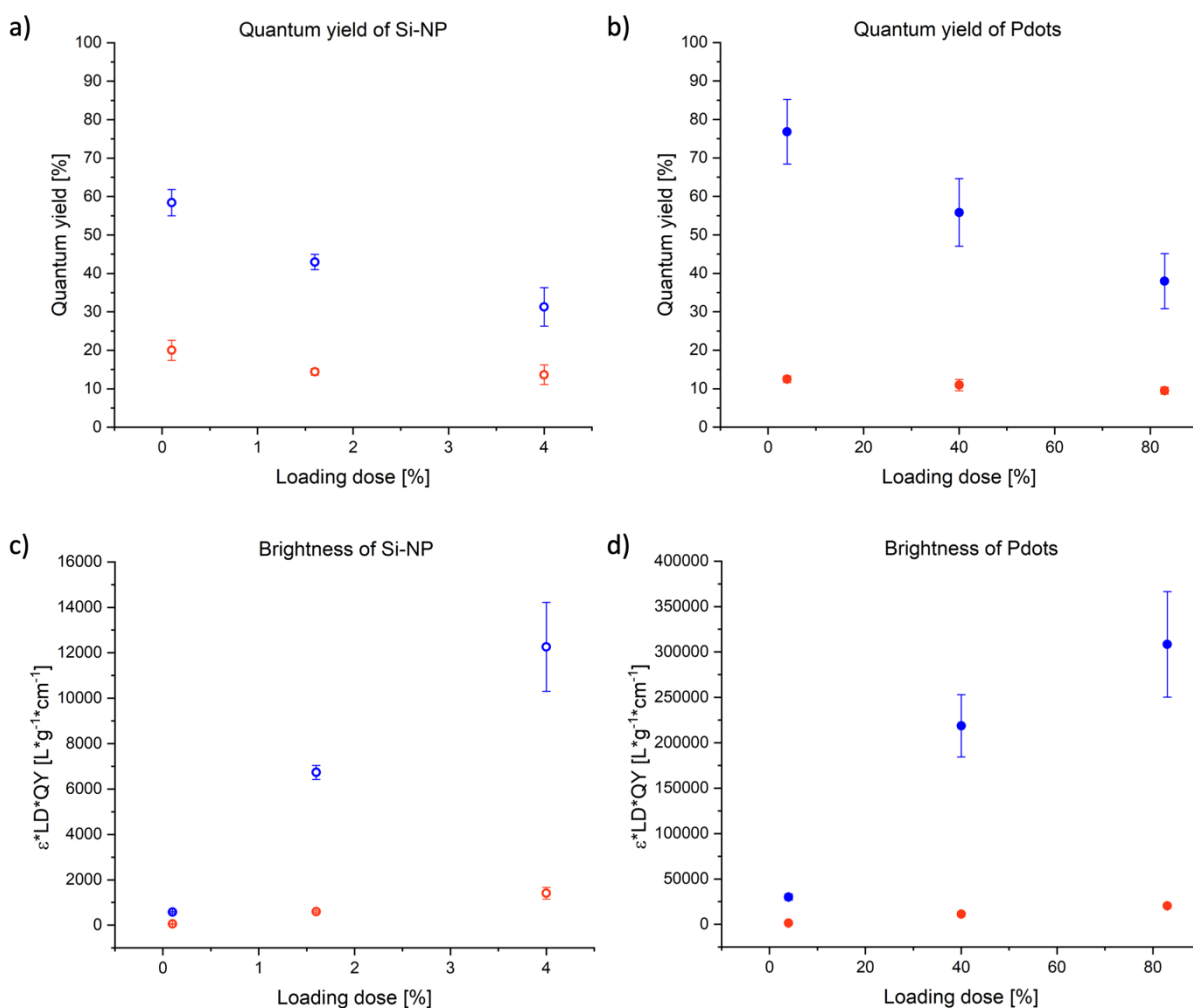


Figure 24: QY (a and b) and brightness (c and d) of Si-NP (a and c) and Pdots (b and d) depending on CP loading dose of PDOF (blue) or CN-PPV (red). Values represent the mean \pm standard deviation of $n=3$ batches.

2.3.6 Optimisation of antibody conjugation conditions with CN-PPV-Pdots

The net charge of NP and Ab for given isoelectric points of NP surface moieties and IgG depends on the buffer pH. During conjugation to a NP, the Ab has to overcome static repulsion to get close enough for covalent bond formation. Thus, the buffer pH influences the conjugation efficiency. Moreover, through the law of mass action, the degree of conjugation is affected by the amount of Ab. It has been shown, that the pH and IgG amount also determine the orientation, hence accessibility of NP-conjugated Ab.⁸⁷

The accessibility of the Ab, in turn, is important for the immunobinding of NP in LFI. Therefore, IgG conjugated NP were prepared under different conjugation conditions and the conjugates were examined for SBR in a simple dipstick LFI. CN-PPV-Pdots were used as representative NP, as the carboxylic groups on the surface of Si-NP and PS-NP were expected to behave alike in the Ab conjugation reaction. The highest SBR was achieved with conjugation at pH=7.4 and an Ab amount corresponding to a theoretical NP surface coverage of 75%. (**Figure 25**) However, as trade between consumption of the rather expensive Ab and SBR, an IgG amount corresponding to 50% theoretical NP surface coverage and buffer pH of 7.4 was chosen for further conjugation reactions.

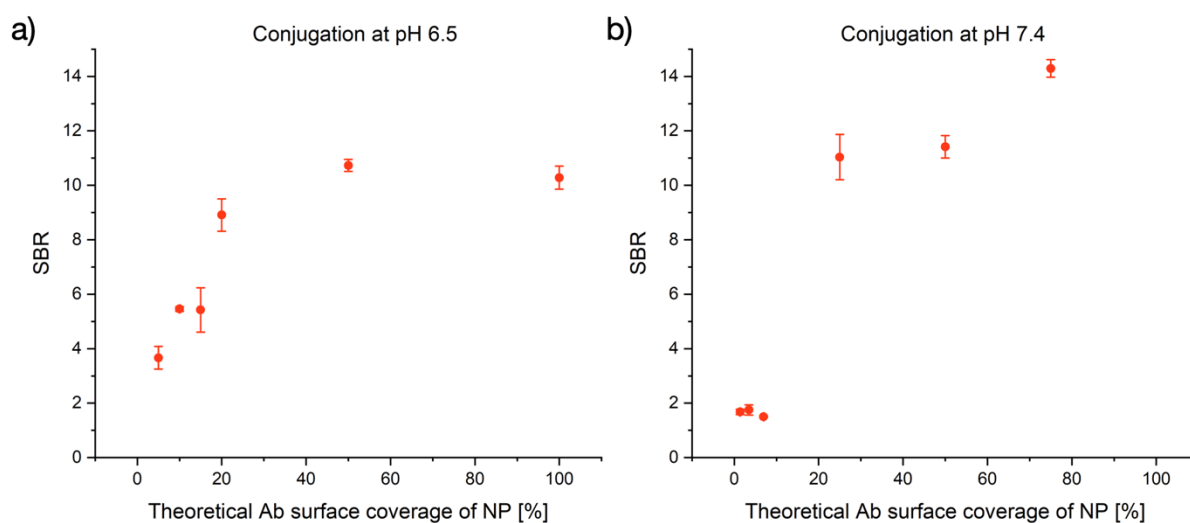


Figure 25: Dipstick LFI signal performance of CN-PPV-Pdots conjugated at pH=6.5 (a) or pH=7.4 (b). SBR versus IgG amount used for conjugation expressed as percentage of NP surface, that would be covered by the Ab in case of complete reaction. Values are mean and standard deviation of 3 individual test strips.

2.3.7 Assessment of antibody conjugation (IgG) using FLISA: Si-NP, Pdots, PS-NP and Au-NP

Preliminary evaluation of the brightness of the conjugated NP is desirably performed without the numerous influences on particle flow, that are expected in an LFI. Fluorescent NP have already been shown to be directly detectable in an ELISA-like fluorescent-linked immunosorbent assay (FLISA).¹¹⁵ Therefore, rabbit IgG conjugates of Si-NP and Pdots were tested in a FLISA system and compared to the commercial fluorescent PS-NP and colorimetric Au-NP. (**Figure 26**) All NP conjugates showed SBR values higher than 1 over the entire NP concentration range tested. Furthermore, an increase of SBR with NP amount was observed, indicating the presence of rabbit IgG on the NP surfaces.

For PDOF- and CN-PPV-Si-NP, PDOF-CN-PPV-Pdots and PS-NP, a linear increase was observed between 12 and 300 ng NP per well, while the linear range was between 0 and 5000 ng for Au-NP, far beyond the measured mass of fluorescent NP. The extended range of linearity to higher NP masses was most likely caused by the approximately 20-fold mass of one Au-NP compared to one of the other NP due to higher density of gold. PDOF- and CN-PPV-Pdots showed a substantially higher SBR compared to Si-NP, PS-NP and Au-NP with a linear range between 12 and 200 ng and slightly decreased SBR for 300 ng. The highest SBR was observed for PDOF-CN-PPV-Pdots.

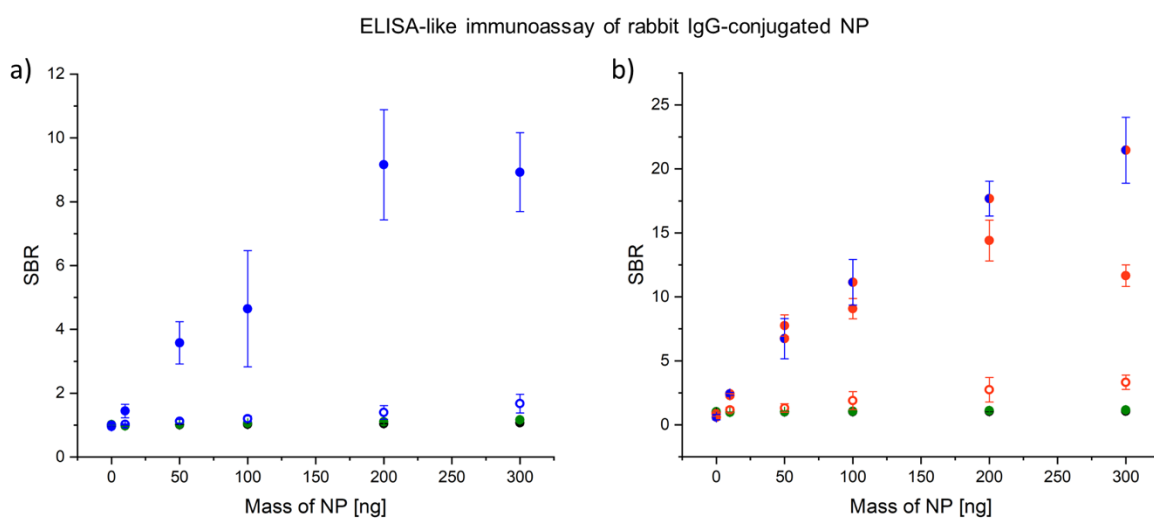


Figure 26: Performance of NP-IgG-conjugates in a FLISA system. Signal-to-background ratio (SBR) of wells coated with capture Ab to wells coated only with BSA. Fluorescent readout of PDOF-Si-NP (blue open circle) and PDOF-Pdots (blue) (both $\lambda_{Ex}/\lambda_{Em}=378/437$ nm) compared to PS-NP (green; $\lambda_{Ex}/\lambda_{Em}=365/406$ nm) and Au-NP (black; $\lambda=534$ nm) (a). CN-PPV-Si-NP (red open circle), CN-PPV-Pdots (red) (both $\lambda_{Ex}/\lambda_{Em}=454/650$ nm) and PDOF-CN-PPV-Pdots (red-blue) ($\lambda_{Ex}/\lambda_{Em}=378/650$ nm) compared to PS-NP (green) Au-NP (black) ($\lambda_{Abs}=534$ nm) (b). Values are mean and standard deviation of means of 3 plates à 3 wells.

2.4 Conclusion

The CP PDOF and CN-PPV were shown to have suitable optical properties for use in signal transducers, e.g. high extinction coefficients of $97.9 \text{ L}\cdot\text{g}^{-1}\cdot\text{cm}^{-1}$ and $25.8 \text{ L}\cdot\text{g}^{-1}\cdot\text{cm}^{-1}$ and high QY in THF solution of 98.6% and 17.7%, respectively. The CP could be encapsulated as Si-NP and Pdots with loading doses up to 4% and 83%, respectively. In these densely packed environments, the fluorophores showed a decreased QY of 31.3% and 38.0% for PDOF-Si-NP and PDOF-Pdots and 13.7% and 9.5% for CN-PPV-Si-NP and CN-PPV-Pdots, respectively.

However, as the number of encapsulated fluorophore molecules was high, the NP brightness was increased for NP with a high CP loading dose compared to NP with lower loading dose and the highest possible loading dose was used for further experiments for each NP system. The Si-NP and Pdots exhibited an appropriate size for LFI with a mean hydrodynamic diameter of 42.2 ± 13.0 and 35.9 ± 5.4 nm, respectively, independent of loading dose or type of CP encapsulated. The Si-NP surface was decorated with carboxylic group functionalised Pluronic® F127 for functionalisation, as indicated by a different zeta potential compared to Si-NP without carboxylic groups with values of -4.1 ± 0.4 mV and -2.5 ± 0.3 mV, respectively. Pdots had even more dense negatively charged surfaces with zeta potentials of -9.0 ± 2.5 mV, indicating the presence of carboxylic groups. The NP were successfully conjugated to rabbit IgG as evidenced by their outstanding performance in an ELISA-like FLISA system, especially in comparison to the two references PS-NP and Au-NP. It can be concluded, that both the optimised Si-NP and Pdots can be potentially used as signal transducers in LFI.

Chapter 3

CP-based fluorescent nanoparticles
as signal transducers in LFI:

Preliminary investigations with the model proteins
rabbit IgG and goat anti-rabbit IgG

3.1 Introduction

3.1.1 LFI structure and critical parameters

As stated previously in Chapter 2, the sensor undergoes many interactions, not only with the analyte, but also medium and each component of the LFI membrane. The LFI itself consists of an overlapping sample pad, conjugate pad, lateral flow membrane (typically NC) and absorbent pad (**Figure 1**). Performance criteria for fluorescent signal transducers in an LFI assay can therefore be categorised according to the following list:

- Long shelf-life
- Low toxicity or environmental impact
- Dispersibility in sample matrix or running buffer
- Inertness to sample matrix
- Fast, selective and strong binding to analyte
- Weak interaction with LFI membrane
- Unhindered flow through membrane pores
- Fast and strong binding to capture antibody
- High signal intensity
- Large Stokes shift
- Low signal decay

3.1.1.1 Choice of membrane

All of the strip components of an LFI are commercially available with different characteristics. In a typical optimisation approach, the NC membrane is evaluated first for non-specific binding.¹¹⁶ Blocking of the membrane, e.g. with glycerol or BSA, is also common to reduce non-specific binding.⁴³ Additionally, the relative flow speed of analyte and detection NP has to be optimised by choice of the membrane to increase sensitivity.¹¹⁷ In a fluorescent LFI for detection of the protein Cry1Ab, only one of five different membranes tested showed no signal for the negative control. The false positive results were attributed to clogging of membrane pores.¹¹⁸ Furthermore, an examination of five NC membranes from varying manufacturers showed different wavelengths and lifetimes of auto-fluorescence for each of the membranes.¹¹⁹

Therefore, the right choice of membrane might reduce background signal, depending on the fluorescence spectrum of the reporter dye and the physicochemical properties of the NP.

3.1.1.2. LFI geometry

Apart from the strip materials, the geometry of the assay is important for sensitivity. In a study on the size of sample and conjugation pad, the LOD for the detection of human IgG with colloidal gold decreased, if the sample and absorption pad area increased two-fold, because of the higher amount of analyte available. If the sample and absorption pad area was increased three-fold, the LOD increased, because of the higher flow velocity, hence reduced contact time of analyte and capture antibody. In general, if the conjugation pad size increased in the same manner as the sample and absorption pad, the LOD did decrease with an increase of size.¹²⁰ In a study on detection of chorionic gonadotropin with colloidal gold, the NC membrane shape was varied to become more narrow or wider towards the absorbent pad as a trapezoid. When the width was narrowed from 12 to 4 mm, the lowest detectable amount was cut to half (5 IU/L chorionic gonadotropin), compared to a straight design (10 IU/L). The same study revealed, that a test line distance of 12.5 mm from the conjugate pad resulted in a higher test line intensity compared to lower or higher distances, independent of membrane shape.¹²¹ This finding was confirmed in another study on the influence of the test line position on LFI sensitivity with colloidal gold. The lowest detectable amount for test line positions of 7.5 and 12.5 mm from the conjugate pad was half as much (10 IU/L of chorionic gonadotropin) compared to test line position of 2.5 and 17.5 mm from the conjugate pad (20 IU/L).¹²² If spots of capture antibody are used instead of a continuous line, the arrangement of the spots greatly influences the uniformity of NP flow. In a quantitative colloidal gold assay for cartilage oligomeric matrix protein, many capture antibody spots were cast on the membrane in successive lines to avoid the hook-effect. When the spots were arranged straight after each another, the lines of spots developed inconsistently in colour. If the spots were arranged in a zig-zag manner, the line intensity decreased gradually towards the absorbent pad, but was consistent within the lines.¹²³

3.1.2 Performance of fluorescent LFI in the literature

Colloidal gold-based colorimetric LFI are generally end-user-friendly, as no instruments are necessary for a qualitative readout. Therefore, the development of fluorescent labels for point-of-care assays has to be justified by improved limits of detection compared to established systems. A number of comparisons of fluorescent LFI to colorimetric gold-based assays have been published to date.

For example, CdTe QD-loaded silica NP were used to detect α -fetoprotein in buffer solution at a concentration 10-times lower (2.0 ng/mL) than with colloidal gold (20.0 ng/mL).¹²⁴ An even more dramatic increase in sensitivity was published for fluorescent Eu(III)-doped particles, that could detect as little as 0.03 ng/mL of the model analyte biotin-BSA.¹²⁵ The sensitivity was further decreased to 0.02 ng/mL, when time-resolved fluorescence detection was used to lower background intensity. Using colloidal gold as signal transducer, the lowest detectable amount of biotin-BSA was 6.1 ng/mL, more than 300 times higher than with fluorescence sensing.

Apart from pilot studies with model analytes, fluorescent labels have been published to work with more complex antigens. For the detection of *E. Coli* O157:H7 in PBS it was shown, that $1.6 \cdot 10^3$ CFU/mL could be detected using fluorescent microspheres, remarkably lower than $1.25 \cdot 10^4$ CFU/mL using gold NP.¹²⁶ When milk was used as a sample matrix, the lowest detectable amount of bacteria increased, but was still lower for the fluorescent, compared to the colorimetric assay (10^4 and 10^5 CFU/mL, respectively). For the detection of aflatoxin T-2 the impact of the sample matrix was even higher. While the cut-off value for detection in PBS was low for fluorescent dye-doped polystyrene microspheres compared to colloidal gold (10 ng/mL and 40 ng/mL, respectively), no analyte could be detected at all in spiked fresh milk samples with fluorescent signal transducer, but the gold NP-based LFI could still detect 50 ng/mL of the aflatoxin.¹²⁷ For the detection of casein in milk samples with fluorescent microparticles, the matrix effects was postulated to be eliminated by diluting the sample 10,000-fold with PBS prior to measurement.¹²⁸ In PBS, the LOD of the fluorescent LFI (100 ng/mL) was 8-times lower than for colloidal gold (818 ng/mL). In diluted milk samples spiked with casein, the analyte concentration determined by the fluorescent LFI was close to the added casein amount, but false positives were observed in non-spiked samples.¹²⁸

The problem of sample matrix background fluorescence can also be circumvented by adjustment of the fluorophore emission wavelength. For example, when the veterinary drug 5-hydroxyflunixin was detected in milk samples using the near-infrared dye IRDye[®] 800CW, the LOD was 10-times lower for the fluorescent LFI (0.07 ng/mL) compared to gold NP (0.82 ng/mL).¹²⁹ However, fluorescent labels are not always necessarily superior to colorimetric labels in terms of sensitivity. In a study on the detection of the insecticide, imidacloprid, the LOD was found to be 0.02 ng/mL for time-resolved measurement of fluorescent NP, but only 0.01 ng/mL for the colloidal gold LFI.¹³⁰ Still, both LFI showed the same sensitivity compared to ELISA. Given the varying performance of fluorescent LFI compared to gold-based colorimetric ones, it is questionable if the sensitivity of the assay is more influenced by the assay optimisation, than by the nature of the signal transducer.

A study on the detection of influenza A and B viruses compared the performance of a commercial fluorescence-based LFI (Sofia[®]) to two commercial gold-based LFI (Quickvue[®] and Directigen[™]). In this case, Sofia[®] was able to detect higher dilutions of influenza A/B viruses (1:3000/1:800) than Quickvue[®] (1:100/1:75) and Directigen[™] (1:100/1:25).¹³¹

To conclude, many publications indicate that fluorescent signal transducers can potentially increase sensitivity of LFI. Nevertheless, the performance of the assay depends on the antigen and sample matrix and has to be compared with optimised established standards, like colloidal gold, in realistic environments to prove superior analysis.

3.1.3 Detection and quantification methods

Fluorescent LFI signals are detected either visually or by instrumentation. In all cases, a light source is necessary for excitation of the fluorophores. For instrumental detection of the signal the light source is usually integrated into the detection device, while for visual interpretation of the signal it might be integrated in the test strip. For example, a fluorescent LFI with an integrated organic LED was developed for the detection of donkey IgG (model analyte) using QD signal transducers. The LOD for visual detection with QD (3 nM) was 7-fold lower than the colorimetric readout with colloidal gold (21 nM).¹³² When comparing the LOD for visual versus instrumental fluorescence detection, instrumental LOD are generally more sensitive, as was shown for the detection of clenbuterol in swine urine with fluorescent dye doped silica NP. The LOD by visual inspection was 0.1 ng/mL clenbuterol, but 0.037 ng/mL using the ESEQuant fluorescent lateral flow strip reader.¹³³

An electronic detection device is also necessary if a quantitative readout is desired. A number of fluorescence readers designed for use with LFI are available from different manufacturers and various applications have been published.^{126,134–136} Some readers feature multiple detection modes, such as different excitation and emission wavelengths or colorimetric readout along with fluorescence detection.¹³⁷ Strip readers for time-resolved fluorescence measurement are often custom-made, but commercial readers are also available.^{138–141} The LFI signal can be also quantified by equipment developed for different applications. This could help to promote acceptance of fluorescent LFI by reduction in cost, if existent equipment can be used in analytical labs. For example, a Western Blot imager was used to quantify four different antibiotics with a near-infrared dye-based fluorescent LFI.¹⁴² To make quantitative fluorescent LFI available to end-users or in less developed environments, the need of expensive analytical tools must be eliminated.

Many publications focus on the integration of smartphone cameras for quantitative signal detection.^{92,143–145} The possibility of multiplex detection with smartphone-based fluorescent LFI was proven by the example of simultaneous detection of mercury ions, ochratoxin A and salmonella on one test strip.¹⁴⁶ For the quantification of chorionic gonadotropin next to carcinoembryonic antigen, the integrated LED of a smartphone together with an external UV LED was used to enable dual-modality colorimetric and fluorescent quantification with a smartphone camera.¹⁴⁷ The need of an external power source was eliminated in a fluorescent QD LFI for detection of the rotavirus. The disposable printed electronics excitation LED was powered through the contactless near-field communication module of a smartphone. A separate CCD camera was used for signal quantification, but it was stated that the smartphone camera could be used for detection, as well.¹⁴⁸ A set of optical filters is usually used for fluorescence sensing to exclude excitation light from the detector. In a smartphone-based fluorescent assay for detection of influenza A nucleoprotein the signal could be quantified without optical filters because of the large Stokes-shift of the QD reporters. The LOD with two different phones (1.5 and 2.6 fmol of influenza A nucleoprotein) was comparable to the LOD with quantification by a gel imager (1.9 fmol).¹⁴⁹

A problem with smartphone-based signal detection is the different quality of smartphone cameras. To make fluorescent LFI end-user friendly, modern commercial LFI include test strip, optoelectronics, power source and smartphone-interface in one housing. For example, the first over-the-counter COVID-19-LFI for home use that got an emergency authorisation of use by the FDA, is a fluorescent LFI that features a test strip, optoelectronics, a power source and a Bluetooth®-interface in one housing.¹⁵⁰ The manufacturer claims, that the QD-based test shows a sensitivity as high as 95%.¹⁵¹

3.1.4 Advantages/disadvantages of fluorescent LFI

To summarise, fluorescent LFI may show decreased LOD compared to colorimetric LFI, but in general, need equipment to be read. In particular, an excitation light source is mandatory. Both colorimetric and fluorescent LFI are suitable for qualitative and quantitative readouts. For a quantitative readout, a detection device is needed. Usually, but not always, optical filters have to be used to exclude excitation light from the detector in fluorescent LFI, adding further complexity to the instrumentation. While colourful samples could interfere with interpretation of a colorimetric assay, the sample matrix auto-fluorescence may reduce sensitivity of fluorescent LFI. In that case, proper sample preparation or appropriate choice of fluorescent reporter emission wavelength have to be used.

3.1.5 Target specifications of LFI, study questions and hypotheses

As the focus of investigation was on the sensitivity-enhancement induced by the use of conjugated polymers as fluorescent signal transducers, the absolute sensitivity of the assay was of minor interest. Most importantly, the strip design should allow comparison of fluorescent and colorimetric nanoprobe. To ensure comparability, the NP release and flow characteristics should be optimised for each NP system through an optimised composition of the running buffer, i.e., type and concentration of surfactants. The dimensions, geometry and architecture of the assay should be kept simple and uniform to reduce sources of variation and minimize effort. Literature data suggests that a rectangular strip design and a strip width of 4-5 mm is suitable. The test line is best to be placed between 10 and 12.5 mm from the conjugate pad and should be kept constant in between tests.

The parameters that may be varied/optimised in LFI systems include:

Parameter	Objectives of optimisation studies
NP conjugate chemistry	Surface density and orientation of antibody coverage impacts on NP binding to the antigen
NP conjugate suspension concentration	The NP concentration must be high enough to overcome losses due to retention in the sample pad, possible non-specific binding to the membrane and sufficient binding to test and control lines
Sample and conjugate pad pre-treatment	Optimisation of additives to the sample and conjugate pad will maximise the percentage release of NP from the sample pad onto the test strip
Running buffer composition	Optimisation of running buffer composition ensures rapid flow of the NP through the membrane and reduces non-specific NP binding to the membrane, which leads to increased background signal.
Test and control line capture antibody	The concentration of the test and control line antibody is directly proportional to signal intensity and SBR ratio. It must be optimised together with the NP conjugate suspension concentration to achieve the highest SBR ratio at the lowest analyte concentration.

It was hypothesised, that the test line signal intensity is dependent upon all these parameters and that a comparison between LFI with different signal transducers was only valid for optimised values of each.

3.2 Materials and methods

3.2.1 Materials

NC membranes Immunopore RP and FF80HP, sample and absorption pad CF6 and conjugate pad Fusion 5 were from GE Healthcare LifeSciences, UK. Adhesive plastic backings were from DCN Dx, USA. Anti-hFABP (#4F29 10E1 and #4f29 9F3) and hFABP (#8F65) were from HyTest, Finland. Tetracycline antibody from sheep (#FGI-20-1176) and tetracycline-BTG (#FGI-80-1296) were from Biozol, Germany. Anti-sheep IgG (SAB3700698), anti-mouse IgG (M6898), Staphylococcal enterotoxin A (#S9399) and tetracycline (#T3258) were from SigmaAldrich, Germany. Anti-Staphylococcal enterotoxin A antibodies (#C86107M and #C86104M) were from Meridian Life Science, USA.

3.2.2 General LFI parameters: IgG

Dipstick LFI were prepared with an adsorption pad overlapping 8 mm with a 25 mm long NC membrane mounted on an adhesive plastic backing. The strips were 4-5 mm wide. A test line of anti-rabbit IgG (500 µg/mL, 1 mm wide) was drawn 13 mm from the membrane bottom with a fountain pen and dried for 15 min at room temperature.

Fluorescent signals were detected with a QIAGEN LFReader. The reader was equipped with two LEDs with adjustable power for excitation, LED1 ($\lambda_{Ex}=365$ nm) and LED2 ($\lambda_{Ex}=470$ nm), as well as two optical filters for detection ($\lambda_{Em}=430$ nm and $\lambda_{Em}=680$ nm). The wavelength sets used for detection were $\lambda_{Ex}/\lambda_{Em}=365/430$ nm (PDOF-NP and PS-NP), $365/680$ nm (PDOF-CN-PPV-NP) and $470/680$ nm (CN-PPV-NP).

The signal of colorimetric Au-NP LFI was detected with an iPhone XR camera at a distance of 15 cm and illumination by the in-built LED. The pictures were analysed with ImageJ software and the inverse greyscale intensity was used as intensity value. When the mobile phone camera was used for analysis of fluorescent LFI, the excitation light source was a UVP mini UV viewing cabinet C-15G with $\lambda_{Ex}=365$ nm and the greyscale intensity was used as intensity value.

3.2.3 Comparison of NC membranes

NC membranes Immunopore RP and FF80HP were cut in pieces of 1x2 cm and the fluorescence intensity was read with a QIAGEN LFReader. The intensity was averaged over 1 cm in the middle of the membrane.

For determination of autofluorescence in the wet state the membranes were wicked with water prior to measurement. In both cases, the fluorescence intensity was measured with an LED1/2 power of 160.

3.2.4 Effects of running buffer composition

Rabbit IgG-conjugated CN-PPV-Pdots were diluted in PBS to a concentration of 2.4 µg/mL. Solutions of Tween 20, Triton X-100 or a mixture of BSA, Triton X-100 and PEG400 were prepared in PBS at concentrations of 0.2, 0.4, 0.5, 0.6, 0.8, 1, 1.25, 1.5, 1.75, 2, 4, 6, 8 and 10 µg/mL. In the mixture of BSA, Triton X-100 and PEG400 each constituent had the given concentrations. Dipstick LFI were dipped in a mixture of 10 µL of the NP suspension and 50 µL of the surfactant solution for 5 min. The strips were successively dried at room temperature under reduced pressure and the fluorescence intensity read with a QIAGEN LFReader with an excitation LED power of 44. The SBR was calculated as signal intensity divided by the intensity 4 mm below the test line.

The procedure was similar for Si-NP, PS-NP and Au-NP, except for the following changes:

Surfactant concentrations were 0.5, 1, 1.5, 2 and 2.5 µg/mL. CN-PPV-Si-NP were diluted and measured at the same concentrations and wavelengths as the Pdots, but with an excitation LED power of 224. PS-NP were diluted to a concentration of 48 µg/mL and the fluorescence intensity was read with an excitation LED power of 64. Au-NP were diluted to a concentration of 24 µg/mL and images of the strips were captured with an iPhone XR. The images were analysed with ImageJ software and the intensity read from the greyscale value.

3.2.5 NP redispersion from conjugate pad

Additive solutions (62.5, 50, 37.5, 25, 12.5 and 0 mg/mL) were prepared by mixing Triton X-100, BSA, PEG400, glycerol and sucrose (12.5, 10, 7.5, 5, 2.5 and 0 mg/mL each) in water. IgG-PDOF-Pdots (10 µL, 2 µg/mL) were mixed with 40 µL of the additive solution. The conjugate pads (10x10 mm) were immersed in the conjugate mixture for 5 min and dried in vacuum. The LFI strips were composed of sample pad (25 mm), conjugate pad (10 mm), NC membrane (25 mm) and wicking pad (25 mm). A test line of anti-rabbit IgG (0.5 mg/mL) was drawn 13 mm from the NC membrane bottom. The strips were assembled on an adhesive plastic backing, cut in pieces of 5 mm width and run by adding 200 µL PBS buffer. After 10 min the strips were dried in vacuum and the fluorescence intensity was read with a QIAGEN LFReader.

In a second set of experiments, the sample pads were immersed in a solution of 1% Triton X-100, 1% BSA and 1% PEG400 in water (200 μ L/125 mm² pad) and dried in vacuum before strip assembly.

In a third set of experiments, PDOF-Si-NP were used instead of Pdots and the sample pad was used without pre-treatment. Additive solutions were composed of 62.5, 31.3, 15.6 and 0 mg/mL Tween 20 in water.

3.2.6 Dipstick assay with rabbit IgG

IgG-PDOF-Pdots, IgG-CN-PPV-Pdots or IgG-PDOF-CN-PPV-Pdots were diluted to NP concentrations of 0.2, 0.4, 0.6, 0.8, 1, 1.2, 1.6 and 2 μ g/mL with HEPES (20 mM, pH=7.4) containing 1% PEG400. For IgG-PDOF-Si-NP, IgG-CN-PPV-Si-NP, IgG-PS-NP and IgG-Au-NP the concentrations were 2.5, 5, 12.5, 25, 37.5, 50, 75 and 100 μ g/mL. 10 μ L of the suspension were mixed with 50 μ L of a solution of 1% Triton X-100, 1% BSA and 1% PEG400 in 8 mM PBS. 5 mm-wide LFI strips were dipped in the suspensions for 5 min. The strips were dried in vacuum and the fluorescence intensity was read using the QIAGEN LFIReader (Pdots, Si-NP and PS-NP) or with a mobile phone camera (Au-NP). The excitation LED power was 64 (PDOF and PDOF-CN-PPV-Pdots), 44 (CN-PPV-Pdots) or 160 (PDOF- and CN-PPV-Si-NP and PS-NP).

3.2.7 Conjugation of anti-tetracycline-, anti-SAE- and anti-hFABP IgG to CN-PPV-Pdots and Au-NP and assessment of NP

The conjugation procedure was the same as for rabbit IgG (Chapter 2.2.6). The Ab clones used were FGI-20-1176 (tetracycline), C86104M (SAE) and 4F29 10E1 (hFABP).

The dipstick LFI strips were assembled following the general dipstick LFI composition. A test line of primary Ab (0.5 mg/mL) and secondary Ab (0.5 mg/mL) was drawn on the NC membrane 8 and 13 mm from the bottom, respectively. Primary Ab were C86107M (SAE) and 4F29 9F3 (hFABP). For the competitive tetracycline assay, tetracycline-BTG (FGI-80-1296, diluted 1:20 in PBS) was used instead of primary Ab. Secondary antibodies were anti-sheep IgG (tetracycline) and anti-mouse IgG (SAE and hFABP).

The procedure of the ELISA was the same as with rabbit IgG-conjugated NP. (Chapter 2.2.8) The Ab and antigen used for coating of the plate were the same as for the test line of the dipstick assay.

3.3 Results and discussion

The optimisation of an LFI is usually performed in the direction of increasing complexity. First, the antibody-antigen pairs are checked for sufficient specificity, selectivity and binding strength in an ELISA.¹⁵² Then, the NP flow through and non-specific binding to the membrane is optimised by selection of an appropriate membrane and/or addition of surfactants. The membrane is then checked for sufficient adsorption capacity of the antibodies. These investigations are usually done in a dipstick format, to reduce the number of influencing parameters. Afterwards, the conjugation pad is added to the dipstick and different pad materials, dimensions, NP amounts and surfactants tested for optimised NP redispersion. The sample pad is then added to the test strip, where the dimension, pad material and surfactant pre-treatment are essayed for optimised wicking, surfactant release and possibly selective retention of components of the sample matrix. Finally, the LFI is validated with samples of known antigen concentration and real patient samples.

3.3.1 Comparison of NC membranes

One main objective of this thesis was to compare different fluorescent probes with Au-NP. Therefore, the autofluorescence of the NC membrane had to be low at excitation and detection wavelength of the fluorescence reader device. The membranes Immunopore RP and FF80HP were used, because they were published to work with Au-NP or had low autofluorescence, respectively.^{91,119} When analysed with the QIAGEN LFReader, both membranes showed remarkably higher background fluorescence in wet, than in dry state. (**Table 6**)

Table 6: Fluorescence signal intensities of blank NC membranes at excitation and detection wavelengths of the QIAGEN LFReader. Values are averages over 1 cm of the membrane.

$\lambda_{Ex}/\lambda_{Em}$ [nm] (Fluorophore)	Mean background signal intensity [mV]			
	Dry		Wet	
	Immunopore RP	FF80HP	Immunopore RP	FF80HP
365/430 (PDOF/PS-NP)	251.7	384.1	1961.1	2357.2
365/680 (PDOF-CN-PPV)	83.6	76.1	116.0	130.4
470/680 (CN-PPV)	36.1	30.3	41.5	46.2

Therefore, membranes were dried prior to signal quantification in subsequent experiments. At the wavelength set used for detection of PDOF- or PS-NP the membrane Immunopore RP showed a lower autofluorescence compared to FF80HP. In contrast, at wavelengths used for detection of CN-PPV- and PDOF-CN-PPV-NP the background intensity was slightly lower for FF80HP than for Immunopore RP. However, as the difference at these two wavelength sets was much lower than for PDOF- and PS-NP wavelengths, Immunopore RP was chosen as NC membrane for all further experiments.

3.3.2 Test line concentration and detection

The test line is one of the two main sites of immunosorption of an LFI and, moreover, the signal detection region. Therefore, special attention has to be paid on the optimisation of capture antibody binding and detection method.

3.3.2.1 Test line concentration optimisation

The concentration of capture antibody at the test line is a major influence on signal intensity. Increasing antibody amounts usually promote binding of the NP probe through the law of mass action. However, the signal intensity may decrease for very high capture antibody concentrations.¹⁵³ For determination of the optimum test line concentration, PDOF-Si-NP and Au-NP were used as signal transducers to investigate the interaction of both covalently and absorptive bound rabbit IgG on the NP surface with the anti-rabbit capture antibody.

(Figure 27)

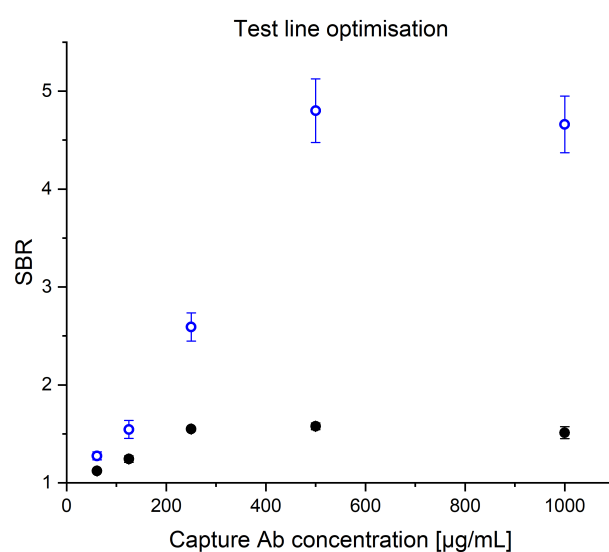


Figure 27: SBR of PDOF-Si-NP and Au-NP dipstick LFI versus concentration of capture antibody at test line. Data points are mean values and standard deviations of 3 individual strips.

Si-NP showed a linear increase of SBR with test line concentration in the range of 61-500 µg/mL of capture antibody and a slightly reduced SBR at 1000 µg/mL. Au-NP only showed a linear increase in SBR over the range of 61-250 µg/mL. However, the SBR was constant for higher antibody concentrations. As no decrease in signal intensity was observed for higher test line concentrations with Au-NP, the plateauing was believed to result from the limited amount of NP available, rather than excessive capture antibody amounts. Thus, a test line concentration of 500 µg/mL was used for successive experiments.

3.3.2.3 Test line detection: Mobile phone and ImageJ versus LFReader

The signal quantification of fluorescent LFI requires instrumentation and the detection instrument influences the sensitivity of the assay. However, sophisticated detection devices are expensive, thus less likely acquired. If the gain in sensitivity by use of specialised equipment is negligible, cheap instruments might be favoured. To assess the sensitivity of fluorescent LFI depending on the detection device, two very different setups were used:

- 1) The UVP mini UV viewing cabinet C-15G, designed for inspection of liquid chromatography strips as excitation light source with integrated UV-filtering viewing window, a mobile phone camera as detection device and evaluation of the data using freeware ImageJ software
- 2) The QIAGEN LFReader lateral flow strip reader, specifically designed to match the excitation and emission wavelengths of the examined fluorophores and evaluation of the data with the associated LFStudio software

Both systems were tested with different amounts of PDOF-, CN-PPV- and PDOF-CN-PPV-Pdots each. In general, the SBR using the mobile phone camera was more than 10-times lower, compared to the LFReader. (**Figure 28**) However, an increase in SBR was observed over the whole range of NP mass tested, even with mobile phone detection. One major drawback of the simple setup was the fixed excitation wavelength, optimised for PDOF excitation. Thus, when compared to the LFReader, the SBR of CN-PPV-Pdots were shifted to lower values relative to PDOF-Pdots. As the built-in filter of the UV chamber was a simple high-pass filter, the PDOF-CN-PPV-Pdots did not profit from background reduction through large Stokes-shift and showed no higher SBR, compared to PDOF-Pdots. For successive experiments, the LFReader was used for signal detection, to avoid limitation of the results to the boundaries of the instruments.

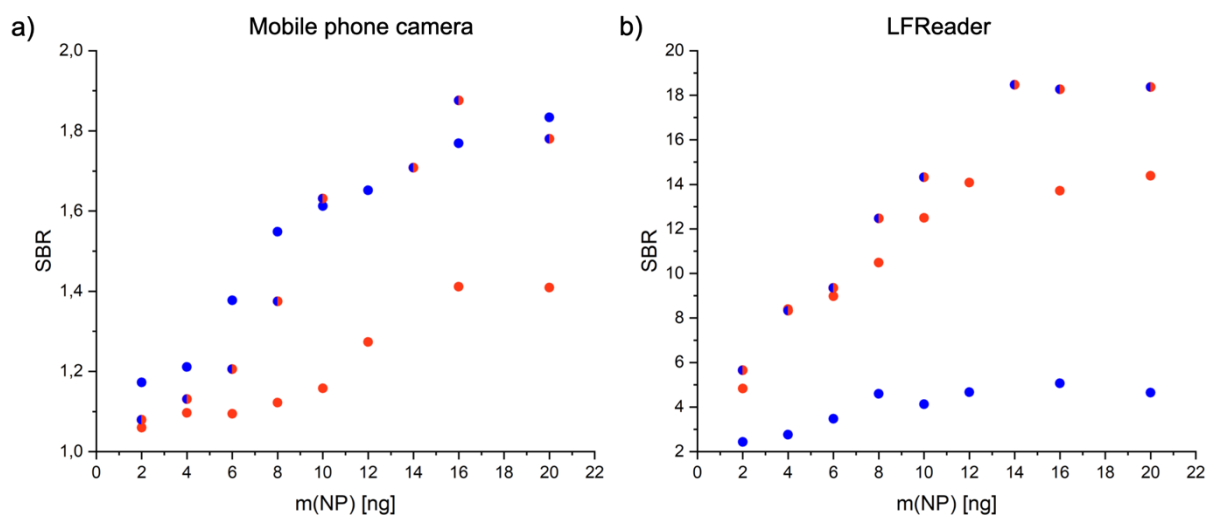


Figure 28: SBR of PDOF-, CN-PPV- and PDOF-CN-PPV-Pdots in a dipstick LFI with signal detected either by an iPhone XR under illumination in a UV-chamber and successive evaluation with ImageJ software (a) or by the LFReader and successive evaluation with LFStudio software (b).

3.3.3 Effect of running buffer composition

As the particle flow is highly influenced by the type of NP, the running buffer composition was assessed in a dipstick assay for Pdots, Si-NP, PS-NP and Au-NP independently. Two non-ionic surfactants, Tween 20 and Triton X-100, were chosen for the investigation, as both were reported to provide good signal development in Au-NP LFI.¹⁵⁴ Additionally, a 1:1:1-mixture of Triton X-100, PEG400 and BSA was tested, that was published to work well with Pdots.⁴¹ At first, Pdots were investigated in a wide surfactant concentration range from 0.2 to 10 $\mu\text{g/mL}$, to identify the concentration range that shows the highest changes in SBR. Both with Tween 20 and Triton X-100, no signal was observed for surfactant concentrations of less than 1 $\mu\text{g/mL}$. (**Figure 29**) The SBR increased between 0.8 and 2.5 $\mu\text{g/mL}$ and remained constant for higher surfactant concentrations. With the mixture of Triton X-100/PEG400/BSA the curve was shifted to lower concentrations with an increase of SBR between 0.4 and 0.8 $\mu\text{g/mL}$ each. The concentration range, in which the increase and plateau of SBR was observed for Pdots (0.5-2.5 mg/mL), was taken forward for investigations with Si-NP, PS-NP and Au-NP. For Si-NP, the maximum SBR was reached with at least 2 mg/mL Tween 20, or 1 mg/mL of either Triton X-100 or the mixture. With PS-NP, the amount of Tween 20 necessary to reach the SBR plateau was above the examined concentration range. In contrast, the minimum amount of Triton X-100 for maximised SBR was below the tested concentrations. The surfactant mixture led to plateauing SBR at 1 mg/mL. For Au-NP, each of the surfactant systems showed maximised SBR for concentrations of at least 1 mg/mL.

However, the SBR plateaus differed in absolute values between surfactants. The highest SBR for Pdots was observed using the surfactant mixture, while for Si-NP, PS-NP and Au-NP the highest SBR was found with Tween 20. To ensure a surfactant concentration in the SBR plateau range, a value higher than the threshold had to be chosen for the LFI. Thus, 8 mg/mL of Triton X-100/PEG400/BSA or 8 mg/mL of Tween 20 were used for the running buffer of Pdots or Si-NP, PS-NP and Au-NP, respectively, in later LFI experiments.

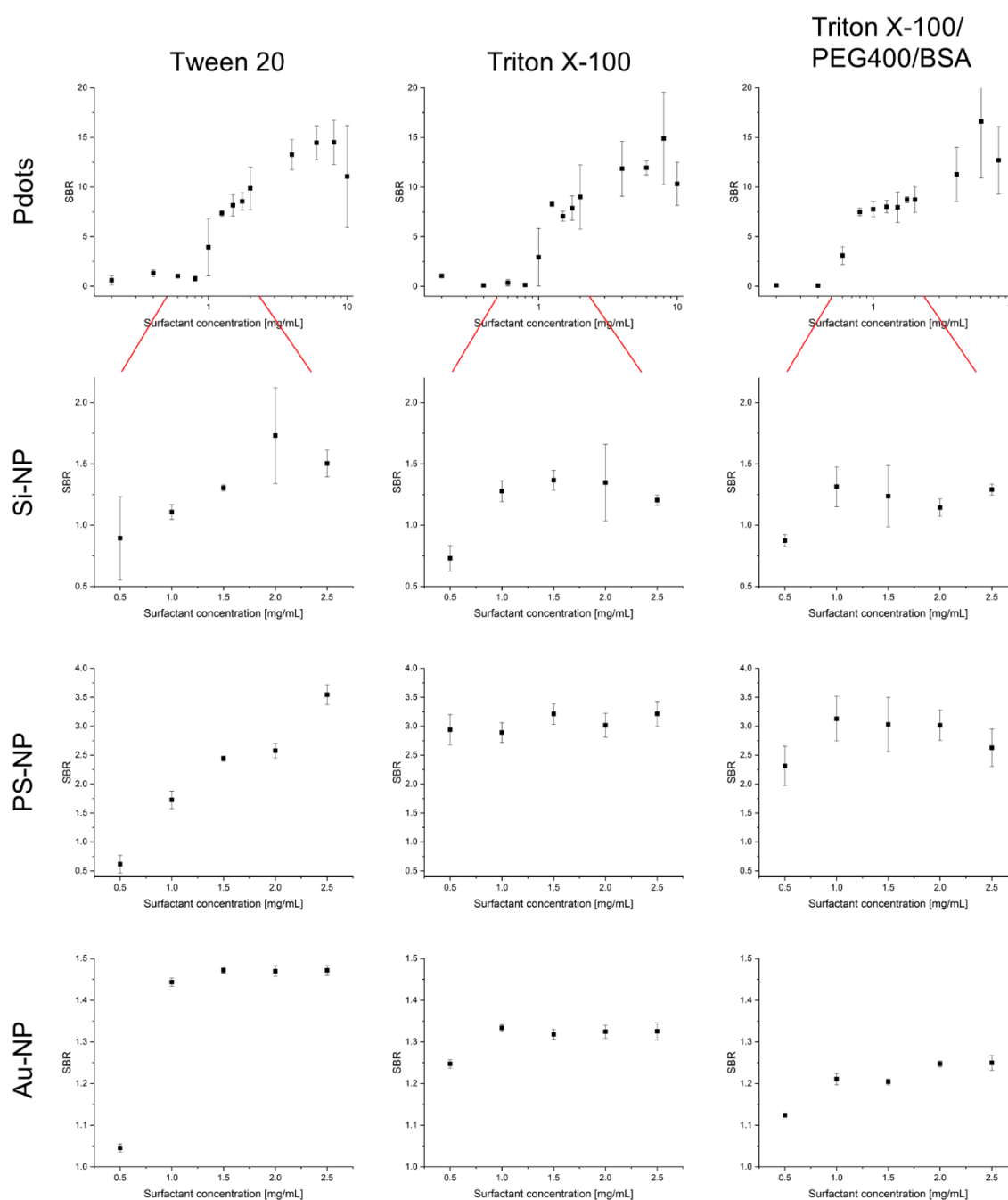


Figure 29: Signal-to-background ratio of dipstick LFI run with NP suspensions containing surfactants of different concentration. Values are mean and standard deviations of 3 individual strips.

3.3.4 NP redispersion from conjugate pad

In a real-life application of LFI the NP signal transducers are usually stored as dry particles in a conjugate pad. For preparation, a NP suspension is wicked in or sprayed on the conjugate pad and successively dried.¹⁵⁵ The amount of NP available for signal generation is determined by the amount redispersed from the conjugate pad. The degree of redispersion depends on the particle-particle, particle-conjugate pad and particle-running buffer interaction and is therefore varying with NP type. Thus, the redispersion was investigated for Pdots and Si-NP, independently. To lower the interaction of particle-particle and particle-conjugate pad, surfactants were used in different amounts in the NP conjugate suspensions.

3.3.4.1 Pdots

For Pdots, a surfactant mixture of Triton X-100, PEG400, BSA, glycerol and sucrose was chosen according to a published procedure.⁴¹ The components of the running buffer that were found to be optimal for particle flow (**Figure 29**), were already included in the conjugate mixture. However, as soon as the sample is applied to the LFI, the soluble components in the conjugate pad are quickly absorbed and move along the NC membrane more or less immediately. Thus, a gradient of surfactant concentration is created over time. If the components of the running buffer are stored dry in the sample pad of the LFI, they are, as well, immediately dissolved. However, since the sample pad is the buffer reservoir for the LFI, the concentration of running buffer components that elute from the sample pad is constant. In this case, the surfactants in the conjugate pad are still flushed off at once, creating a surfactant gradient over time, but one that does not deplete.

For this reason, the influence of pre-treatment of the sample pad was investigated. Without sample pad pre-treatment, a substantial increase in SBR was observed between 0 and 10 g/L surfactants in the conjugate buffer, indicating a more efficient redispersion of the NP when surfactants were present in the conjugate pad. (**Figure 30a**) However, the SBR then decreased with increasing surfactant concentration. It was hypothesised, that, while at the initial high surfactant concentration the NP flowed freely, the elution was hindered when no surfactant was present in the running buffer. NP that were stuck on the membrane increased the background signal and lowered the SBR. A higher initial surfactant amount led to redispersion and elution of more particles, thus increasing the amount of NP that adhered to the NC membrane outside the test line. In contrast, when the sample pad was pre-treated with surfactant, facilitating a minimum surfactant concentration in the running buffer, the SBR increased with surfactant amount in the conjugate suspension. (**Figure 30b**)

Thus, a higher surfactant concentration in the conjugate buffer promoted redispersion of the NP from the conjugate pad. Even with pre-treated sample pad, the SBR was very low, if no surfactant was added to the conjugate buffer, indicating irreversible binding or aggregation of the NP upon drying. Therefore, addition of surfactants to the conjugate buffer was mandatory for redispersibility of Pdots.

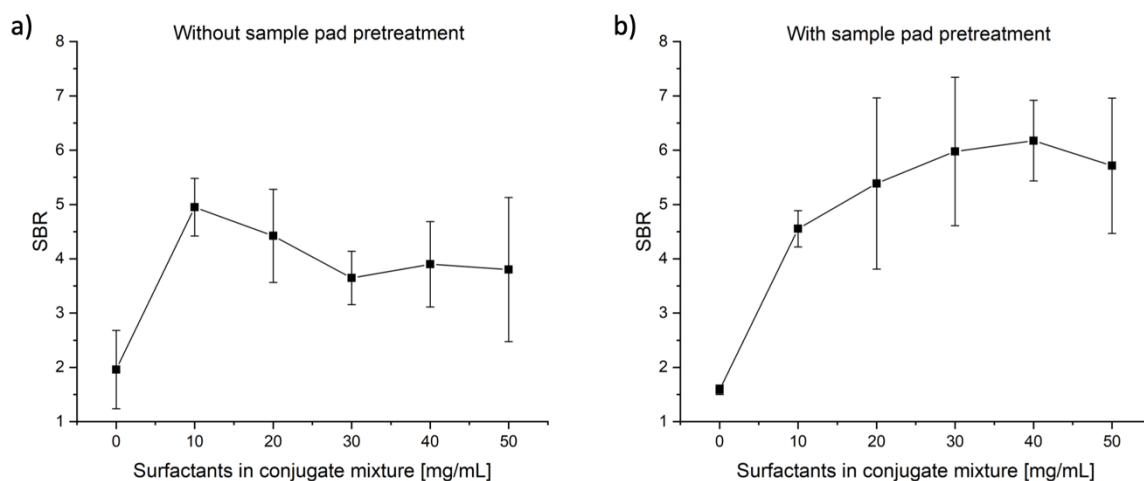


Figure 30: Recovery of IgG-PDOF-Pdots from the conjugate pad without (a) and with (b) pre-treatment of the sample pad with a mixture of 1% Triton X-100, 1% PEG400 and 1% BSA (w/w) in water for different amounts of additive mixture in the conjugate suspension. The additive mixture was composed of Triton X-100, BSA, PEG400, glycerol and sucrose in a 1:1:1:1:1 (w/w) ratio. Values are mean and standard deviations of 3 individual strips.

3.3.4.2 Si-NP

For Si-NP, Tween 20 was chosen as surfactant for the conjugate buffer, as it provided the highest SBR in the running buffer assessment. (**Figure 29**, 3.3.3) Similar to results with Pdots, addition of surfactant was necessary for redispersion of the NP. (**Figure 31a**) No decrease in SBR was observed with increasing surfactant amount over the range tested. The signal intensity, however, was very low in general.

The high standard deviations of SBR after redispersion were most likely caused by irregular distribution of the NP in the conjugate pad or uneven contact between conjugate pad and NC membrane, as indicated by uneven NP flow along the membrane. (**Figure 31b**) For industrial production, more sophisticated equipment would be used, that were not accessible for these studies. To eliminate the influence of the production technique on the signal intensity and give more comparable results between different NP, further studies were performed in a dipstick format.

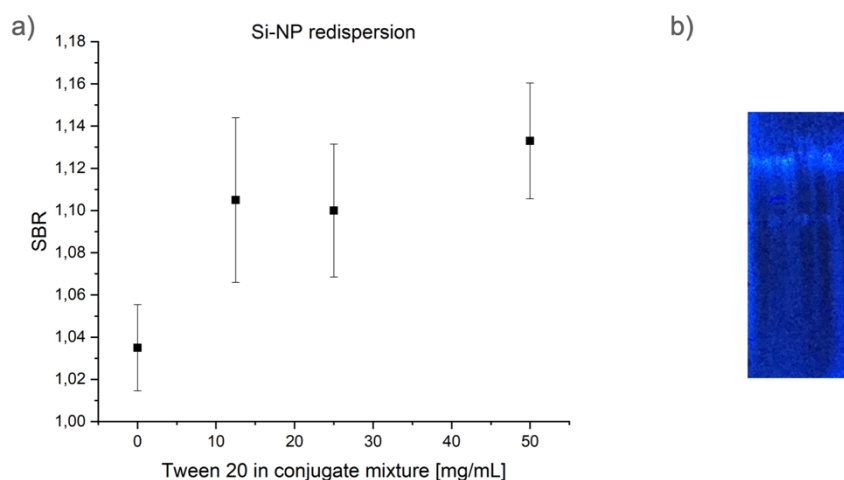


Figure 31: Recovery of IgG-PDOF-Si-NP from the conjugate pad for different concentrations of Tween 20 in the conjugate suspension (a). Values are mean and standard deviations of 3 individual strips. Dissected NC membrane after redispersion of PDOF-Si-NP showing uneven release and flow of the NP (b). Direction of NP flow was from bottom to top.

3.3.5 Dipstick assay with rabbit IgG

Using the optimised conditions, rabbit IgG-conjugated NP were applied to dipstick LFI for comparison of the assay sensitivity. (**Figure 32**)

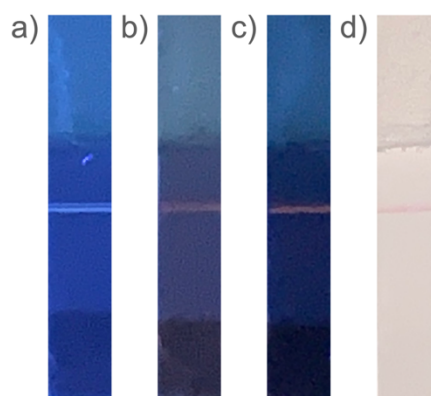


Figure 32: Examples of dipstick LFI with PDOF-Pdots (a), CN-PPV-Pdots (b) and PDOF-CN-PPV-Pdots (c) under a UV lamp ($\lambda_{Ex}=365$ nm). Example of Au-NP dipstick LFI under ambient light (d). The direction of flow was bottom to top.

The model antigen-antibody pair of rabbit IgG-anti-rabbit IgG was chosen, as it was proven to work well in the FLISA microplate assay (Chapter 2.3.6). Even though similar at low NP amounts, the SBR of PDOF-Si-NP was much higher in the high NP mass range, compared to Au-NP. (**Figure 33a**) However, as the density of Au-NP was approximately 10-times higher, compared to Si-NP, the minimum NP number detectable was lower for Au-NP, than for PDOF-Si-NP.

Still, the PDOF-Si-NP outperformed the small-molecule-dye PS-NP. The CN-PPV-Si-NP showed similar SBR, compared to Au-NP and PS-NP over the entire mass range tested. (**Figure 33b**)

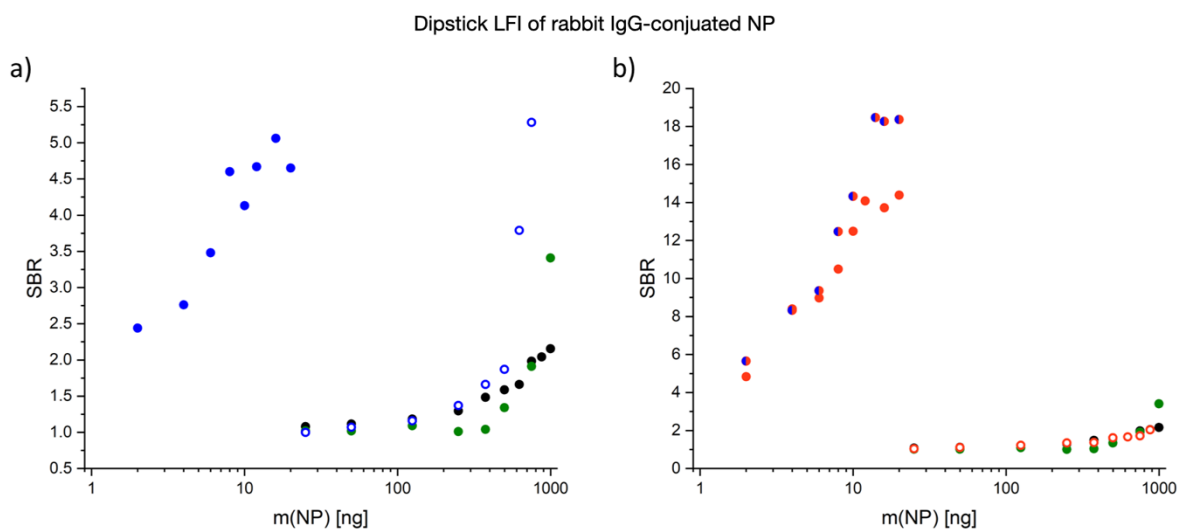


Figure 33: SBR versus NP mass in dipstick-LFI of rabbit IgG-NP conjugates. PDOF-Si-NP (blue open circle) and PDOF-Pdots (blue) compared to PS-NP (green) and Au-NP (black) (a). CN-PPV-Si-NP (red open circle), CN-PPV-Pdots (red) and PDOF-CN-PPV-Pdots (blue-red) compared to PS-NP (green) and Au-NP (black) (b).

In general, Pdots required at least 100-fold less NP mass for detection, compared to Si-NP, PS-NP and Au-NP. (**Figure 33**) Similar to the FLISA microplate assay, the SBR for CN-PPV- and PDOF-CN-PPV-Pdots was much higher than for PDOF-Pdots. The reason, most likely, was the high background signal of the membrane at the PDOF excitation/emission wavelength settings (Chapter 3.3.1). In contrast, the maximum SBR of CN-PPV-Si-NP was lower, compared to PDOF-Si-NP. Given the limited sensitivity of the used detector, a minimum signal intensity was required to generate a detector response. Thus, it was hypothesised, that the high extinction coefficient and QY of PDOF were beneficial in case of low CP LD.

Of all NP tested, the highest SBR was achieved with PDOF-CN-PPV-Pdots. (**Figure 33b**) While the SBR was equal for CN-PPV-Pdots at NP masses lower than 10 ng, higher amounts of NP gave a larger SBR for PDOF-CN-PPV-Pdots. The NC membrane background signal for excitation/emission wavelengths of PDOF-CN-PPV-Pdots was more than twice as high, as for CN-PPV-Pdots. Thus, the higher SBR of PDOF-CN-PPV-Pdots indicated superior signal intensity through improved absorption and efficient FRET in the CP blend system.

3.3.6 Preliminary data with anti-tetracycline, anti-SAE and anti-hFABP IgG: Selected LFI and ELISA-like microplate assay results

For accurate quantitative description and comparison of the sensitivity, the NP systems have to be applied to real samples. A diversity of analytes with practical relevance was chosen for detection to cover a wide range of interests. Tetracycline is an antibiotic, commonly used in veterinary medicine for disease prevention and feed efficiency improvement.¹⁵⁶ To decrease the human uptake of antibiotics through meat, eggs and dairy products, concentration limits of tetracycline in these products are regulated by law. Au-NP-based LFI are commercially available for the detection of tetracycline.¹⁵⁷ Thus, a comparison of CP-based fluorescent LFI with commercial absorption-based LFI is simple. As tetracycline is a very small compound, it features only one Ab-binding site and has to be analysed in a competitive LFI format. *Staphylococcus aureus* enterotoxin A (SAE) is a toxin released by the bacteria, thus indicating an infection.¹⁵⁸ Heart fatty acid binding protein (hFABP) is an early marker for cardiac disease and its detection is beneficial in emergency ambulance.¹⁵⁹ Both antigens feature multiple Ab-binding sites and can be detected in a sandwich-type LFI.

3.3.6.1 Antibody conjugation to Pdots

The optimised conditions for conjugation of rabbit IgG to Pdots were taken forward for conjugation of anti-tetracycline, anti-SAE and anti-hFABP IgG to CN-PPV-Pdots. The IgG-Pdot conjugates had size and zeta potential comparable to the model rabbit IgG-Pdots, indicating successful conjugation. (**Table 7**)

Table 7: Summary of properties of anti-tetracycline, anti-SAE and anti-hFABP IgG-CN-PPV-Pdots in comparison to rabbit IgG-PDOF-Pdots.

	Anti-tetracycline IgG	Anti-SAE IgG	Anti-hFABP IgG	Rabbit IgG ¹
Nr. mean size [nm]	53.9	56.5	59.9	44.4±11.5
Zeta potential [mV]	-13.3	-16.0	-13.6	-15.1±3.5
NP yield [%]	20	23	17	30±4

¹ Mean and standard deviation of 3 batches

3.3.6.2 Dipstick LFI with anti-tetracycline, anti-SAE and anti-hFABP IgG-CN-PPV-Pdots

When applied to dipstick LFI including the respective analytes, no dependence of test line signal on the analyte concentration was observed over the whole range of three orders of magnitude. (**Figure 34**) For tetracycline and SAE, however, the signal at the control line developed in good intensity, indicating successful conjugation of the Ab to the Pdots. The hFABP LFI showed no signal, neither at the test nor the control line. Thus, it is questionable, whether the conjugation reaction, the immunosorption or both failed to work.

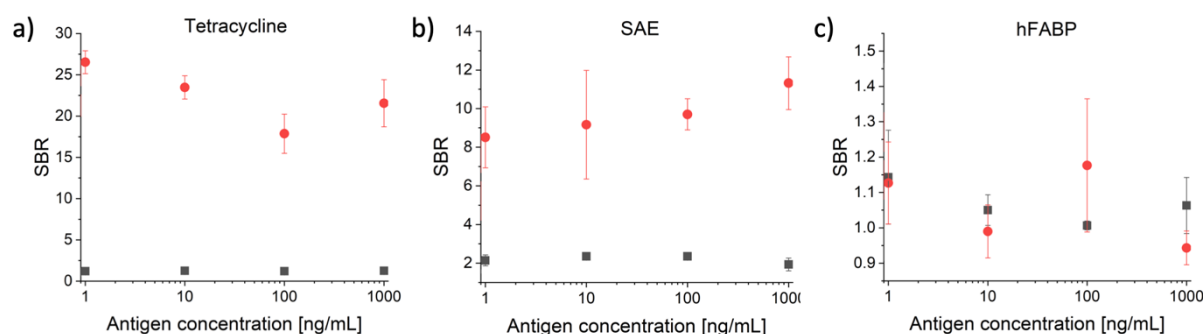


Figure 34: Dipstick LFI with CN-PPV-Pdots. SBR of test line (black) and control line (red) versus concentration of tetracycline (a), staphylococcus aureus enterotoxin A (b) and heart fatty acid binding protein (c). Values are mean and standard deviation of 3 individual strips.

3.3.6.3 ELISA-like microplate assay with anti-tetracycline, anti-SAE and anti-hFABP IgG-Au-NP

The application of Ab-antigen pairs to LFI is limited by the kinetics of the immunoreaction. A fast binding of the antigen to the antibody is required for LFI.¹⁶⁰ For investigation of the immunobinding independent of kinetics and success of the covalent coupling reaction, anti-tetracycline, anti-SAE and anti-hFABP IgG were adsorbed to Au-NP and subjected to ELISA-like microplate assays. With anti-tetracycline IgG the assay design was a competitive format. Thus, a negative correlation between antigen amount and signal intensity was expected. For the sandwich-immunoassay with anti-SAE and anti-hFABP IgG a positive correlation would indicate successful immunobinding.

However, no correlation was observed for anti-tetracycline and anti-SAE IgG-Au-NP. (Figure 35) In contrast to previous results in the dipstick LFI, anti-hFABP IgG showed increased binding with increasing antigen concentration.

As both anti-tetracycline and anti-SAE IgG were bound to the control line in the dipstick LFI, but showed no binding in the Au-NP microplate assay, the antibodies could be successfully conjugated to Pdots, but were not able to bind the antigen. Thus, no LFI could be developed for detection of tetracycline and SAE.

Anti-hFABP IgG showed increase of signal intensity with antigen amount in the Au-NP microplate assay, hence success of immunobinding to the antigen, but no binding in the Pdots dipstick assay. Thus, the antibodies were either not conjugated to the Pdots, or the immunobinding reaction was too slow for the lateral flow format. Optimisation of the conjugation reaction, as well as the flow conditions in the LFI, would be necessary for assay development. However, it is not guaranteed, that antibodies, that work in an ELISA, are working in an LFI, as well. Therefore, no further investigations on the hFABP-Pdot-LFI were done.

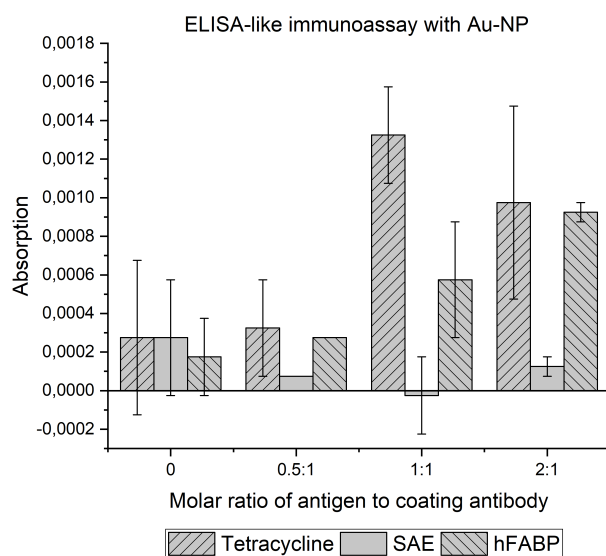


Figure 35: ELISA-like microplate assay of anti-tetracycline, anti-SAE and anti-hFABP IgG-conjugated Au-NP.

3.4 Conclusion

Critical LFI parameters were optimised with regards to SBR for each NP system individually. At the CP excitation/emission wavelengths, the NC membrane Immunopore RP showed the lowest autofluorescence. Application of anti-rabbit IgG capture Ab yielded the highest SBR at a concentration of 500 µg/mL. When the test line intensity was read with a lateral flow reader, the SBR was 10-times higher compared to detection with a mobile phone camera. The addition of surfactants to the running buffer was shown to be crucial for signal development. For Pdots, a mixture of Triton X-100/PEG400/BSA provided the best particle flow. For Si-NP, PS-NP and Au-NP the highest SBR was achieved with Tween 20. The redispersion of NP from the conjugate pad was only possible with surfactant addition in the conjugate mixture. The surfactants in the conjugate pad also provided particle flow in the membrane, but higher SBR were achieved by pre-treatment of the sample pad with surfactants, hence more constant surfactant concentration in the running buffer. The uneven release of particles from the conjugate pad led to a high standard deviation of SBR. Therefore, subsequent LFI were prepared in a dipstick format without sample and conjugate pad.

Dipstick LFI showed superior SBR of CP for high CP loading doses, compared to Au-NP and the small-molecule dye fluorescent NP Fluoresbrite® BB. The SBR of PDOF-CN-PPV- and CN-PPV-Pdots was about 10-times higher, compared to Au-NP. However, CN-PPV-Si-NP showed SBR comparable to both PS-NP and Au-NP. PDOF-Si-NP had a maximum SBR similar to PDOF-Pdots, but at about 50-times higher NP mass. The highest SBR was observed for PDOF-CN-PPV-Pdots. In this CP blend system, the energy of the highly absorptive PDOF was believed to be transferred in a radiationless manner to the large-Stokes-shift CN-PPV by FRET. In general, Pdots required more than 100-fold less NP mass for detection, compared to the other NP systems.

Pdots were also conjugated to anti-tetracyclin, anti-SAE and anti-hFABP IgG, but did not show any binding to the test line in a dipstick LFI. Subsequent ELISA-like microplate investigations using the Au-NP-adsorbed Ab showed, that anti-tetracycline and anti-SAE IgG did not show any immunobinding, while anti-hFABP IgG was either too slow in binding for LFI or was not conjugated to Pdots. Further optimisation of these systems would involve detailed studies of antibody stability or integrity and were therefore beyond the scope of this thesis.

Chapter 4

High-entropy nanozymes as
colorimetric signal transducers in eLFI

4.1 Introduction

4.1.1 Nanozymes

Chemical reactions are usually kinetically hindered, even if thermodynamically favoured. The reason is a high-energy transition state that is only reached by few of the Boltzmann-distributed molecules at a given temperature.¹⁶¹ A catalyst is able to lower the activation energy of the reaction by lowering the energy of the transition state or formation of a low-energy intermediate. A higher portion of molecules is able to overcome the energy differences even at low temperatures and the reaction is faster.¹⁶² An important example is the catalysis of biomolecular reactions by enzymes, biological macromolecules that are characterised by high catalytic activity at body temperature and high specificity towards reaction and substrate.¹⁶³ The drawback of enzymes is their complicated production and isolation, as well as low thermal stability.¹⁶⁴ To overcome these problems, artificial enzymes have been investigated, starting with cyclodextrin for oxidation of α -ketones in 1953.¹⁶⁵ The first artificial macromolecules with catalytic activity were published in 1971 and called “synzymes”, because of their macromolecular nature and outstanding catalytic activity in comparison to small-molecule catalysts.¹⁶⁶ In analogy, the term “nanozyme” was introduced in 2004 for gold NP with functionalised surface that catalysed cleavage of RNA, even though the first nanozyme, fullerene carboxylic acid that could cleave DNA via photocatalysis, was published already in 1993.^{167,168} In comparison to NP-supported catalysts, nanozymes show intrinsic catalytic activity and can be divided in three main groups of metal-based, metal-oxide- or metal-sulfide-based and carbon-based nanomaterials.¹⁶⁹ To date, nanozymes have found numerous applications in redox-based- and photocatalysis.^{170,171}

A surprising discovery in 2007 was the ability of magnetite (Fe_3O_4) NP to catalyse dye oxidation by hydrogenperoxide.¹⁷² Although peroxidase-like catalysis by gold and ceria nanozymes had been reported before, magnetite was considered an inert material until then.^{173,174} Even though numerous highly-cited articles on the catalytic activity of magnetite NP were published afterwards, the experiments were reproduced and the article was harshly criticised in 2018 for not showing proof of catalytic activity at all.¹⁷⁵ One year later, a study on the magnetite NP catalysed formation of hydroperoxyl and hydrosuperperoxyl radicals from hydrogen peroxide was published to prove catalytic activity of the nanozyme independent of a dye substrate.¹⁷⁶ A debate arose, in which critics mentioned that the acceleration of the reactions by magnetite NP is low and less than 0.1 catalytic cycles were performed per Fe_3O_4 unit.¹⁷⁷ Under these conditions the activity of magnetite NP should not be called “catalytic”. The counterargument was that only the surface of the NP are accessible for the reaction and therefore the amount of Fe_3O_4 for the calculation of catalytic cycles was overestimated.¹⁷⁸

To date, regardless of whether or not the magnetite NP should be called “catalytically active”, many applications have been published where an increase of reaction speed was attributed to Fe₃O₄ nanozymes. And even if no catalytic mechanism has been discovered yet, any observable increase in reaction speed mediated by magnetite NP is worth investigating.

4.1.2 Nanozymes in LFI

To increase signal intensity in colorimetric LFI, enzyme-coupled NP may be used to catalyse a colour change reaction. (**Figure 5**) For example, HRP-decorated Au-NP were prepared for an immunoassay for the detection of human IgG. The limit of detection was decreased by a factor of 10 (200 pg/mL) when the enzyme-catalysed oxidation of TMB dye was used to increase colour intensity of the test line, compared to colorimetric readout without additional staining (2 ng/mL).¹⁷⁹ HRP-decorated gold NP for the detection of *E. coli* as model antigen could further reduce the sensitivity by factor of 1000 when a dye oxidation reaction was carried out on the test strip after immunosorption, compared to visual readout without dye-enhancement of the signal. The limit of detection was found to be 10² and 10⁵ CFU/mL, respectively.¹⁸⁰ However, HRP suffers the same drawbacks as other enzymes, namely susceptibility to denaturation and high cost.

A possible solution is the intrinsic catalytic activity of nanozymes. For example, magnetite NP were used in an LFI for the detection of a bunyavirus.¹⁸¹ The lowest concentration that could be detected visually was said to be reduced two orders of magnitude to 1 ng/mL, compared to 100 ng/mL using colloidal gold. But on closer observation, the lowest visually detected concentration of the bunyavirus was as low as 10 ng/mL using magnetite NP alone without successive dye reaction already. Even 0.1 ng/mL were faintly visible without dye reaction and only slightly more pronounced with successive catalytic dye oxidation. This is surprising, as colloidal gold has a high extinction coefficient and should not have such a high detection limit, compared to magnetite NP without colour reaction. But while the antibodies were attached to magnetite NP via a covalent coupling reaction, they have been absorbed to gold NP, which might account for the difference in detection limit. The superior sensitivity of nanozyme-based LFI compared to colorimetric gold assays was more clear for an assay using *E. coli* as a model antigen and porous Pt-Au-NP as the nanozyme.⁵⁴ Both the nanozyme and the colloidal gold reference were conjugated to the antibodies through an adsorption method, but the sensitivity of the nanozyme assay was 1000-fold higher (10² CFU/mL), compared to the colloidal gold (10⁵ CFU/mL).

A challenge for implementation of the signal amplification by catalysed colour change in real applications is the occurrence of natural enzymes in biological matrices. These enzymes could potentially catalyse the same reaction as the nanozyme on the whole test strip, increasing the background intensity. For example, when Pd-Pt-NP were used for *E. coli* detection in spiked milk samples, the limit of detection was reduced only 100-fold for nanozymes (10^2 CFU/mL), compared to gold NP (10^5 CFU/mL).⁵⁵ A workaround is the bleaching of natural enzymes by means of a high H_2O_2 concentration used for the colour change reaction. When Pt-Au-NP were used for the detection of *Potato virus X* in complex matrices, a low detection limit could be reached by use of high (0.2 M) concentrations of H_2O_2 . Compared to the conventional gold LFI, the lowest detectable amount in leaf and tuber extracts was reduced 250- and 500-fold, respectively.⁵²

On overview over recently published catalysis-amplified LFI and the comparison of the detection limit with the colloidal gold colorimetric assay is given in **Table 8**.⁴⁴

Table 8: eLFI systems published with comparison to colorimetric LFI.

Catalytic system	Analyte	Matrix	LOD	Reported LOD		Ref.
				amplification vs. Au-NP	Year	
Fe_3O_4	<i>Ebolavirus</i>	PBS/TRIS	1 ng/mL	100x	2015	181
Pd@Pt nanozyme	<i>E. coli</i> & <i>S. Enteritidis</i>	PBS	34 & 20	33x & 50x	2017	182
			CFU/mL			
Pd-NP	<i>E. coli</i> O157:H7	PBS	10^2 CFU/mL	100x	2018	55
Porous Pt@Au-NP	<i>E. coli</i> O157:H7	PBS	10^2 CFU/mL	1000x	2016	54
Concave Pd-Pt-NP	<i>E. coli</i> O157:H7	PBS & Milk	10^2 & 10^3 CFU/mL	100x & 50x	2017	183
Growth of Au-NP with $HAuCl_4$	<i>Potato virus X</i>	Leaf extracts in PBS	17 pg/mL	240x	2018	184
Pt@Au-NP	<i>Potato virus X</i>	Leaf and tuber extracts in PBS	8 & 4 pg/mL	250x & 500x	2021	52
cLFIA with Pd-NP	hCG	PBS	1 nIU	1000x	2020	44

4.1.3 High-entropy materials: What are they?

The improvement of material characteristics has ever since been a key aim of human society. Starting with pure copper, the composition of man-made metals has become more and more complex over time.¹⁸⁵ Usually, small amounts of additives were added to a bulk of one or two metals to dramatically change the material properties. Unlike conventional alloys, high-entropy alloys (HEA) contain numerous metals in a similar concentration.

While early research on the topic date back to the 1970s, HEA were first named in 2004 and defined as materials consisting of at least five different metals in equimolar ratio.^{186,187} It was initially believed that a high number of constituents would promote formation of amorphous states, but in contrast, experimental analysis revealed formation of a single crystalline phase in HEA.¹⁸⁸ Materials with this composition and characteristics are first generation HEA. As suggested by the name, HEA can also be defined by a high total molar configurational entropy of $S > 1.61R$ (where R is the universal gas constant).¹⁸⁵ This entropy value is considered high, as it usually compensates for the enthalpy of mixing at the melting temperature and therefore, no demixing of the metal alloy melt is observed upon crystallisation.¹⁸⁹ The second definition allows a higher number of possible material compositions. These second generation HEA consist of at least four principal elements of molar portions between 5 and 35% each and might even consist of multiple phases.¹⁹⁰ In general, HEA are materials of a composition that is close to the centre of multicomponent phase diagrams.¹⁹¹

The concept of HEA was also applied to systems that contain non-metal elements to give high-entropy ceramics.¹⁹² A general term combining the former and the latter is high-entropy materials (HEM) or high-entropy nanomaterials (HEN). For HEM with just one type of anion, only the cationic lattices contribute to the configurational entropy and the entropy is calculated as sum of the entropies of each lattice. Thus, for a metal oxide with two cationic lattices of the formula $A_xB_yO_z$, the configurational entropy is calculated as:¹⁹³

$$S_{config} = -R \left[x \left(\sum_{a=1}^M x_a \ln x_a \right)_{A-site} + y \left(\sum_{b=1}^N y_b \ln x_b \right)_{B-site} \right] \quad (9)$$

To distinguish between different compounds of complex composition with regards to entropy, materials with a lower number of different cations, than necessary for a high entropy, are called multi-cationic materials (MCM). In addition to novelty, HEM exhibit exceptional mechanical, physical (electrical, magnetic) and chemical (catalytical, biomedical chemical) properties. It has to be noted that a high configurational entropy does not necessarily induce certain properties. But as the structure is retained after exchange of some of the constituents, the properties are more easily investigated with regard to composition, independent from crystal structure.

4.1.4 High-entropy materials: Possible applications

Most of the research on HEM focuses on their mechanical properties and application as structural materials. Because of their wear-resistance, low density and refractory properties, HEA are proposed for use in aerospace landing gear.¹⁹⁴ Especially the retention of mechanical properties at high temperatures makes them possible candidates to replace titanium and steel alloys in the compressor of jet engines.¹⁹⁵ It was further discovered that HEA could maintain mechanical properties at very low temperatures as well, allowing cryogenic applications, such as cryogenic liquid gas storage.¹⁹⁶ The resistance to and self-healing behaviour under radiation enables use in nuclear power reactors^{197,198} As HEM feature entropy-stabilised structures, they were used as an effective barrier against Cu and Si diffusion in integrated circuits.¹⁹⁹ With the development of advanced coating procedures, HEM have also gained high interest as a coating material, especially for tools and machines.^{200,201}

Apart from their possible improved mechanical and chemical properties, the electrical properties have been investigated for future applications as well. For example, semiconducting HEM have been developed and the use for electronic, optoelectronics, photovoltaic and thermoelectric devices is proposed.²⁰² Many HEA have been investigated for their potential use as superconducting materials, but the critical temperature for superconductivity remains less than 10 K.²⁰³ However, the concept of HEA has been applied to the rare-earth (RE) site of $\text{RE}_1\text{Ba}_2\text{Cu}_3\text{O}_7$ to give superconducting oxides with high critical temperatures above 90 K.²⁰⁴ With high Li-ion conductivity and capacity, as well as cycle-resistance, HEM have been successfully used as anode and cathode material in Li-ion batteries.²⁰⁵⁻²⁰⁷

Because of their tuneable surface chemistry, HEM are also investigated for use in electrocatalysis, especially for renewable energies.²⁰⁸ For example, the limiting step in direct methanol fuel cells is the slow oxidation of the methanol. HEA were found to substantially accelerate the reaction and are therefore suitable catalysts for methanol oxidation.²⁰⁹⁻²¹² Another application in the field of renewable energies is the electrolysis of water. In this process, HEA have been shown to accelerate hydrogen production.²¹³ To further reduce costs of the technique, HEA catalysts without noble metals have been developed.²¹⁴ Furthermore, the oxygen production could be accelerated by use of HEA with lowered noble-metal content.²¹⁵ The latest developments for oxygen generation are HEA electrode materials without any noble-metal, which could even exceed catalytic activity of state-of-the-art catalysts.^{216,217} To economically use the hydrogen of electrolysed water for generation of electricity, the oxygen reduction in fuel cells has to be optimised as well. For this application, HEA were developed that feature high activity, despite reduced content of expensive platinum.^{218,219}

Furthermore, thermal catalysis might be improved by HEM. For example, HEA have shown high conversion and selectivity in NH_3 synthesis.²²⁰ For possible uses in hydrogen storage, NH_3 has to be efficiently degraded after production and storage. As a replacement for expensive ruthenium-containing catalysts, HEA catalysts were developed that improved decomposition of ammonia 20-fold, compared to Ru-based.²²¹ Apart from energy-production, an essential part of sustainable industry is the replacement of fossil sources of hydrocarbons. As one possible way to do so, HEA were successfully applied as catalysts for the conversion of CO_2 to hydrocarbons.²²²

To summarise, due to their wide range of compositions and broad tuneability of properties, HEM can be applied to a vast number of technologies. The development is driven by the need for materials that improve physical, mechanical and chemical properties, reduce cost and spare rare resources. The high number of possible compositions will most likely open the way towards many more possible future applications.

4.1.5 High-entropy materials: Possible biomedical applications as nanozymes

HEN nanozymes have not yet been investigated for biomedical applications. However, many applications for nanozymes in the biomedical field are under investigation and the nanozymes might be replaced by HEN to improve performance and reduce expenses. For example, vitamin C was found to induce oxidative stress by formation of reactive oxygen species (ROS) in certain cancer cells, an effect catalysed by Fe and Pt.²²³ Functionalised Fe_3O_4 @carbon NP were used to catalyse vitamin C-induced oxidative stress in prostate cancer cells and promote apoptosis.²²⁴ Another possibility to cause oxidative stress in tumour cells is to utilise the increased level of H_2O_2 in tumour cells. Pt-NP-decorated metal organic frameworks were used to generate O_2 from abundant H_2O_2 in tumour cells which was turned into $^1\text{O}_2$ by light to induce apoptosis by intracellular oxidative damage.²²⁵ The use of highly catalytically active HEN, instead of Fe_3O_4 @carbon NP and Pt-NP could increase the efficiency of the reaction, as well as reduce the necessary amount of NP to be delivered to the cells. The catalytic activity of nanozymes might also be used outside the body as a disinfectant. For example, the oxidase-like activity of Au-NP on mesoporous silica was used to generate ROS from oxygen and act as an antibacterial agent against both gram-positive and gram-negative bacteria.²²⁶ In this case, HEN could be an inexpensive replacement for the gold catalyst.

By fine tuning of the surface chemistry, nanozymes can be also used to decrease the concentration of ROS. As ROS have been found to induce severe illnesses, nanozymes could be applied as medications.²²⁷ For example, Au-NP produced by algae were used to reduce acetaminophen-induced oxidative damage of hepatocytes *in vitro*.²²⁸

In rats, the antioxidant properties of cross-linked nanozymes were shown to reduce ischemia-induced brain injury even *in-vivo*.²²⁹ However, the short half-life, poor passage through the blood-brain-barrier, proteolysis and immunogenicity are challenging. Additional to medical treatment, preservative applications are also possible. Apoferritin-containing Ag-Au-NP, for example, were successfully used as antioxidative agent for cryopreservation of human sperm.²³⁰

Finally, nanozymes may also improve the sensitivity of colorimetric LFI. For example, hierarchically structured Pt-NP were used to intensify the signal by catalysis of a dye reaction at the test and control line of an LFI. For the detection of human chorionic gonadotropin (hCG), the sensitivity could be increased 20-fold, compared to conventional Au-NP-based colorimetric LFI.²³¹ However, platinum is an expensive noble metal and may not be cost-effective in disposable tests such as LFI. To decrease the platinum content and at the same time increase sensitivity, Pt-decorated magnetite NP were used as nanozymes. While the magnetite core could be utilised to enrich the analyte concentration in the sample by magnetic separation, the Pt-decoration of the surface led to a high catalytic activity. With this approach, hCG-detection sensitivity was increased 150-fold, compared to conventional Au-NP based LFI.⁵³ The noble-metal-free HEA CrMnFeCoNi showed electrocatalytic activity for the oxygen reduction reaction at least as high as the state-of-the-art platinum on carbon.²³² Thus, it is likely, that HEN can replace the nanozymes in the abovementioned biomedical applications.

4.1.6 Target specifications of NP, study questions and hypothesis

Fe₃O₄ NP have already been published for use as nanozymes in eLFI. To investigate whether HEN may be superior to Fe₃O₄ NP in eLFI assays, basic investigations of the catalytic activity i.e., acceleration of dye oxidation reaction, must first be performed. It was hypothesised that the cocktail effect in different HEN compositions may lead to surfaces with enhanced peroxidase-like activity when compared with Fe₃O₄ NP. To study this, collaborators at the Karlsruhe Institute of Technology prepared three different HEN and four different MCM species with the compositions and configurational entropies, as calculated with **Equation 9**, listed in **Figure 36**. Two species of Fe₃O₄ NP with different diameters (bm-Fe₃O₄, ball-milled = ~200 nm; np-Fe₃O₄, non-processed = ~800 nm) were also provided as reference materials. HEN were dispersed with different surfactants and the impact of surfactant type and quantity on the catalytic activity was measured using two colorimetric dyes, TMB and DAB. Following dispersion, the HEN and Fe₃O₄ NP were conjugated with a model antibody, rabbit IgG, and investigated in an ELISA.

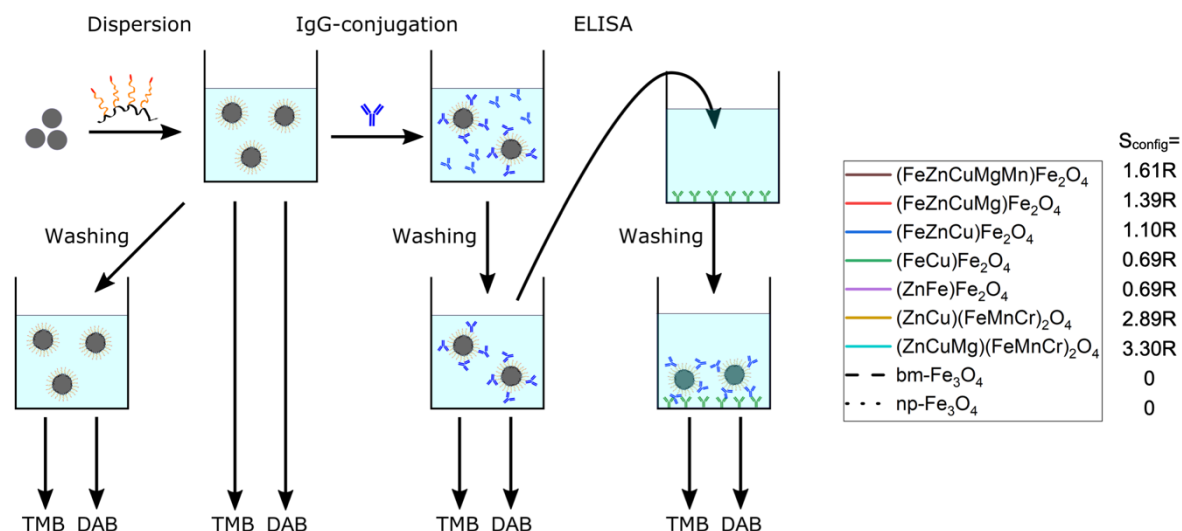


Figure 36: Experimental design for the investigation of MCM and HEN catalytic activity.

4.2 Materials and methods

4.2.1 Materials

FeO, CuO, Fe₂O₃, MgO, Cr₂O₃, Mn₂O₃, ZnO, 3,3',5,5'-tetramethylbenzidine (TMB), 3,3'-diaminobenzidine (DAB) and hydrogen peroxide solution (30 wt. % in H₂O) were of analytical grade from SigmaAldrich.

4.2.2 Nanozyme preparation

The nanozymes were kindly provided by the group of Dr. Ben Breitung, Karlsruhe Institute of Technology. They were produced by mixing the metal oxide precursors FeO, CuO, Fe₂O₃, MgO, Cr₂O₃, Mn₂O₃ and ZnO in the respective masses to achieve the desired M₃O₄ stoichiometry. The oxides were ball-milled at 500 rpm for 14-26 h in an argon atmosphere, using a Retsch PM 100 ball-milling machine.

4.2.3 Dispersion and physicochemical characterisation

10 mg samples were dispersed in 10 mL 50 mM TRIS buffer pH=7.4 containing either 0.1% Tween 20 (pilot studies), 0.005% or 0.1% PS-g-PEG-COOH (antibody conjugation) and sonicated for eight minutes, vortexing every two minutes. Hydrodynamic diameters and zeta potential were measured with a Malvern Zetasizer ZS Nano equipped with 633 nm laser at a scattering angle of 173°. The samples were diluted in deionised water to a final concentration of 0.1 mg/mL prior to size measurement at 25 °C.

The sizes reported are mean values of number distributions. Samples were diluted in 10 mM KCl to a final concentration of 0.05 mg/mL for zeta potential measurements. Zeta potentials were calculated from electrophoretic mobilities using the Smoluchowski approximation setting in the Zetasizer Nano software v3.30.⁹⁰

4.2.4 Peroxidase-like activity of dispersions with different compositions

100 μ L samples (80, 8 or 0.8 μ g/mL) in 50 mM TRIS buffer pH=7.4 containing 0.1% Tween 20 were added to a 96-well plate. Subsequently, 100 μ L TMB or DAB solution (1632 μ M) in 0.4 M sodium acetate buffer pH=4 (TMB) or 0.05 M TRIS pH=7.4 (DAB) were added and incubated for 15 minutes. The dye solutions contained 100 mM H₂O₂ (TMB) or 1060 mM H₂O₂ (DAB). Additionally, all experiments were performed under the same conditions in the absence of H₂O₂, to determine the background absorption and sample influence on the dye colour independently of H₂O₂, especially at higher concentrations. Final nanozyme concentrations tested were 40, 4 and 0.4 μ g/mL. The dye absorption was measured every two minutes at 650 nm (TMB) or 471 nm (DAB) and the absorption of the blank wells was subtracted.

In a second experiment, the nanozyme concentration was adjusted for each sample to match 1) the molar content of Fe(II) (or Fe(III)) in the sample compared to Fe₃O₄ controls. and 2) the surface of Fe(II) (or Fe(III)) in np-Fe₃O₄ according to **Equation 10. (Table 9)**

$$c(NP) = c(np-Fe_3O_4 \text{ 818 nm}) * \frac{d(NP)}{d(np-Fe_3O_4)} * \frac{w_{Fe(II)}(NP)}{w_{Fe(II)}(np-Fe_3O_4)} \quad (10)$$

Table 9: Concentrations of nanozymes in assessment of catalytic activity to match the molar content of Fe(II) or Fe(III) or the molar content of Fe(II) or Fe(III) on the NP surface in the sample to np-Fe₃O₄.

Sample	Final NP concentration in assay [μ g/mL]	
	Equimolar Fe(II)	Equimolar Fe(II) per surface area
(FeZnCuMgMn)Fe ₂ O ₄	197.5	43
(FeZnCuMg)Fe ₂ O ₄	157.5	52
(FeZnCu)Fe ₂ O ₄	123	24.5
(FeCu)Fe ₂ O ₄	81.5	17.5
(ZnFe)Fe ₂ O ₄	81.5	23
(ZnCu)(FeMnCr) ₂ O ₄	122.5	19
(ZnCuMg)(FeMnCr) ₂ O ₄	115.5	19.5
Fe ₃ O ₄ (ball-milled)	40	12.5
Fe ₃ O ₄ (non-processed)	40	40

4.2.5 Antibody conjugation (rabbit IgG) to selected materials

10 mg selected nanozyme samples were dispersed under ultrasonication in 10 mL 50 mM TRIS pH=7.4 containing 0.005% or 0.1% PS-g-PEG-COOH as described above. Dispersions (1 mL) were mixed with a solution of 5% PEG400 in water (40 μ L) and 1 M HEPES buffer pH=7.4 (40 μ L). Subsequently, freshly prepared solutions of 1% EDC in water (40 μ L) and 1% NHS in water (10 μ L) were added and mixed for 5 min. A solution of 0.1 g/L rabbit IgG in water (367 μ L) was added and the mixture was stirred for 2 h at RT. A solution of 1% BSA in water (10 μ L) was added and the suspension stirred for 30 min. The suspensions were washed three times by centrifugation at 15000 x g for 5 min and redispersion in 2 mL 50 mM TRIS pH=7.4 and finally redispersed in 1 mL 50 mM TRIS pH=7.4 containing 0.1% Tween 20.

4.2.6 ELISA performance

50 μ L of goat anti-rabbit IgG in 0.1 M borate buffer pH=9 (20 μ g/mL) were added to a 96-well plate. The plate was covered and incubated at 4 °C overnight, then washed twice with 200 μ L TRIS pH=7.4 containing 0.05% Tween 20. The remaining binding sites were blocked by adding 150 μ L PBS containing 1% BSA, covering the plate, incubating for 2 h at room temperature, and washing twice with 200 μ L TRIS pH=7.4 containing 0.05% Tween 20. Rabbit IgG-nanozyme conjugates were diluted in TRIS pH=7.4 containing 0.05% Tween 20 and 1 mg/mL BSA at concentrations of 500, 250, 100, 50 and 10 μ g/mL and 100 μ L were added to each well. The plate was covered, incubated at room temperature for 2 h, then washed three times with 200 μ L TRIS pH=7.4 containing 0.05% Tween 20 and filled with 100 μ L TRIS pH=7.4 containing 0.05% Tween 20. TMB substrate solution was prepared by mixing 700 μ L 4 M sodium acetate buffer pH=4, 274 μ L TMB (10 mg/mL in DMSO), 76 μ L H₂O₂ and 6090 μ L H₂O. 100 μ L TMB substrate solution were then added to each well and the absorbance was read at 650 nm every 2 min for 15 min.

DAB substrate solution was prepared by mixing 700 μ L 0.5 M TRIS pH=7.4, 245 μ L DAB (10 mg/mL in DMSO), 756 μ L H₂O₂ and 5299 μ L H₂O. 100 μ L DAB substrate solution were then added to each well and the absorbance was read at 471 nm every 2 min for 15 min.

4.3 Results

4.3.1 Dispersion and physicochemical characterisation

The catalysis by magnetite NP is said to occur on the particle surface.¹⁷² Therefore, MCM and HEN are believed to perform heterogeneous catalysis as well. The reaction speed of two-phase reactions depends on the interface area.²³³ Thus, a comparison of catalytic activities by mass of different materials is only valid for similar NP sizes. For application of the MCM and HEN to immunoassay, the surface needs to be decorated with reactive moieties that can be conjugated to Ab. It was shown, that surfactants and polymers are able to adsorb to iron oxide surfaces.²³⁴ For stabilisation of the NP suspension, as well as introduction of functional groups, PS-g-PEG-COOH was used as surfactant, a strategy that was shown to work well with Pdots. (Chapter 2) Concentrations of 0.005% and 0.1% (w/v) were chosen to resemble the surface-to-surfactant amount ratio in Pdots and use the highest soluble amount, respectively. Tween 20 was used as non-ionic surfactant for comparison. The molecular weight of Tween 20 is much lower compared to PS-g-PEG-COOH. Therefore, it could possibly have a denser surface coverage on the NP, which would affect stability and catalytic activity. The hydrodynamic diameter of the HEN suspensions was evaluated by DLS. The nanoyzmes had comparable sizes between 100 and 300 nm in 0.1% surfactant, similar to the bm-Fe₃O₄ standard. (**Figure 37**) With only 0.005% PS-g-PEG-COOH most of the NP showed an increase in size, attributed to increased particle aggregation.

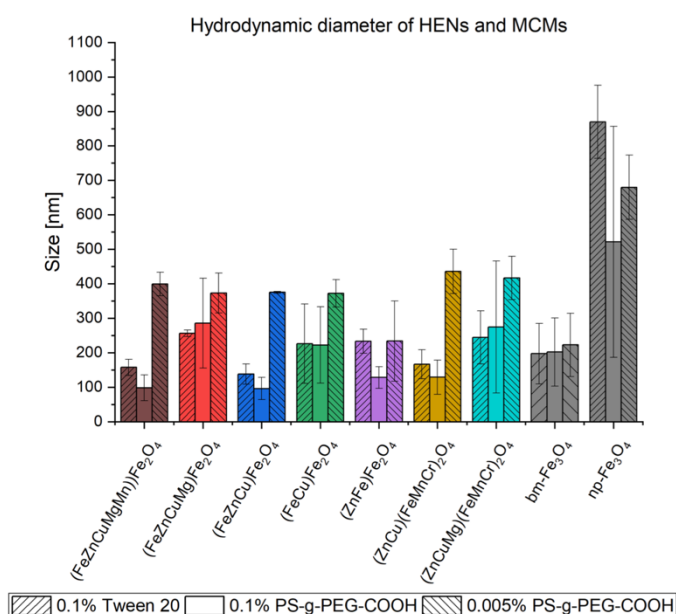


Figure 37: Hydrodynamic diameter of NP dispersed in 0.1% Tween 20, 0.1% PS-g-PEG-COOH or 0.005% PS-g-PEG-COOH. Data shows mean and standard deviation of two replicates.

4.3.2 Peroxidase-like activity of dispersions with different compositions

4.3.2.1 Peroxidase-like activity of dispersions of varying concentration

To assess the catalytic activity of MCM and HEN, the colour change of two typical substrates for ELISA (DAB and TMB) was observed over time. DAB is oxidised by H_2O_2 to form a brown diamine product, with an absorption maximum at 471.²³⁵ (**Figure 38a**) TMB is oxidised in a one-electron process to a cation radical, that disproportionates into a diamine and the native TMB molecule, both of which together form a blue charge-transfer complex with strong absorbance at 650 nm.²³⁶ (**Figure 38b**)

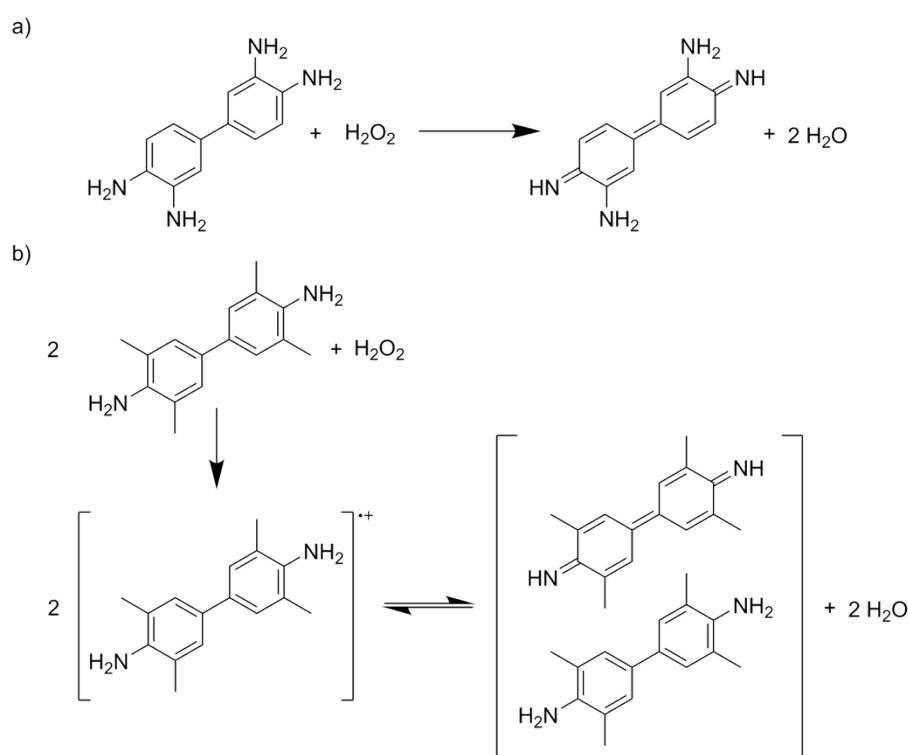


Figure 38: Reaction scheme of oxidation of DAB (a) and TMB (b).

It has to be noted, that “peroxidase-like” is a term commonly used by researchers in the nanozyme field for any acceleration of HRP-substrate oxidation by H_2O_2 , regardless of the mechanism.¹⁷⁸ Natural HRP catalysis usually involves a two-electron transfer, split in two one-electron transfers, in which the central iron of the enzyme cycles between Fe(III) and Fe(IV).²³⁷ The iron oxidises the substrate and is, in turn, oxidised by H_2O_2 . It is known, that artificial substrates, that are widely used with HRP in ELISA, are oxidised by HRP in a one-electron process.^{236,237} Metal oxide nanozymes are different in that they do not oxidise the substrate, but reduce H_2O_2 or O_2 to reactive radicals, which then oxidise the substrate.^{176,177} The subsequent reduction of the oxidised nanozymes, as a requirement to form a catalytic cycle,

is, to the best of my knowledge, not proven to date. It is therefore debatable, whether the role of the MCM and HEN in the reaction of the following investigations is catalyst or reactant.

However, proof of the mechanism of action is out of scope of this thesis and any acceleration of reaction is going to be referred to as catalysis, for better comprehension. The improvement of substrate oxidation in the presence of MCM or HEN was systematically evaluated.

At first it was investigated, which concentration of NP was required for observable differences in reaction speed. In reaction mixtures with final MCM or HEN concentrations of 0.4, 4 and 40 $\mu\text{g/mL}$ the changes in absorption were more pronounced with increasing amount of NP. **(Figure 39)** Moreover, only for the highest MCM and HEN concentration the differences were high with respect to standard deviations. Therefore, a concentration of 40 $\mu\text{g/mL}$ NP in the reaction mixture was used for further experiments.

Under the chosen reaction conditions, the changes of concentration of the reactants were small with respect to the absolute concentration values, leading to apparent steady-state kinetics. As a result, the absorption increased almost linearly with time. Thus, the reaction speed was considered constant, hence calculated as slope of absorption versus time in successive investigations.

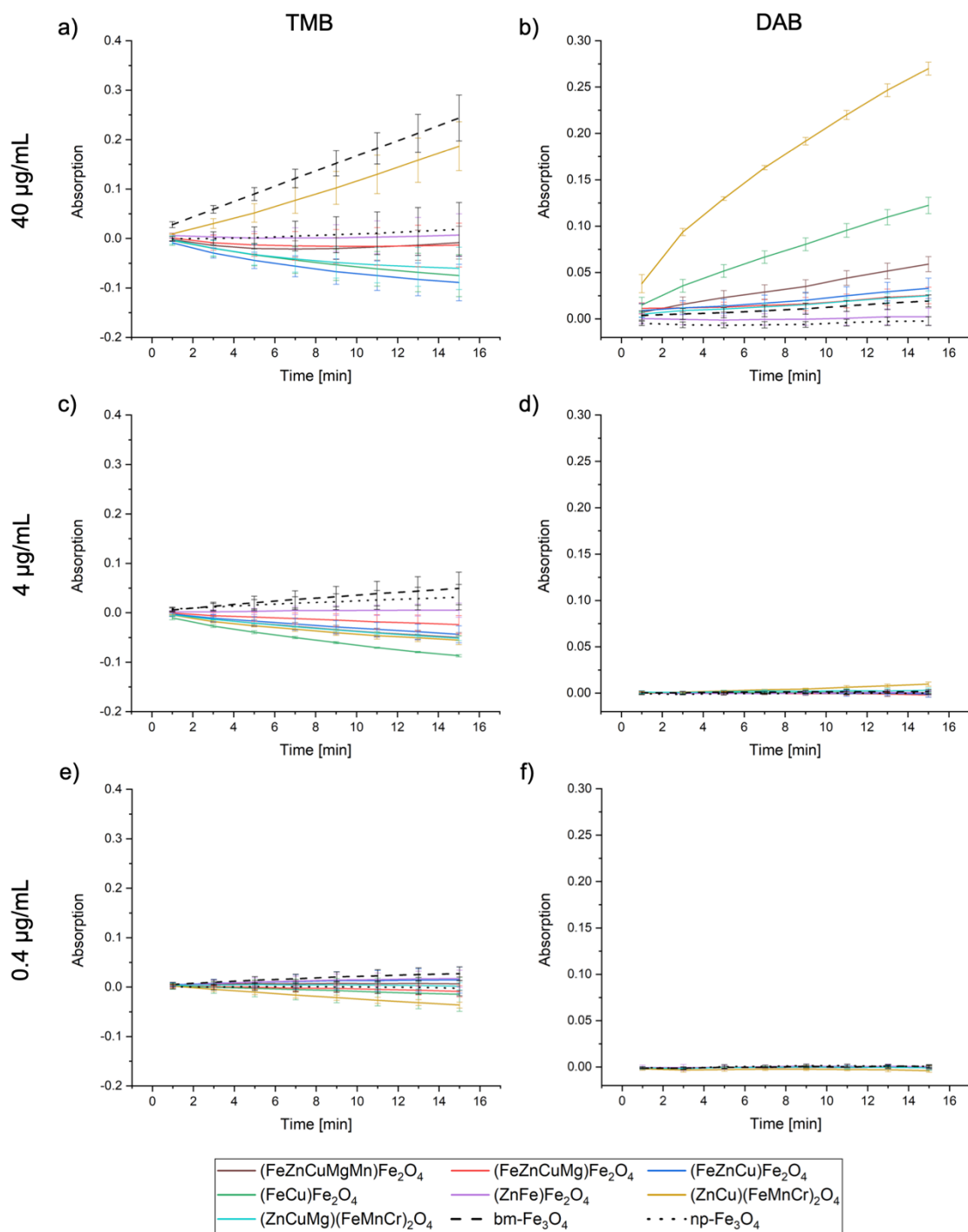


Figure 39: Absorption of solutions of TMB (a, c, e) or DAB (b, d, f) oxidised by H_2O_2 in the presence of 40 (a, b), 4 (c, d) or 0.4 (e, f) $\mu\text{g/mL}$ NP dispersed in 0.1% Tween 20. Absorption of wells without H_2O_2 and absorption of wells with H_2O_2 , but no catalyst, were both subtracted from the sample absorption values. Data shown is the mean and standard deviation of 3 individual wells distributed over 3 individual plates from a single MCM or HEN batch.

4.3.2.2 Intra and interday variability of peroxidase-like activity of MCM and HEN dispersions with different dispersant

Given the large standard deviations of absorption relative to the difference between mean MCM or HEN values for TMB oxidation, verification of reproducibility of the catalytic assay was necessary. Therefore, the same NP dispersions were subjected to catalytic testing on three individual plates. Furthermore, the influence of statistical errors for NP suspension preparation had to be evaluated. Thus, two more individual dispersions of each NP were produced on different days and the catalytic activity was investigated separately. All of the experiments were performed with three different dispersant media to investigate the influence of type and concentration of the surfactant on catalytic activity of the MCM and HEN. The catalytic assay was reproducible and the standard deviations of means were small, compared to the differences in reaction speed. (middle bars, **Figure 40**) Moreover, preparation of individual NP dispersions resulted in similar catalytic activities. (individual bars, **Figure 40**) Therefore, both the preparative and analytical procedures were reproducible. More importantly, the changes in reaction speed induced by HEN materials could be considered true phenomena, rather than statistical errors.

In general, the reaction speeds in Tween 20 were lower compared to PS-g-PEG-COOH suspensions. It was hypothesised, that the small Tween 20 surfactant molecule was able to cover the NP surface in a denser manner, compared to the bulky polymer, therefore blocking more reactive sites. The amount of PS-g-PEG-COOH did not influence the reaction speed, except for oxidation of DAB in the presence of $(\text{ZnCu})(\text{FeMnCr})_2\text{O}_4$, which was faster for the low polymer concentration. For a more comprehensive evaluation, the reaction speeds of solutions containing only H_2O_2 (H_2O_2 background) were subtracted from the reaction speeds with NP in later experiments to show the acceleration of the reaction achieved specifically by the nanozymes. For the purposes of this thesis, this normalised reaction speed was referred to as the “catalytic activity” of the sample. Even though reaction speeds in Tween 20 were lower, the proportions of catalytic activity between nanozymes were comparable to dispersions in PS-g-PEG-COOH. For this reason, Tween 20 was used as dispersant in the follow-up experiment and the rather expensive polymeric surfactant was only used for successive experiments including Ab-conjugated nanozymes.

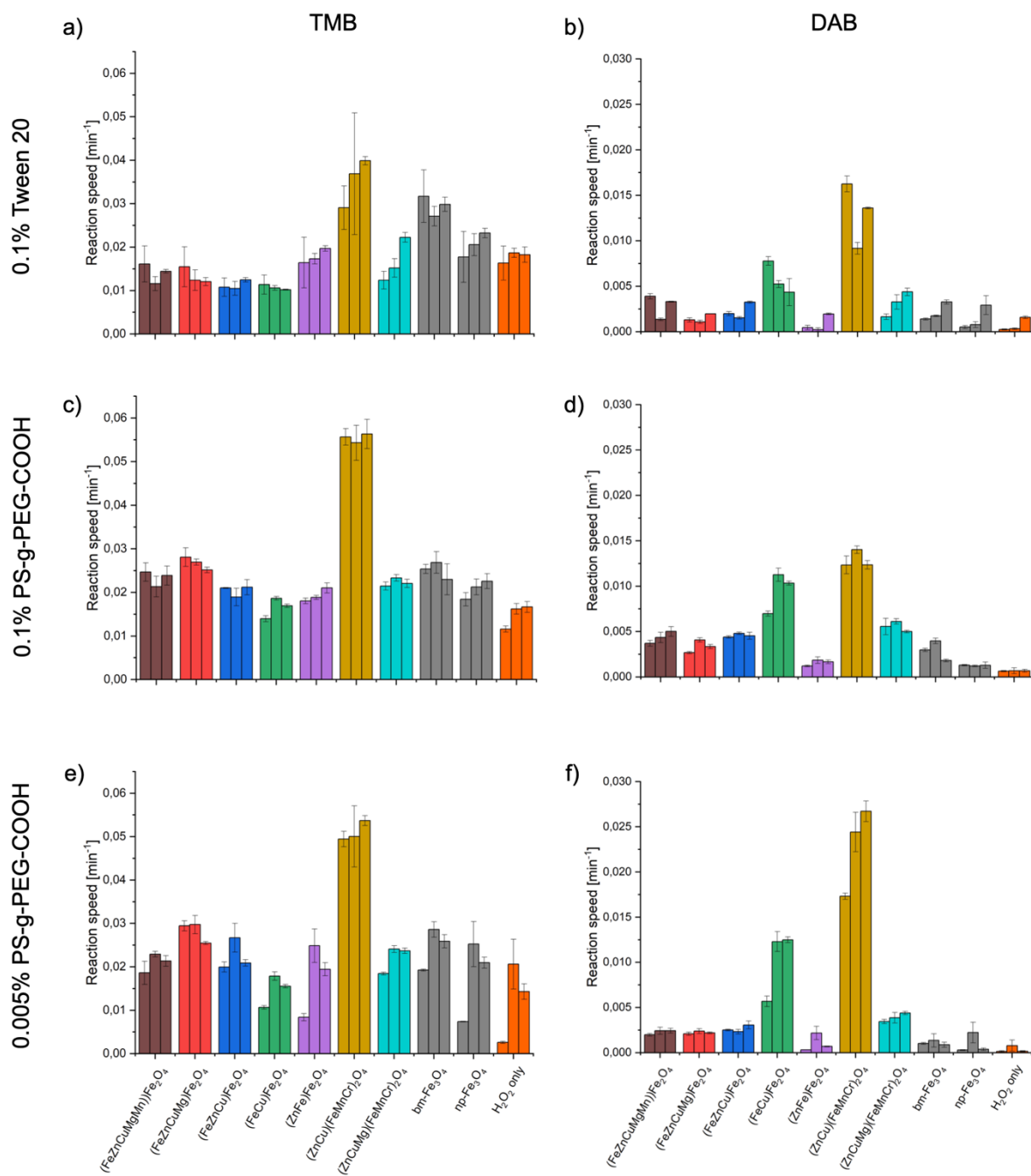


Figure 40: Reaction speed e.g., slope of absorption versus time, for oxidation of TMB (a, c e) and DAB (b, d, f) catalysed by NP dispersed in 0.1% Tween 20 (a, b), 0.1% PS-g-PEG-COOH (c, d) or 0.005% PS-g-PEG-COOH). Background values of wells with MCM or HEN, (without H₂O₂) were subtracted. Each bar of one group shows an individual NP dispersion replicate on an individual plate. Values are mean values and standard deviation of three individual wells per plate. Each middle bar of a group shows one NP dispersion on three replicate plates with three replicate wells each and values are reported as mean and standard deviation of means.

4.3.2.3 Peroxidase-like activity of dispersions of same Fe(II) content

The active centre of catalysis for peroxidase-like activity of Fe_3O_4 is believed to be Fe(II).^{172,238} To investigate the catalytic activity of the iron in MCM and HEN in comparison to Fe_3O_4 , the concentration of NP were adjusted to match the molar concentration of Fe(II) in the samples of the np- Fe_3O_4 . Samples without Fe(II) were used in concentrations matching the molar content of Fe(III), accordingly. In all of the experiments, $(\text{ZnCu})(\text{FeMnCr})_2\text{O}_4$ had superior catalytic activity in comparison to the other samples and the bm- Fe_3O_4 standard. **(Figure 41)** Based on Fe(II) content, $(\text{FeZnCuMgMn})\text{Fe}_2\text{O}_4$ and $(\text{FeCu})\text{Fe}_2\text{O}_4$ showed higher activity for oxidation of DAB, compared to the other MCM and HEN, as well as the bm- Fe_3O_4 . The same was observed when the NP concentration was adjusted to match the molar Fe(II) or Fe(III) content multiplied with the estimated NP surface area, e.g. Fe(II) or Fe(III) surface area. **(Figure 41d)** However, for oxidation of TMB only the HEN $(\text{ZnCu})(\text{FeMnCr})_2\text{O}_4$ and $(\text{FeZnCuMgMn})\text{Fe}_2\text{O}_4$ had higher catalytic activity, compared to the bm- Fe_3O_4 NP for same Fe(II) or Fe(III) content. **(Figure 41a)** Surprisingly, the material with the highest catalytic activity ($(\text{ZnCu})(\text{FeMnCr})_2\text{O}_4$) did not contain any Fe(II). The properties of HEM are usually not just the sum of the properties of single components, but may be very different in combination, a feature called “cocktail effect”¹⁸⁹ An example for this phenomenon was seen for the highly active $(\text{ZnCu})(\text{FeMnCr})_2\text{O}_4$. The addition of only one magnesium atom in the crystal lattice dramatically changed the property of the material and the resulting $(\text{ZnCuMg})(\text{FeMnCr})_2\text{O}_4$ showed highly reduced activity. For this reason, both materials and the quite active $(\text{FeZnCuMgMn})\text{Fe}_2\text{O}_4$ and $(\text{FeCu})\text{Fe}_2\text{O}_4$, as well as the bm- Fe_3O_4 standard were conjugated to rabbit IgG and applied to an immunoassay.

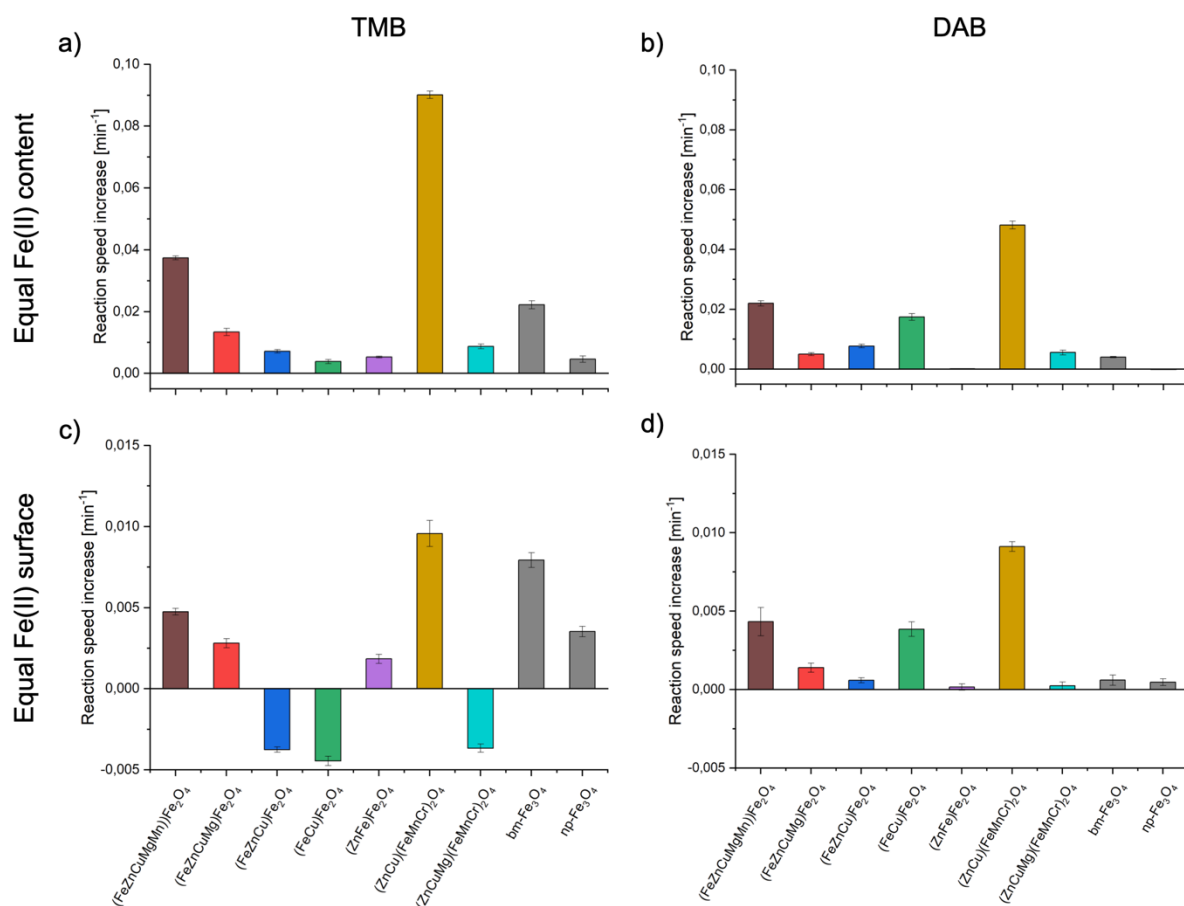


Figure 41: Acceleration of TMB (a, c) or DAB (b, d) oxidation by H_2O_2 in the presence of MCM and HEN over reaction with only H_2O_2 . Values of wells without H_2O_2 were subtracted. The NP amount was adjusted to the molar content of Fe(II) or Fe(III) (a, b) or surface area of Fe(II) or Fe(III) (c, d) in the np-Fe₃O₄ NP. Values are mean and standard deviation of 3 individual wells from a single material batch.

4.3.3 Antibody conjugation (rabbit IgG) to selected materials

The conjugation procedure that was established for Pdots (Chapter 2) was applied to MCM and HEN with minor changes. Most importantly, the NP could be purified by centrifugation, because of the larger size and higher density of the metal oxide NP, compared to Pdots, which had to be worked up by time-consuming SEC.

4.3.3.1 Physicochemical properties of conjugates

Compared to unconjugated NP, the conjugated samples showed an increased size and reduced zeta potential, indicating alteration of the particle surface. (**Table 10**) While the increase in size of (FeZnCuMgMn)Fe₂O₄ was approximately the expected value for addition of a layer of Ab, the other samples, including bm-Fe₃O₄, exhibited much larger diameters after conjugation, indicating a possible aggregation of the particles. However, the zeta potentials of selected samples changed in the same manner, indicating the same change in surface chemistry, e.g., conjugation of Ab. Surprisingly, the zeta potential of bm-Fe₃O₄ did not change at all after conjugation. Given the comparable zeta potential and particle size of the crude NP dispersions, no different behavior was expected for the coupling reaction. For more solid evidence, the success of Ab conjugation to the NP was further assessed in an immunoassay.

Table 10: Number mean hydrodynamic diameter and zeta potential of the same MCM, HEN and bm-Fe₃O₄ NP dispersions before and after conjugation to rabbit IgG.

	Size [nm]		Zeta potential [mV]	
	unconjugated	IgG conjugate	unconjugated	IgG conjugate
(FeZnCuMgMn)Fe ₂ O ₄	177.7	195.6	-23.1	-17.6
(FeCu)Fe ₂ O ₄	174.7	336.7	-24.1	-18.6
(ZnCu)(FeMnCr) ₂ O ₄	125.4	435.1	-22.3	-15.6
bm-Fe ₃ O ₄	260.0	356.8	-22.1	-22.7

4.3.3.2 Interday variability of peroxidase-like activity of selected dispersions of rabbit IgG-conjugated MCM and HEN

The three most active samples, as well as bm-Fe₃O₄ were used for the investigation. To evaluate reproducibility of the conjugation reaction, all conjugates were prepared in triplicate. The influence of surface coverage on catalysis was furthermore investigated by conjugation of materials dispersed in two different concentrations of surfactant polymer. It was shown that the catalytic activity between batches was comparable and the conjugation reaction was therefore considered reproducible. (**Figure 42**) However, loss of activity was observed for all of the NP conjugates, compared to unconjugated dispersions. As the acceleration of the reactions was measurable to at least some extent, the surface of the NP was considered still active and the MCM and HEN were subjected to microplate immunoassays.

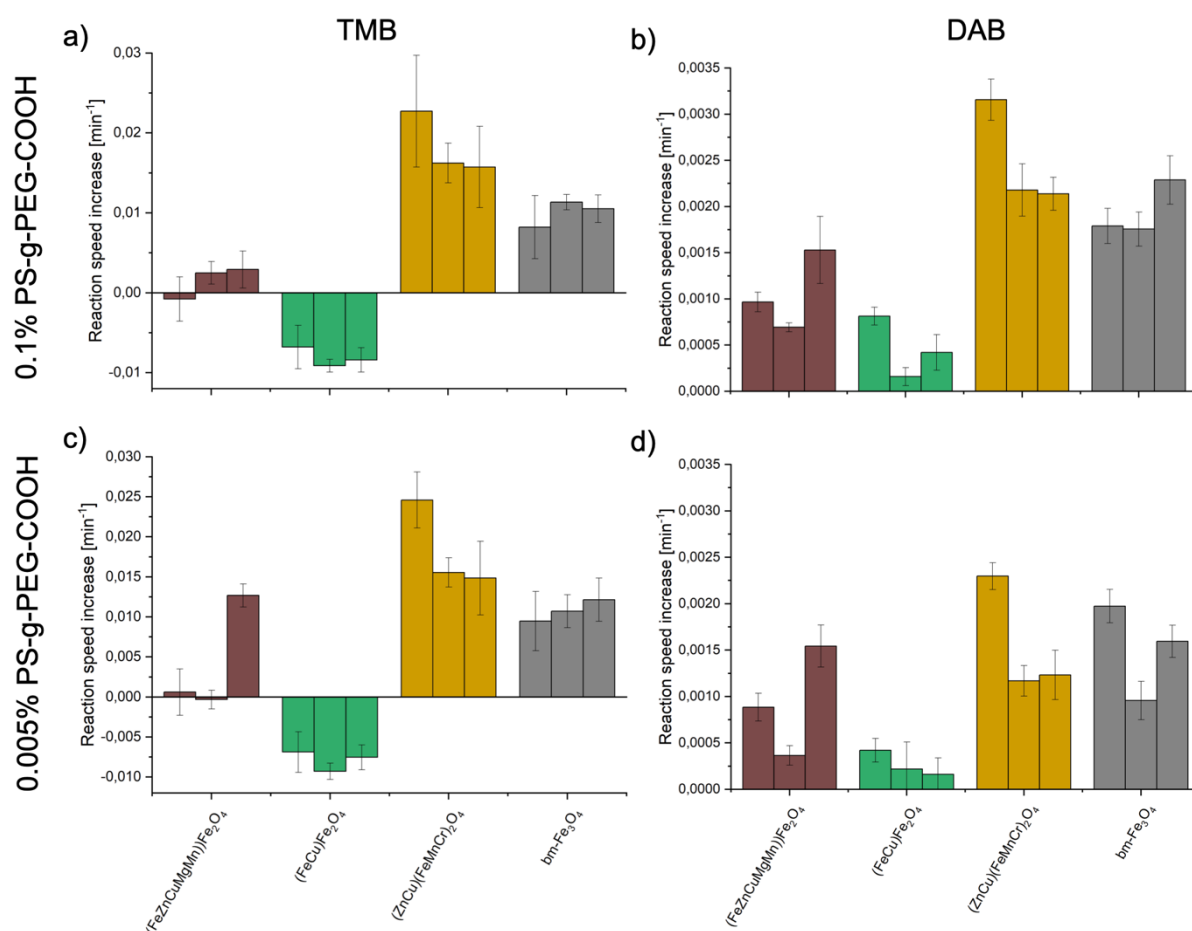


Figure 42: Acceleration of TMB (a, c) or DAB (b, d) oxidation by H_2O_2 in the presence of MCM and HEN over reaction with only H_2O_2 . 40 $\mu\text{g}/\text{mL}$ IgG-conjugated NP were dispersed in 0.1% PS-g-PEG-COOH (a, b) or 0.005% PS-g-PEG-COOH (c, d). Reaction speed of wells without H_2O_2 was subtracted from the values. Each bar of one group shows an individual NP conjugate replicate on an individual plate. Values are mean and standard deviation of three individual wells per plate.

4.3.4 ELISA performance

4.3.4.1 Concentration-dependence of peroxidase-like activity of selected rabbit IgG-conjugated MCM and HEN bound in an ELISA

The number of particles available for catalysis in a microplate immunoassay is limited by the surface of the wells, that is covered with capture Ab. NP of similar size possess a similar surface area and it was therefore hypothesised, that the number of particles in the immunoassay would be the same for all conjugates, if the coverage was maximised. Different amounts of conjugates were incubated in the ELISA, to find the amount of maximised immunobinding. Wells coated with BSA only (no capture Ab), were also incubated with the conjugates, to distinguish immunobound from sedimented particles.

It was observed that wells without capture Ab had lower absorption values compared to the wells with the same conjugate and coated with capture Ab, indicating a low level of nonspecific binding. (Figure 43)

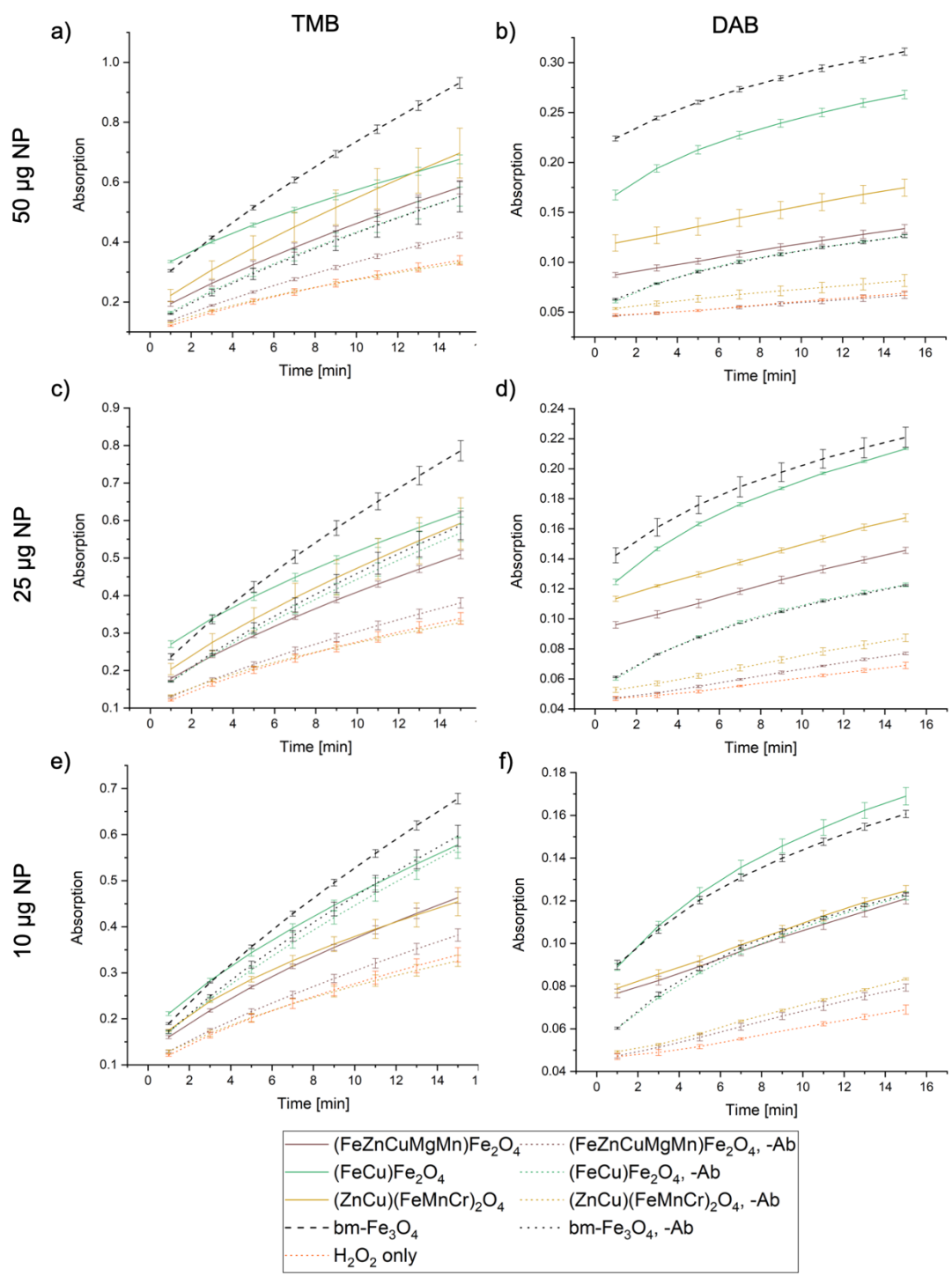


Figure 43: ELISA of 5 (g, h), 10 (e, f), 25 (c, d) and 50 (a, b) µg IgG-conjugated NP in wells coated with anti-rabbit IgG (solid or segmented lines) or only coated with BSA (dotted lines). Absorption over time with TMB (a, c, e, g) or DAB (b, d, f, h) substrate. Values are mean and standard deviation of three individual wells.

Accordingly, the reaction speed was increased for wells with capture Ab coating. Furthermore, an increase in reaction speed with increased NP amount was observed over the whole range tested and the absorption at starting point increased alike, indicating a higher number of particles bound to the capture Ab. However, the initial absorption was very different between different conjugates. Owing to the design of the experiment, wells with and without capture Ab of the same NP would always be treated the same when washing with a multi-channel pipette. Thus, NP conjugates were treated with individual pipetting steps and were therefore susceptible to differences in redispersion of sedimented particles and damaging of the Ab- or NP-coating in the wells. To average out the errors, at least three individual replicate plates were measured in further immunoassays. Although it remained unclear, if even more particles could be bound to the microplate wells, a further increase of NP amount would have been a vast waste of precious material. Therefore, 50 µg NP conjugates were used for successive microplate assays.

4.3.4.2 Interday variability of peroxidase-like activity of selected rabbit IgG-conjugated MCM and HEN bound in an ELISA

As previous results indicated differences in NP binding or sedimentation between conjugates, immunoassays were performed for a total of five replicates to evaluate reproducibility.

The values of accelerated reaction speed (i.e., the difference between reaction with catalyst, e.g. with Ab-coating, subtracting the reaction speed with H₂O₂ alone, e.g. with BSA-coating only) varied quite substantially between replicate plates (differences between columns), but were fairly low and reproducible between replicate samples on a single plate (error bars for each column). (**Figure 44**) The variations in the microplate assays occurred for all of the conjugates, thus no preferential binding depending on NP type was observed and the deviations were considered statistical in nature. Further optimisation, as well as automation, of the multiple ELISA processing steps may be useful in decreasing this variability.

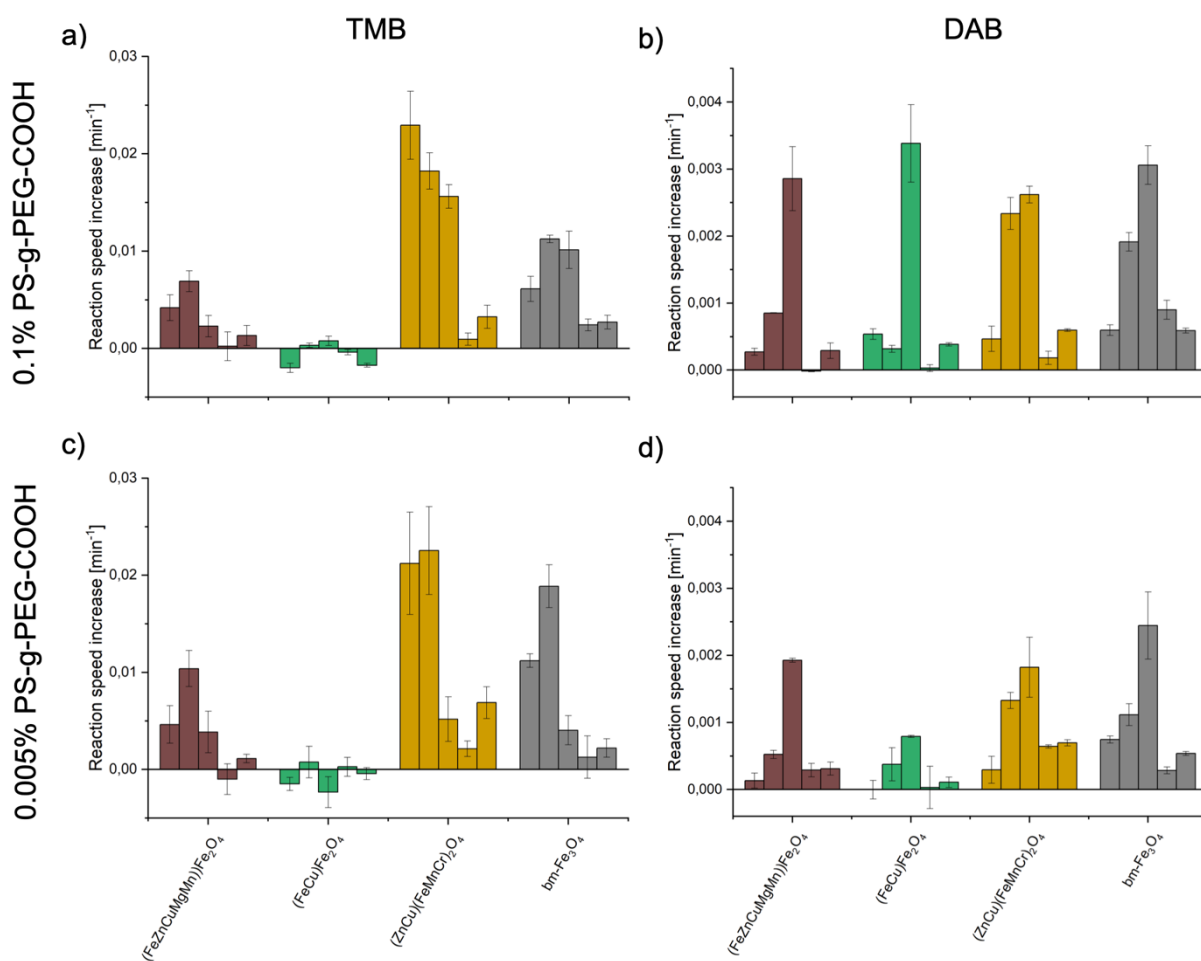


Figure 44: Reaction speed, e.g. slope of absorption versus time, for oxidation of TMB (a, c) and DAB (b, d) catalysed by IgG conjugates of NP dispersed in 0.1% PS-g-PEG-COOH (a, b) or 0.005% PS-g-PEG-COOH) (c, d). The wells were coated with anti-rabbit IgG and were incubated with 500 µg/mL rabbit IgG-NP conjugates. Reaction speed of wells coated with BSA only and incubated with 500 µg/mL rabbit IgG-NP conjugates was subtracted from the values. Each bar of one group shows an individual NP conjugate replicate on an individual plate. Values are mean values and standard deviation of three individual wells per plate.

4.3.4.3 Batch-to-batch-variation of selected HEN

In addition to understanding the variation between replicate ELISA assays, it was of interest to determine the batch-to-batch variation in HEN materials themselves. To this end, a second batch of $(\text{ZnCu})(\text{FeMnCr})_2\text{O}_4$ and $(\text{ZnCuMg})(\text{FeMnCr})_2\text{O}_4$ was synthesized. The NP were dispersed and conjugated according to the previously used procedures and investigated for catalytic activity. The results of the first batch of HEN could be reproduced very well with the second batch of NP. (**Figure 45**) The activity of $(\text{ZnCu})(\text{FeMnCr})_2\text{O}_4$, as well as the loss of activity following conjugation, was therefore interpreted as an intrinsic property of the material.

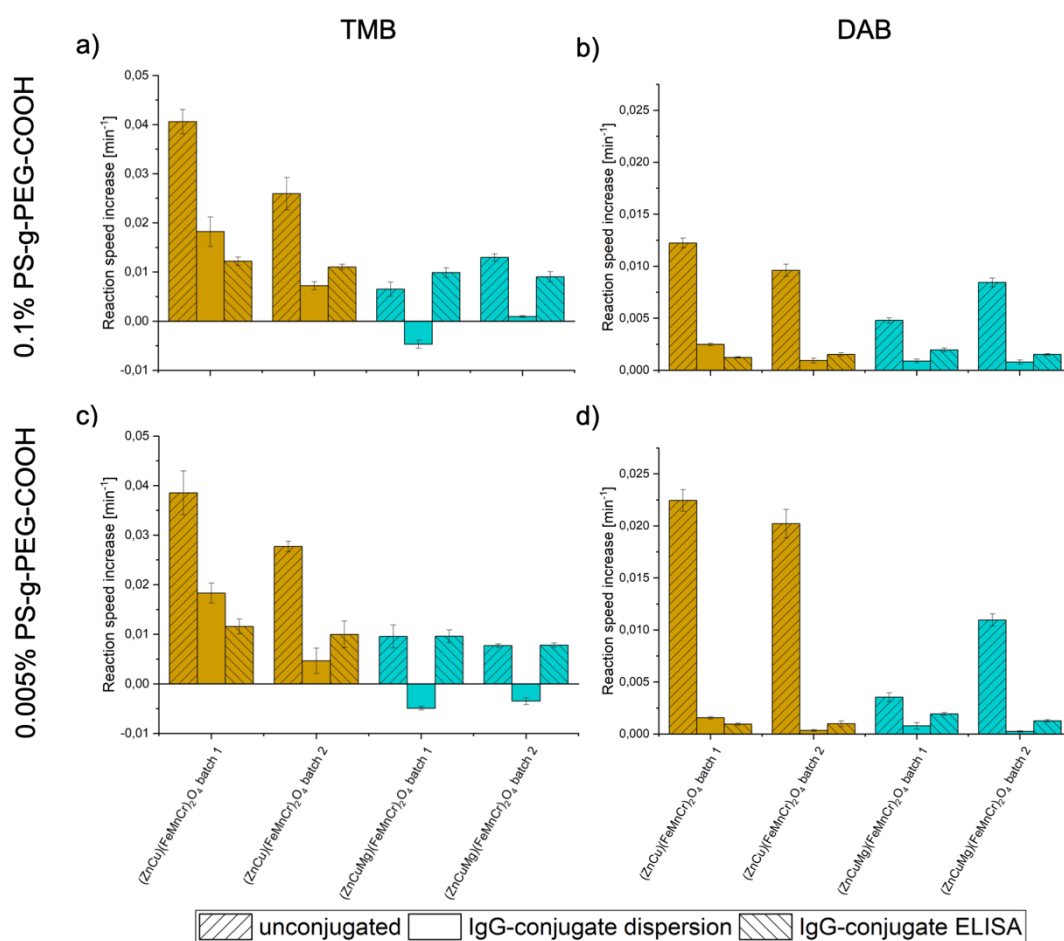


Figure 45: Batch-to-batch variation of selected HEN. Increase in speed of oxidation of TMB (a, c) or DAB (b, d) by H_2O_2 catalysed by HEN NP over oxidation with H_2O_2 only. HEN were dispersed in 0.1% (a, b) or 0.005% (c, d) PS-g-PEG-COOH. NP concentration was 40 $\mu\text{g}/\text{mL}$ for HEN or IgG-HEN-conjugate suspensions or 500 $\mu\text{g}/\text{mL}$ for IgG-HEN-conjugate suspensions in ELISA. Data shown are mean values and standard deviations of three replicate wells.

4.3.4.4 Troubleshooting: Understanding the catalytic activity at each processing step

It was observed that the catalytic activity of the dispersed samples was significantly higher than that of the IgG-conjugated samples, both in dispersion and in the ELISA. To better understand how each processing step influenced the catalytic activity of the samples, the average catalytic activity (i.e., the increase in reaction rate above the H_2O_2 control) was plotted for (1) the unconjugated dispersion, (2) a dispersion washed several times with TRIS buffer, (3) the IgG-conjugated dispersion, and (4) the IgG-conjugate in the ELISA. (**Figure 46**). Unexpectedly, the loss in activity occurred primarily during washing with a buffer (TRIS pH=7.4). It was hypothesised that soluble components could be removed from the MCM and HEN dispersions during the washing steps after conjugation. In case these components contributed to the catalysis, the loss of activity upon Ab coupling would be explained.

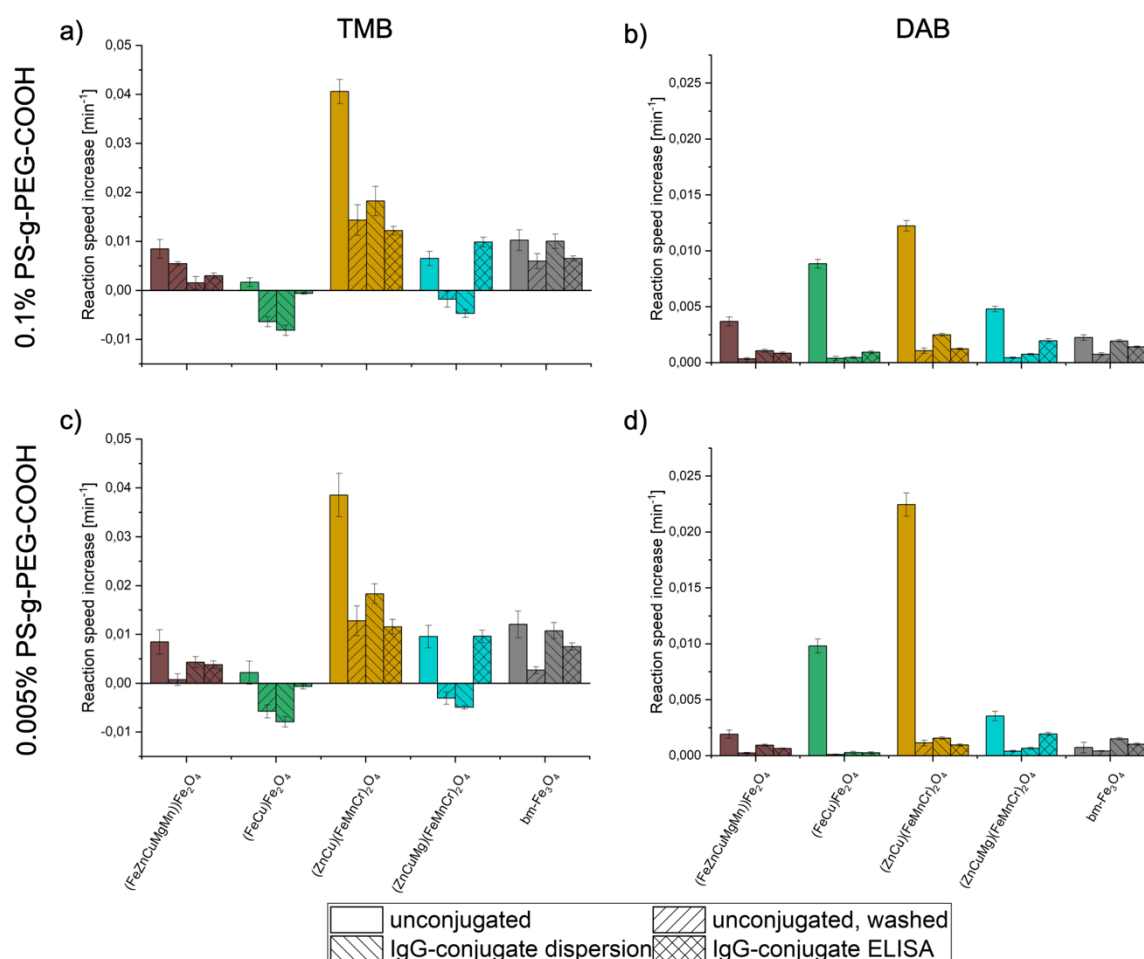


Figure 46: Increase in speed of oxidation of TMB (a, c) or DAB (b, d) by H_2O_2 catalysed by MCM and HEN NP over oxidation with H_2O_2 only. NP were dispersed in 0.1% (a, b) or 0.005% (c, d) PS-g-PEG-COOH. NP suspensions were used untreated, washed with 50 mM TRIS pH=7.4 containing 0.1% Tween 20, or conjugated to rabbit IgG. NP concentration was 40 $\mu\text{g/mL}$ for NP- or IgG-NP-conjugate suspensions or 500 $\mu\text{g/mL}$ for IgG-NP-conjugate suspensions in ELISA. Data shown are mean values and averaged standard deviations of five replicate plates with three replicate wells each, except for (ZnCuMg)(FeMnCr)₂O₄, which was three replicate wells on one plate.

As the washing steps included repeated sedimentation and redispersion, the NP size could be possibly altered, hence the active surface area reduced. However, DLS measurements showed no change in hydrodynamic diameter between crude and washed dispersions. **(Figure 47)** The results indicated that repeated washing with TRIS buffer had a profound effect on some materials, especially the HEN $(\text{ZnCu})(\text{FeMnCr})_2\text{O}_4$, but less of an effect on other materials, such as the Fe_3O_4 control. Thus, removal of soluble catalytically active components by the washing procedure was considered the most probable cause of activity loss. However, in the ELISA experiments the particles were not only washed after conjugation, but also several time throughout the immunoassay. Any retained activity was therefore believed to result from NP catalysis, rather than solutes. Furthermore, as the assay conditions were optimised to favor complete coverage of the capture Ab area in the wells, the surface available for catalysis was the same, independent on NP type. Therefore, the remaining activity in the ELISA represented the intrinsic catalytic activity of the NP material.

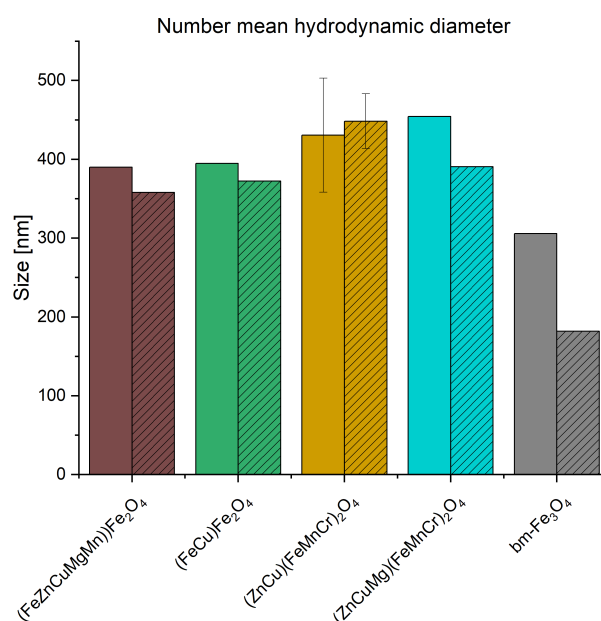


Figure 47: Hydrodynamic diameter of MCM and HEN dispersed in 0.05 M TRIS pH=7.4 before and after washing with 0.05 M TRIS pH=7.4 by repeated centrifugation and redispersion. Values of $(\text{ZnCu})(\text{FeMnCr})_2\text{O}_4$ are mean and standard deviation of 3 individual NP dispersions.

4.3.5 Effect of dispersant on catalytic activity

The buffer used for dispersion of the NP, TRIS, is known to form complexes with metal ions, including Zn(II), Cu(II) and Fe(III).^{239,240} Cu(II)-complexes, in turn, are known to catalyze oxidation of dyes by H₂O₂.²⁴¹ To assess the influence of TRIS on possible dissolution properties of HEN components and hence, the catalytic activity, NP suspensions were prepared in water, PBS and TRIS and then washed with the respective dispersant. No surfactant was used for dispersion to exclude any influence of such. Subsequent catalysis investigation of the crude and washed dispersions showed that washing led to reduced reaction speed for all NP and dispersants. (**Figure 48a and 48b**) However, the differences between crude and washed particles were only minor for water and PBS, and could be attributed to material loss during the washing procedure. In contrast, all NP, except bm-Fe₃O₄, dispersed in TRIS showed a major decrease in activity upon washing. The effect was most pronounced for DAB reactions, but also present for TMB. The supernatants of the washing procedure were collected and assessed for catalytic activity. For the DAB reaction with TRIS dispersions, the catalytic activity of supernatants and washed dispersions added up to the values of crude suspensions. (**Figure 48d**) For TMB, however, a correlation between supernatants and dispersions could not be found, but the catalytic activity of the supernatants was low, in general. It has to be noted, that the TMB substrate had a substantially lower pH (pH=4), compared to the DAB substrate (pH=7.4). Any catalytically active ions, that would have been complexed by TRIS could therefore precipitate in the TMB substrate, due to protonation of the TRIS amine group. The data clearly indicated that TRIS played a major role in reduction of activity upon washing. The experimental results suggested that catalytically active components were dissolved out of the solid NP material. However, the identification of the active species was out of scope of this thesis and is currently under investigation by other researchers in our group.

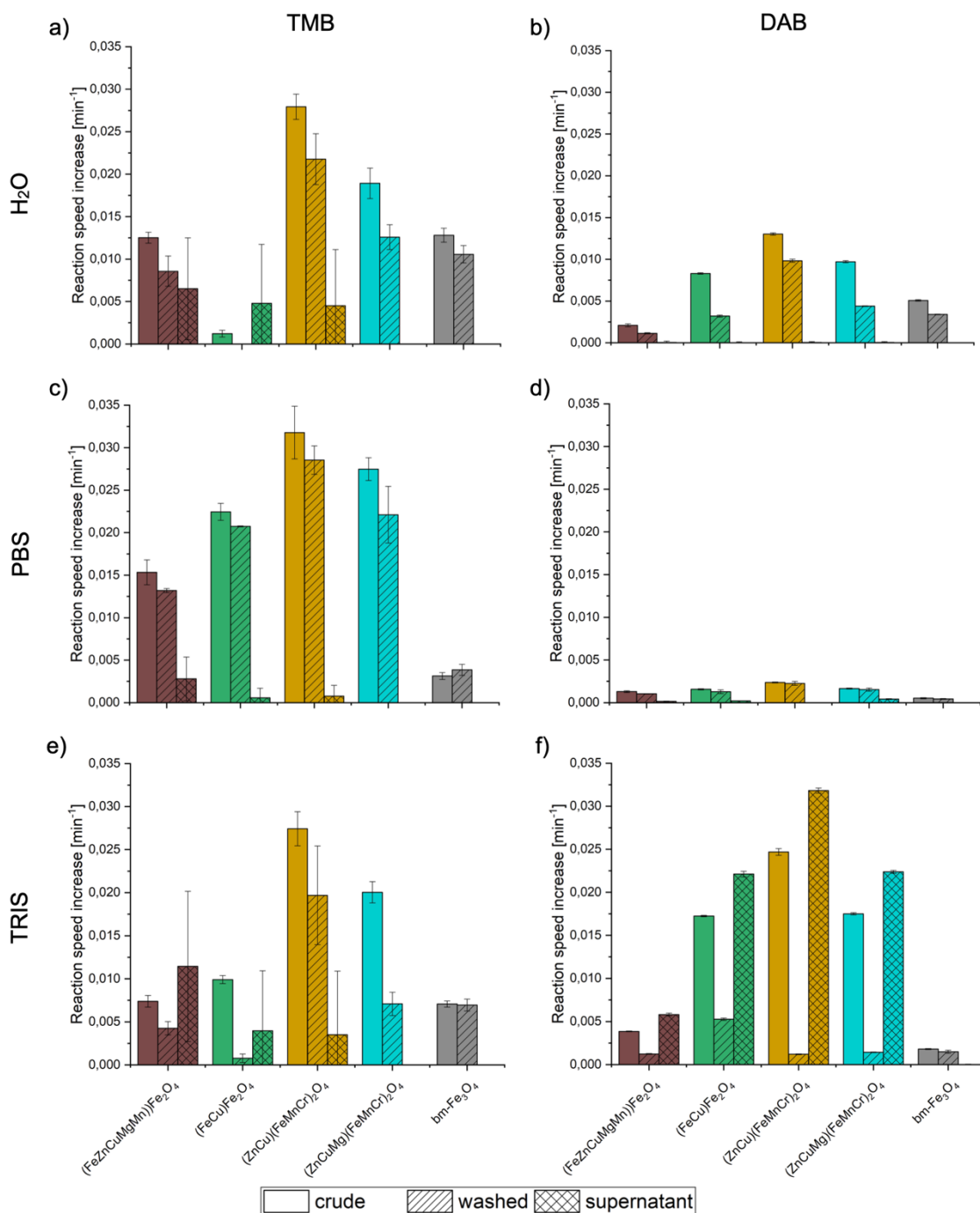


Figure 48: Increase in reaction speed of oxidation of TMB (a, c and e) or DAB (b, d and f) by H₂O₂ catalysed by MCM and HEN NP, dispersed in H₂O (a and b), PBS (c and d) or 50 mM TRIS pH=7.4 (e and f), over oxidation with H₂O₂ only. NP suspensions were used untreated, or washed with the respective dispersant three times by centrifugation sedimentation and redispersion. The supernatants were combined, freeze-dried and diluted with water to match the concentration in the untreated suspensions. NP concentration was 40 µg/mL. Values are mean and standard deviations of three wells.

4.4 Conclusion

Dispersions of MCM, HEN and bm-Fe₃O₄ were prepared with comparable hydrodynamic diameters between 200 and 300 nm in 0.1% Tween 20 or PS-g-PEG-COOH. The NP formed aggregates with diameters between 200 and 400 nm, when only 0.005% PS-g-PEG-COOH was used for dispersion. The catalytic activity of the NP was assessed by H₂O₂ oxidation of the dyes TMB and DAB. Distinct differences of reaction speed were observed for NP concentrations no less than 40 µg/mL and the reaction speeds were reproducible. When the small-molecule surfactant Tween 20 was used for dispersion, the reaction speeds were reduced, compared to the polymeric surfactant PS-g-PEG-COOH, which was used for further surface modification.

Depending on the dye, all of the HEN, as well as (FeCu)Fe₂O₄ showed increased catalytic activity superior to bm-Fe₃O₄ and were conjugated to rabbit IgG for subsequent immunoassays. A decrease in catalytic activity was observed for all materials upon conjugation. However, the effect was most pronounced for (ZnCu)(FeMnCr)₂O₄. The NP were subjected to an ELISA, where only (ZnCu)(FeMnCr)₂O₄ and (ZnCuMg)(FeMnCr)₂O₄ showed increased catalytic activity over bm-Fe₃O₄. Investigation on a second batch of NP excluded impurities or NP aggregation as cause for the severe drop of activity between unconjugated and conjugated (ZnCu)(FeMnCr)₂O₄. Instead, washing experiment in different dispersants revealed that the buffer used for dispersion, TRIS, led to dissolution of catalytically active components of the materials, that would be washed away during conjugates workup. Currently, the identification of the catalytically active species is under investigation by other researchers in our group.

Chapter 5

Summary and perspectives

5.1 Summary

The objective of this thesis was to evaluate new NP-based signal transducers for sensitivity-enhancement in lateral flow immunoassays (LFI). Two approaches, fluorescent LFI and dye-reaction enhanced LFI (eLFI) were considered as possible formats for improvement of sensitivity, compared to conventional colorimetric LFI.

In the second chapter, conjugated polymers (CP) were encapsulated in NP for use as fluorescent signal transducers and compared to commercial small-molecule fluorescent dye NP (PS-NP) and colorimetric detected colloidal gold (Au-NP). Two CP, PDOF and CN-PPV, were chosen to study the importance of brightness and background intensity on the signal-to-background ratio (SBR). PDOF had a high QY and extinction coefficient, thus high brightness. CN-PPV had a large Stokes shift, thus reduced background intensity. A blend of PDOF and CN-PPV was also investigated in an attempt to combine the advantages of both CP. Because of the hydrophobic nature of the CP, encapsulation in NP (Si-NP and Pdots) was necessary for use as signal transducer. The relation between CP loading dose and NP brightness was evaluated for Si-NP and Pdots. Theoretical considerations suggested that the brightness would increase proportionally to the loading dose for particles and the assumption was verified experimentally. While Si-NP could be loaded with up to 4% CP, Pdots had a maximum loading dose of 83%. Thus, the maximum brightness of Pdots was much higher compared to Si-NP. The Si-NP and Pdots with highest loading doses, as well as the reference NP, were conjugated to rabbit IgG as a model antibody (Ab) and subjected to an ELISA-like assay. It was shown that CP encapsulated in both Si-NP and Pdots had superior SBR, compared to PS-NP and Au-NP. For the same CP loading dose, e.g. same encapsulation system, CN-PPV NP had higher SBR compared to PDOF NP. With the same CP, Pdots had a higher SBR, compared to Si-NP. The highest SBR was observed for PDOF-CN-PPV-Pdots. In summary, the SBR in the ELISA-like assay was in the order of Au-NP < PS-NP < PDOF-Si-NP < CN-PPV-Si-NP < PDOF-Pdots < CN-PPV-Pdots < PDOF-CN-PPV-Pdots.

In the third chapter, the conjugated NP were used to optimise LFI parameters for each NP system. The investigated parameters were NC membrane material, test line concentration, fluorescent signal detector, running buffer composition and conjugate buffer composition. It was observed, that the fluorescent background signal of the NC membrane Immunopore RP was lower than of FF80HP. The SBR had a positive correlation with the test line capture Ab concentration up to 0.5 g/L, but decreased at higher values. The SBR was higher in general, when detected with a lateral flow reader, compared to a mobile phone camera.

All NP systems required surfactants in the running buffer for signal development. The SBR was observed to increase over a concentration range, depending on surfactant and NP type and plateaued for higher concentrations. Thus, a concentration of 8 mg/mL, a value well in the plateau region of all NP systems, was found suitable for the LFI. The highest SBR was observed when the running buffer contained a mixture of Triton X-100, PEG400 and BSA for Pdots or Tween 20 for Si-NP, PS-NP and Au-NP. The addition of surfactants was also necessary in the conjugate mixture to allow redispersion of Pdots and Si-NP from the conjugate pad. However, the SBR was found to have very high standard deviations after redispersion, owing to simplicity of available strip production methods. Thus, a dipstick LFI format without conjugate pad was found beneficial to reduce the error of SBR. Under the optimised conditions, the different rabbit IgG-conjugated NP were evaluated in dipstick LFI for sensitivity. It was observed, that the required NP mass for detection was about 100-fold lower for Pdots, compared to Si-NP, PS-NP and Au-NP, indicating superior sensitivity of Pdots. For Pdots, the SBR was in the order of PDOF < CN-PPV < PDOF-CN-PPV. To more accurately quantify the sensitivity, Ab for real analytes, namely anti-tetracycline-, anti-SAE- and anti-hFABP IgG were conjugated to Pdots and Au-NP. Unfortunately, no relation between analyte concentration and SBR at test line was found for any of the Pdot conjugates. In an ELISA-like assay with the Au-NP conjugates it was observed that only anti-hFABP IgG was able to bind the antigen. However, using the rabbit IgG model antigen system, it was possible to, for the first time ever, evaluate the sensitivity of CP-based signal transducers along Au-NP and a small-molecule fluorescent dye probe.

The main findings on CP-based fluorescent LFI were:

- 1) CP-based signal transducers may greatly enhance the sensitivity of LFI compared to small-molecule fluorescent dye-based NP and Au-NP
- 2) An increase of LFI sensitivity is observed for high CP loading doses (Pdots), but absent for low CP loading doses (Si-NP)
- 3) In Pdots, the large-Stokes shift CP (CN-PPV) shows higher SBR in LFI compared to the high-brightness CP (PDOF)
- 4) The highest SBR in LFI is observed for Pdots with a polymer blend of PDOF and CN-PPV

In the fourth chapter, new possible nanocatalysts for eLFI based on multi-cationic materials (MCM) and high-entropy nanomaterials (HEN) were evaluated for their catalytic activity. Fe₃O₄ NP, that have been published to work in eLFI, were used for comparison. The NP had comparable sizes, as determined by DLS.

A method for the quantification of the catalytic activity was established, that was based on the oxidation of the dyes TMB and DAB by H_2O_2 and quantification of the reaction products by absorption measurement. The method was found to be reproducible for all NP dispersions. A selection of the most active MCM and HEN, as well as the Fe_3O_4 control, was conjugated to rabbit IgG for use in immunoassays. Surprisingly, the HEN that showed more than twice the reaction speed of Fe_3O_4 in unconjugated dispersion ($(ZnCu)(FeMnCr)_2O_4$), had only slightly increased activity over the Fe_3O_4 control after conjugation. The conjugates were subjected to ELISA, where the decrease of catalytic activity of MCM and HEN, in comparison to unconjugated dispersions, was also observed. Further investigations could exclude aggregation and impurities as the cause of reduced activity of conjugated NP. In fact, the results suggested, that the buffer TRIS led to solubilisation of catalytically active species from the MCM and HEN surface. This phenomenon is currently being investigated in further detail in follow-on studies.

The main findings on MCM and HEN as catalysts for eLFI were:

- 1) The oxidation of TMB and DAB by H_2O_2 and quantification of the reaction products by absorption measurement is a reproducible method for evaluation of the catalytic activity of nanocatalysts
- 2) MCM and HEN show different catalytic activities, depending on the composition
- 3) Solubilised ions, that leak from the NP surface, may greatly influence the catalytic activity

5.2 Perspectives

CP have proven to be promising fluorescent dyes for signal transducers in LFI. In low-loading dose formulations however, they do not show advantages over commonly used LFI probes. Therefore, resources in product-oriented research can be spared, as these formulations do not need further investigation. It was shown that the type of CP has a high influence on the SBR in LFI. Thus, the assay sensitivity might be further improved by utilisation of different CP. The highest SBR was observed for Pdots with a polymer blend of PDOF and CN-PPV, using the FRET effect to combine the beneficial properties of both CP. However, optimisation of the ratio between FRET donor and FRET acceptor might further improve LFI sensitivity. The investigations on the model Ab system were only sufficient to qualitatively verify the superior sensitivity of Pdot-based LFI over colorimetric LFI. Thus, the system has to be transferred to a real application and the sensitivity has to be quantified based on analyte concentrations.

MCM and HEN were shown to be possible superior systems to Fe_3O_4 as nanocatalysts in immunoassays. The huge number of available combinations of elements in MCM and HEN allows for further optimisation of catalytic activity. The differences in activity of the materials evaluated in this thesis might help to build up a structure-activity relationship. However, the activity might be highly influenced by ions, that are leaking from the NP. For faster screening for active materials, new compounds should be subjected to all washing steps, that would occur during workup or application, prior to catalysis investigations. Finally, new active materials have to be applied to eLFI to quantify improvements in sensitivity.

The data generated by this research has provided detailed and fundamental guidance for the further development of more sensitive LFI in the future. With the advances in PCR technology and the decrease in price of alternative diagnostic methods, the relevance of LFI had appeared to be on the decline in recent years. With the widespread use of LFI diagnostics in the Sars-CoV-2 pandemic, it became clear that LFI have practical advantages in many diagnostic scenarios, especially as over-the-counter self-testing assays. This reinforces the need for future developments in this field to improve robustness and sensitivity. It has been exciting to play a role in this development process.

References

- (1) World Health Organization. *COVID-19 Weekly Epidemiological Update 29.12.2020* https://www.who.int/docs/default-source/coronaviruse/situation-reports/20201229-weekly-epi-update-con_20_cleared.pdf (accessed 27.01.2021)
- (2) Andrades Valtueña, A.; Mitnik, A.; Key, F. M.; Haak, W.; Allmäe, R.; Belinskij, A.; Daubaras, M.; Feldman, M.; Jankauskas, R.; Janković, I.; Massy, K.; Novak, M.; Pfrengle, S.; Reinhold, S.; Šlaus, M.; Spyrou, M. A.; Szécsényi-Nagy, A.; Törv, M.; Hansen, S.; Bos, K. I.; Stockhammer, P. W.; Herbig, A.; Krause, J. *Curr. Biol.* **2017**, *27* (23), 3683-3691.e8.
- (3) Baader, G.; Winau, R. *Die hippokratischen Epidemien*; Franz Steiner Verlag: Stuttgart, **1984**.
- (4) Huff, H. V. *Clin. Infect. Dis.* **2020**, No. Xx, 1–2. DOI: 10.1093/cid/ciaa1251
- (5) Pokhrel, P.; Hu, C.; Mao, H. *ACS Sensors* **2020**, *5* (8), 2283–2296.
- (6) Bukasov, R.; Dossym, D.; Filchakova, O. *Anal. Methods* **2021**, 34–55.
- (7) O'Farrell, B. In *Lateral Flow Immunoassay*; Humana Press: Totowa, NJ, **2009**; pp 1–33.
- (8) Angelini, D. J.; Biggs, T. D.; Prugh, A. M.; Smith, J. A.; Hanburger, J. A.; Llano, B.; Avelar, R.; Ellis, A.; Lusk, B.; Malik Naanaa, A.; Sisco, E.; Sekowski, J. W. *J. Forensic Sci.* **2021**, *66* (2), 758–765.
- (9) Rosenstein, R. W.; Bloomster, T. G. Solid phase assay employing capillary flow, US4855240, **1989**.
- (10) Berson, S. A.; Yalow, R. S. *J. Clin. Invest.* **1959**, *38* (11), 1996–2016.
- (11) Huet, J.; Sentenac, A.; Fromageot, P. *J. Biol. Chem.* **1982**, *257* (5), 2613–2618.
- (12) Hawkes, R.; Niday, E.; Gordon, J. *Anal. Biochem.* **1982**, *119* (1), 142–147.
- (13) Leuvering, J. H. W.; Thal, P. J. H. M.; van der Waart, M.; Schuurs, A. H. W. M. *J. Immunoassay* **1980**, *1* (1), 77–91.
- (14) Sajid, M.; Kawde, A.-N.; Daud, M. *J. Saudi Chem. Soc.* **2015**, *19* (6), 689–705.
- (15) European Commission. *Commission Recommendation of 18.11.2020 on the use of rapid antigen tests for the diagnosis of SARS-CoV-2 infection* https://ec.europa.eu/health/sites/health/files/preparedness_response/docs/sarscov2_rapidantigentests_recommendation_en.pdf (accessed 19.01.2021)

- (16) Scohy, A.; Anantharajah, A.; Bodéus, M.; Kabamba-Mukadi, B.; Verroken, A.; Rodriguez-Villalobos, H. *J. Clin. Virol.* **2020**, *129* (May), 104455.
- (17) Xiao, X.; Hu, S.; Lai, X.; Peng, J.; Lai, W. *Trends Food Sci. Technol.* **2021**, *111* (235), 68–88.
- (18) Lakowicz, J. R. *Principles of Fluorescence Spectroscopy*; Lakowicz, J. R., Ed.; Springer US: Boston, MA, **2006**.
- (19) Mathies, R. A.; Peck, K.; Stryer, L. *Anal. Chem.* **1990**, *62* (17), 1786–1791.
- (20) Stohrer, W.-D. In *Photochemie*; Wiley-VCH Verlag GmbH & Co. KGaA: Weinheim, FRG, **2005**; pp 5–81.
- (21) Brooks, D. E.; Devine, D. *Quantitative immunochromatographic assays*. US5753517A, **1998**.
- (22) Shenzhen Bioeasy Biotechnology Co. Ltd. *Point of care testing (POCT) - Bioeasy* http://en.bioeasy.com/?page_id=177 (accessed 19.01.2021).
- (23) Microprofit Biontech. *Shenzhen Microprofit Biotech Co., Ltd* <http://www.microprofit-bio.com/products/> (accessed 19.01.2021).
- (24) ellume. *Ellume | Consumer Products* <https://www.ellumehealth.com/products/consumer-products/> (accessed 19.01.2021).
- (25) Quidel Corporation. *Fluorescent Immunoassays | Direct & Indirect Fluorescent Antibody Tests* <https://www.quidel.com/immunoassays/fluorescent-immunoassays-fia> (accessed 19.01.2021).
- (26) Porte, L.; Legarraga, P.; Vollrath, V.; Aguilera, X.; Munita, J. M.; Araos, R.; Pizarro, G.; Vial, P.; Iruetagoiena, M.; Dittrich, S.; Weitzel, T. *Int. J. Infect. Dis.* **2020**, *99*, 328–333.
- (27) Saxman, A. M.; Liepins, R.; Aldissi, M. *Prog. Polym. Sci.* **1985**, *11* (1–2), 57–89.
- (28) Rasmussen, S. C. *ACS Symp. Ser.* **2011**, *1080*, 147–163.
- (29) Grady, L. J.; Polimeni, J. R. *Discrete Calculus*; Springer London: London, UK, **2010**.
- (30) Braeken, Y.; Cheruku, S.; Ethirajan, A.; Maes, W. *Materials (Basel)*. **2017**, *10* (12), 1–23.
- (31) Apaydin, D. H.; Tordin, E.; Portenkirchner, E.; Aufischer, G.; Schlager, S.; Weichselbaumer, M.; Oppelt, K.; Sariciftci, N. S. *ChemistrySelect* **2016**, *1* (6), 1156–1162.

- (32) Ocheje, M. U.; Charron, B. P.; Nyayachavadi, A.; Rondeau-Gagné, S. *Flex. Print. Electron.* **2017**, *2* (4), 43002.
- (33) Guo, X.; Baumgarten, M.; Müllen, K. *Prog. Polym. Sci.* **2013**, *38* (12), 1832–1908.
- (34) Xie, J.; Zhao, C.; Lin, Z.; Gu, P.; Zhang, Q. *Chem. - An Asian J.* **2016**, *11* (10), 1489–1511.
- (35) Melling, D.; Martinez, J. G.; Jager, E. W. H. *Adv. Mater.* **2019**, *31* (22), 1808210.
- (36) Dararatana, N.; Seidi, F.; Crespy, D. *ACS Appl. Mater. Interfaces* **2018**, *10* (24), 20876–20883.
- (37) Dai, C.; Liu, B. *Energy Environ. Sci.* **2020**, *13* (1), 24–52.
- (38) Baek, P.; Voorhaar, L.; Barker, D.; Travas-Sejdic, J. *Acc. Chem. Res.* **2018**, *51* (7), 1581–1589.
- (39) Abelha, T. F.; Dreiss, C. A.; Green, M. A.; Dailey, L. A. *J. Mater. Chem. B* **2020**, *8* (4), 592–606.
- (40) Li, K.; Liu, B. *J. Mater. Chem.* **2012**, *22* (4), 1257–1264.
- (41) Fang, C.; Chou, C.; Yang, Y.; Wei-Kai, T.; Wang, Y.; Chan, Y.-H. *Anal. Chem.* **2018**, *90* (3), 2134–2140.
- (42) Andreeva, I. P.; Grigorenko, V. G.; Egorov, A. M.; Osipov, A. P. *Anal. Lett.* **2016**, *49* (4), 579–588.
- (43) Yang, Y.-Q.; Yang, Y.; Liu, M.; Chan, Y. *Anal. Chem.* **2020**, *92* (1), 1493–1501.
- (44) Mulvaney, S. P.; Kidwell, D. A.; Lanese, J. N.; Lopez, R. P.; Sumera, M. E.; Wei, E. *Sens. Bio-Sensing Res.* **2020**, *30* (August), 100390.
- (45) Cho, J. H.; Paek, E. H.; Cho, I. I. H.; Paek, S. H. *Anal. Chem.* **2005**, *77* (13), 4091–4097.
- (46) Mao, X.; Ma, Y.; Zhang, A.; Zhang, L.; Zeng, L.; Liu, G. *Anal. Chem.* **2009**, *81* (4), 1660–1668.
- (47) He, Y.; Zhang, S.; Zhang, X.; Baloda, M.; Gurung, A. S.; Xu, H.; Zhang, X.; Liu, G. *Biosens. Bioelectron.* **2011**, *26* (5), 2018–2024.
- (48) Loynachan, C. N.; Thomas, M. R.; Gray, E. R.; Richards, D. A.; Kim, J.; Miller, B. S.; Brookes, J. C.; Agarwal, S.; Chudasama, V.; McKendry, R. A.; Stevens, M. M. *ACS Nano* **2018**, *12* (1), 279–288.

- (49) Wang, Q.; Wei, H.; Zhang, Z.; Wang, E.; Dong, S. *TrAC - Trends Anal. Chem.* **2018**, *105*, 218–224.
- (50) Chen, W.; Huang, Z.; Hu, S.; Peng, J.; Liu, D.; Xiong, Y.; Xu, H.; Wei, H.; Lai, W. *J. Dairy Sci.* **2019**, *102* (3), 1887–1900.
- (51) Huang, Y.; Ren, J.; Qu, X. *Chem. Rev.* **2019**, *119* (6), 4357–4412.
- (52) Panferov, V. G.; Safenkova, I. V.; Zherdev, A. V.; Dzantiev, B. B. *Talanta* **2021**, *225* (December 2020), 121961.
- (53) Kim, M. S.; Kweon, S. H.; Cho, S.; An, S. S. A.; Kim, M. II; Doh, J.; Lee, J. *ACS Appl. Mater. Interfaces* **2017**, *9* (40), 35133–35140.
- (54) Jiang, T.; Song, Y.; Wei, T.; Li, H.; Du, D.; Zhu, M. J.; Lin, Y. *Biosens. Bioelectron.* **2016**, *77*, 687–694.
- (55) Han, J.; Zhang, L.; Hu, L.; Xing, K.; Lu, X.; Huang, Y.; Zhang, J.; Lai, W.; Chen, T. *J. Dairy Sci.* **2018**, *101* (7), 5770–5779.
- (56) Cheng, N.; Shi, Q.; Zhu, C.; Li, S.; Lin, Y.; Du, D. *Biosens. Bioelectron.* **2019**, *142* (March), 1–7.
- (57) Song, X.; Knotts, M. *Anal. Chim. Acta* **2008**, *626* (2), 186–192.
- (58) Croce, A. C.; Bottiroli, G. *Eur. J. Histochem.* **2014**, *58* (4), 320–337.
- (59) Kuznetsov, A.; Frorip, A.; Maiste, A.; Ots-Rosenberg, M.; Sünter, A. *J. Innov. Opt. Health Sci.* **2015**, *8* (3), 1–9.
- (60) Klingstedt, T.; Nilsson, K. P. R. *Biochim. Biophys. Acta - Gen. Subj.* **2011**, *1810* (3), 286–296.
- (61) Banerjee, R.; Jaiswal, A. *Analyst* **2018**, *143* (9), 1970–1996.
- (62) Huang, X.; Aguilar, Z. P.; Xu, H.; Lai, W.; Xiong, Y. *Biosens. Bioelectron.* **2016**, *75*, 166–180.
- (63) Huang, X.; Aguilar, Z. P.; Li, H.; Lai, W.; Wei, H.; Xu, H.; Xiong, Y. *Anal. Chem.* **2013**, *85* (10), 5120–5128.
- (64) Mak, W. C.; Beni, V.; Turner, A. P. F. *TrAC Trends Anal. Chem.* **2016**, *79*, 297–305.
- (65) Ryu, Y.; Jin, Z.; Kang, M. S.; Kim, H.-S. *BioChip J.* **2011**, *5* (3), 193–198.
- (66) Brunetti, V.; Chibli, H.; Fiammengo, R.; Galeone, A.; Malvindi, M. A.; Vecchio, G.;

- Cingolani, R.; Nadeau, J. L.; Pompa, P. P. *Nanoscale* **2013**, 5 (1), 307–317.
- (67) Behnke, T.; Würth, C.; Hoffmann, K.; Hübner, M.; Panne, U.; Resch-Genger, U. *J. Fluoresc.* **2011**, 21 (3), 937–944.
- (68) Feng, L.; Zhu, C.; Yuan, H.; Liu, L.; Lv, F.; Wang, S. *Chem. Soc. Rev.* **2013**, 42 (16), 6620–6633.
- (69) Elmowafy, E. M.; Tiboni, M.; Soliman, M. E. *Biocompatibility, biodegradation and biomedical applications of poly(lactic acid)/poly(lactic-co-glycolic acid) micro and nanoparticles*; Springer Singapore, **2019**; Vol. 49.
- (70) Neumann, P. R.; Crossley, D. L.; Turner, M.; Ingleson, M.; Green, M.; Rao, J.; Dailey, L. A. *ACS Appl. Mater. Interfaces* **2019**, 11 (50), 46525–46535.
- (71) Tan, H.; Zhang, Y.; Wang, M.; Zhang, Z.; Zhang, X.; Yong, A. M.; Wong, S. Y.; Chang, A. Y. chi; Chen, Z. K.; Li, X.; Choolani, M.; Wang, J. *Biomaterials* **2012**, 33 (1), 237–246.
- (72) Reisch, A.; Klymchenko, A. S. *Small* **2016**, 12 (15), 1968–1992.
- (73) Hlaing, M.; Gebear-Eigzabher, B.; Roa, A.; Marcano, A.; Radu, D.; Lai, C. Y. *Opt. Mater. (Amst)*. **2016**, 58, 439–444.
- (74) Lavis, L. D.; Raines, R. T. *ACS Chem. Biol.* **2008**, 3 (3), 142–155.
- (75) Safenkova, I.; Zherdev, A.; Dzantiev, B. *Anal. Bioanal. Chem.* **2012**, 403 (6), 1595–1605.
- (76) Aveyard, J.; Mehrabi, M.; Cossins, A.; Braven, H.; Wilson, R. *Chem. Commun.* **2007**, No. 41, 4251–4253.
- (77) Posthuma-Trumpie, G. A.; Korf, J.; Van Amerongen, A. *Anal. Bioanal. Chem.* **2009**, 393 (2), 569–582.
- (78) Yan, J.; Liu, Y.; Wang, Y.; Xu, X.; Lu, Y.; Pan, Y.; Guo, F.; Shi, D. *Sensors Actuators, B Chem.* **2014**, 197, 129–136.
- (79) Kumar, A.; Dixit, C. K. In *Advances in Nanomedicine for the Delivery of Therapeutic Nucleic Acids*; Elsevier, **2017**; pp 43–58.
- (80) Berg, J. M.; Romoser, A.; Banerjee, N.; Zebda, R.; Sayes, C. M. *Nanotoxicology* **2009**, 3 (4), 276–283.

- (81) Guerrini, L.; Alvarez-Puebla, R. A.; Pazos-Perez, N. *Materials (Basel)*. **2018**, *11* (7), 1–28.
- (82) Tam, J. O.; de Puig, H.; Yen, C.; Bosch, I.; Gómez-Márquez, J.; Clavet, C.; Hamad-Schifferli, K.; Gehrke, L. *J. Immunoass. Immunochem.* **2017**, *38* (4), 355–377.
- (83) Walkey, C. D.; Olsen, J. B.; Guo, H.; Emili, A.; Chan, W. C. W. *J. Am. Chem. Soc.* **2012**, *134* (4), 2139–2147.
- (84) Sperling, R. A.; Parak, W. J. *Philos. Trans. R. Soc. A Math. Phys. Eng. Sci.* **2010**, *368* (1915), 1333–1383.
- (85) Werengowska-Ciećwierz, K.; Wiśniewski, M.; Terzyk, A. P.; Furmaniak, S. *Adv. Condens. Matter Phys.* **2015**, *2015*, 1-27.
- (86) Ali, M. A.; Islam, M. T. In *Surface Modification of Nanoparticles for Targeted Drug Delivery*; Springer International Publishing: Cham, **2019**; pp 405–430.
- (87) Saha, B.; Songe, P.; Evers, T. H.; Prins, M. W. J. *J. Analyst* **2017**, *142* (22), 4247–4256.
- (88) Zhang, B.; Yu, J.; Liu, C.; Wang, J.; Han, H.; Zhang, P.; Shi, D. *RSC Adv.* **2016**, *6* (55), 50119–50127.
- (89) Acchione, M.; Kwon, H.; Jochheim, C. M.; Atkins, W. M. *MAbs* **2012**, *4* (3), 362–372.
- (90) Clogston, J. D.; Patri, A. K. In *Characterization of Nanoparticles Intended for Drug Delivery*; Humana Press: Totowa, NJ, **2011**; pp 63–70.
- (91) Wiriyachaiorn, S.; Howarth, P. H.; Bruce, K. D.; Dailey, L. A. *Diagn. Microbiol. Infect. Dis.* **2013**, *75* (1), 28–36.
- (92) Lee, L.; Nordman, E.; Johnson, M.; Oldham, M. *Biosensors* **2013**, *3* (4), 360–373.
- (93) Glazer, A. N. In *Methods in Enzymology*; **1990**; Vol. 186, pp 161–168.
- (94) Iwai, K.; Uesugi, Y.; Sakabe, T.; Hazama, C.; Takemura, F. *Polym. J.* **1991**, *23* (6), 757–763.
- (95) Crosby, G. A.; Demas, J. N. *J. Am. Chem. Soc.* **1971**, *93* (12), 2841–2847.
- (96) Lou, D.; Fan, L.; Ji, Y.; Gu, N.; Zhang, Y. *Anal. Methods* **2019**, *11* (28), 3506–3513.
- (97) Mujumdar, R. B.; Ernst, L. A.; Mujumdar, S. R.; Lewis, C. J. *Bioconjug. Chem.* **1993**, *4* (2), 105–111.
- (98) Cai, Y.; Kang, K.; Li, Q.; Wang, Y.; He, X. *Molecules* **2018**, *23* (5), 1102.

- (99) Martinez, V.; Henary, M. *Chem. - A Eur. J.* **2016**, *22* (39), 13764–13782.
- (100) Ibnaouf, K. H. *Synth. Met.* **2015**, *209*, 534–543.
- (101) Samuel, I. D. W.; Rumbles, G.; Collison, C. J. *Phys. Rev. B* **1995**, *52* (16), R11573–R11576.
- (102) Samuel, I. D. W.; Rumbles, G.; Collison, C. J.; Moratti, S. C.; Holmes, A. B. *Chem. Phys.* **1998**, *227* (1–2), 75–82.
- (103) Nagarajan, R. *Colloids Surfaces B Biointerfaces* **1999**, *16* (1–4), 55–72.
- (104) Han, S.; Kim, C.; Kwon, D. *Polym. Degrad. Stab.* **1995**, *47*, 203–208.
- (105) Guan, B.; Ali, A.; Peng, H.; Hu, W.; Markely, L. R.; Estes, S.; Prajapati, S. *Anal. Methods* **2016**, *8* (13), 2812–2819.
- (106) Tan, H.; Xue, J. M.; Shuter, B.; Li, X.; Wang, J. *Adv. Funct. Mater.* **2010**, *20* (5), 722–731.
- (107) Bourke, S.; Urbano, L.; Olona, A.; Valderrama, F.; Dailey, L. A.; Green, M. A. In *Reporters, Markers, Dyes, Nanoparticles, and Molecular Probes for Biomedical Applications IX*; **2017**; Vol. 10079, p 100790A. DOI: 10.1117/12.2252035
- (108) Desai, P. .; Jain, N. .; Sharma, R. .; Bahadur, P. *Colloids Surfaces A Physicochem. Eng. Asp.* **2001**, *178* (1–3), 57–69.
- (109) Wang, H.; Williams, G. R.; Wu, J.; Wu, J.; Niu, S.; Xie, X.; Li, S.; Zhu, L.-M. *Int. J. Pharm.* **2019**, *559*, 289–298.
- (110) Lenaerts, V.; Triqueneaux, C.; Quartern, M.; Rieg-Falson, F.; Couvreur, P. *Int. J. Pharm.* **1987**, *39* (1–2), 121–127.
- (111) You, Z.; Nirmalanathan-Budau, N.; Resch-Genger, U.; Panne, U.; Weidner, S. M. *J. Chromatogr. A* **2020**, *1626*, 461392.
- (112) Eastman, J. In *Colloid Science*; Blackwell Publishing Ltd.: Oxford, UK, **1992**; Vol. 41, pp 36–49.
- (113) Ulusoy, M.; Jonczyk, R.; Walter, J. G.; Springer, S.; Lavrentieva, A.; Stahl, F.; Green, M.; Scheper, T. *Bioconjug. Chem.* **2016**, *27* (2), 414–426.
- (114) Koralli, P.; D. Nega, A.; Vagiaki, L. E.; Pavlou, A.; Siskos, M. G.; Dimitrakopoulou-Strauss, A.; Gregoriou, V. G.; Chochos, C. L. *Mater. Chem. Front.* **2020**, *4* (8), 2357–2369.

- (115) Xing, C.; Liu, L.; Song, S.; Feng, M.; Kuang, H.; Xu, C. *Biosens. Bioelectron.* **2015**, *66*, 445–453.
- (116) Hsieh, H. V.; Dantzler, J. L.; Weigl, B. H. *Diagnostics* **2017**, *7* (2), 29.
- (117) Lee, J.-Y.; Kim, Y. A.; Kim, M. Y.; Lee, Y. T.; Hammock, B. D.; Lee, H.-S. *Anal. Chim. Acta* **2012**, *757*, 69–74.
- (118) Chen, C.; Wu, J. *Sensors (Switzerland)* **2012**, *12* (9), 11684–11696.
- (119) Shah, K. G.; Yager, P. *Anal. Chem.* **2017**, *89* (22), 12023–12029.
- (120) Parolo, C.; Medina-Sánchez, M.; De La Escosura-Muñiz, A.; Merkoçi, A. *Lab Chip* **2013**, *13* (3), 386–390.
- (121) Zadehkafi, A.; Siavashi, M.; Asiaei, S.; Bidgoli, M. R. *J. Chromatogr. B Anal. Technol. Biomed. Life Sci.* **2019**, *1110–1111* (August 2018), 1–8.
- (122) Asiaei, S.; Bidgoli, M. R.; ZadehKafi, A.; Saderi, N.; Siavashi, M. *Clin. Chim. Acta* **2018**, *487* (April), 210–215.
- (123) Hong, S. Y.; Park, Y. M.; Jang, Y. H.; Min, B.-H.; Yoon, H. C. *BioChip J.* **2012**, *6* (3), 213–220.
- (124) Bai, Y.; Tian, C.; Wei, X.; Wang, Y.; Wang, D.; Shi, X. *RSC Adv.* **2012**, *2* (5), 1778.
- (125) Juntunen, E.; Myryläinen, T.; Salminen, T.; Soukka, T.; Pettersson, K. *Anal. Biochem.* **2012**, *428* (1), 31–38.
- (126) Xie, Q.-Y.; Wu, Y.-H.; Xiong, Q.-R.; Xu, H.-Y.; Xiong, Y.-H.; Liu, K.; Jin, Y.; Lai, W.-H. *Biosens. Bioelectron.* **2014**, *54*, 262–265.
- (127) Zhang, X.; Wu, C.; Wen, K.; Jiang, H.; Shen, J.; Zhang, S.; Wang, Z. *Molecules* **2015**, *21* (1), 27.
- (128) Cheng, S.; Yang, Y.; Ni, X.; Peng, J.; Lai, W. *Food Agric. Immunol.* **2017**, *28* (6), 1017–1028.
- (129) Fan, R.; Zhang, W.; Jin, Y.; Zhao, R.; Yang, C.; Chen, Q.; He, L.; Chen, Y. *Microchim. Acta* **2020**, *187* (6), 1–9.
- (130) Tan, G.; Zhao, Y.; Wang, M.; Chen, X.; Wang, B.; Li, Q. X. *Food Chem.* **2020**, *311* (June 2019), 126055.
- (131) Leonardi, G. P.; Wilson, A. M.; Zuretti, A. R. *J. Virol. Methods* **2013**, *189* (2), 379–382.

- (132) Venkatraman, V.; Steckl, A. J. *Biosens. Bioelectron.* **2015**, *74*, 150–155.
- (133) Song, C.; Zhi, A.; Liu, Q.; Yang, J.; Jia, G.; Shervin, J.; Tang, L.; Hu, X.; Deng, R.; Xu, C.; Zhang, G. *Biosens. Bioelectron.* **2013**, *50*, 62–65.
- (134) Chen, R.; Li, H.; Zhang, H.; Zhang, S.; Shi, W.; Shen, J.; Wang, Z. *Anal. Bioanal. Chem.* **2013**, *405* (21), 6783–6789.
- (135) Ryu, J. H.; Kwon, M.; Moon, J.-D.; Hwang, M.-W.; Lee, J.-M.; Park, K.-H.; Yun, S. J.; Bae, H. J.; Choi, A.; Lee, H.; Jung, B.; Jeong, J.; Han, K.; Kim, Y.; Oh, E.-J. *Ann. Lab. Med.* **2018**, *38* (6), 578–584.
- (136) Wu, M.; Zhang, X.; Wu, R.; Wang, G.; Li, J.; Chai, Y.; Shen, H.; Li, L. S. *Anal. Lett.* **2020**, *53* (11), 1757–1773.
- (137) Wang, J.; Wang, Q.; Zheng, Y.; Peng, T.; Yao, K.; Xie, S.; Zhang, X.; Xia, X.; Li, J.; Jiang, H. *Food Agric. Immunol.* **2018**, *29* (1), 56–66.
- (138) Rundström, G.; Jonsson, A.; Mårtensson, O.; Mendel-Hartvig, I.; Venge, P. *Clin. Chem.* **2007**, *53* (2), 342–348.
- (139) Zhang, Z.; Wang, D.; Li, J.; Zhang, Q.; Li, P. *Anal. Methods* **2015**, *7* (6), 2822–2829.
- (140) Shao, X. Y.; Wang, C. R.; Xie, C. M.; Wang, X. G.; Liang, R. L.; Xu, W. W. *Sensors (Switzerland)* **2017**, *17* (3).
- (141) Huang, D.; Ying, H.; Jiang, D.; Liu, F.; Tian, Y.; Du, C.; Zhang, L.; Pu, X. *Anal. Biochem.* **2020**, *588* (August 2019), 113468.
- (142) Chen, Y.; Chen, Q.; Han, M.; Liu, J.; Zhao, P.; He, L.; Zhang, Y.; Niu, Y.; Yang, W.; Zhang, L. *Biosens. Bioelectron.* **2016**, *79*, 430–434.
- (143) Rajendran, V. K.; Bakthavathsalam, P.; Jaffar Ali, B. M. *Microchim. Acta* **2014**, *181* (15–16), 1815–1821.
- (144) You, M.; Lin, M.; Gong, Y.; Wang, S.; Li, A.; Ji, L.; Zhao, H.; Ling, K.; Wen, T.; Huang, Y.; Gao, D.; Ma, Q.; Wang, T.; Ma, A.; Li, X.; Xu, F. *ACS Nano* **2017**, *11* (6), 6261–6270.
- (145) Rong, Z.; Wang, Q.; Sun, N.; Jia, X.; Wang, K.; Xiao, R.; Wang, S. *Anal. Chim. Acta* **2019**, *1055*, 140–147.
- (146) Jin, B.; Yang, Y.; He, R.; Park, Y. II; Lee, A.; Bai, D.; Li, F.; Lu, T. J.; Xu, F.; Lin, M. *Sensors Actuators B Chem.* **2018**, *276*, 48–56.

- (147) Hou, Y.; Wang, K.; Xiao, K.; Qin, W.; Lu, W.; Tao, W.; Cui, D. *Nanoscale Res. Lett.* **2017**, *12* (1), 291.
- (148) Venkatraman, V.; Liedert, R.; Kozak, K.; Steckl, A. J. *Flex. Print. Electron.* **2016**, *1* (4), 044001.
- (149) Shah, K. G.; Singh, V.; Kauffman, P. C.; Abe, K.; Yager, P. *Anal. Chem.* **2018**, *90* (11), 6967–6974.
- (150) Food and Drug Administration. *In Vitro Diagnostics EUAs* <https://www.fda.gov/medical-devices/coronavirus-disease-2019-covid-19-emergency-use-authorizations-medical-devices/vitro-diagnostics-euas> (accessed 19.01.2020).
- (151) Ellume. *Ellume's COVID-19 Home Test shows 96% accuracy in multi-site US clinical study* <https://www.ellumehealth.com/2020/12/10/ellumes-covid-19-home-test-shows-96-accuracy-in-multi-site-us-clinical-study/> (accessed 19.01.2020).
- (152) Zherdev, A. V.; Dzantiev, B. B. In *Rapid Test - Advances in Design, Format and Diagnostic Applications*; InTech, **2018**; pp 9–44. DOI: 10.5772/intechopen.76926
- (153) Pan, R.; Jiang, Y.; Sun, L.; Wang, R.; Zhuang, K.; Zhao, Y.; Wang, H.; Ali, M. A.; Xu, H.; Man, C. *J. Dairy Sci.* **2018**, *101* (5), 3835–3843.
- (154) Srisrattakarn, A.; Tippayawat, P.; Chanawong, A.; Tavichakorntrakool, R.; Daduang, J.; Wonglakorn, L.; Lulitanond, A. *Diagnostics* **2020**, *10* (10), 794.
- (155) Tisone, T. C.; O'Farrell, B. In *Lateral Flow Immunoassay*; Humana Press: Totowa, NJ, **2009**; pp 131–156.
- (156) Sarmah, A. K.; Meyer, M. T.; Boxall, A. B. A. *Chemosphere* **2006**, *65* (5), 725–759.
- (157) PerkinElmer. *Dairy Testing* https://www.perkinelmer.com/lab-solutions/resources/docs/BRO_Dairy-Testing.pdf (accessed 12.04.2021)
- (158) Heidinger, J. C.; Winter, C. K.; Cullor, J. S. *J. Food Prot.* **2009**, *72* (8), 1641–1653.
- (159) Furuhashi, M.; Hotamisligil, G. S. *Nat. Rev. Drug Discov.* **2008**, *7* (6), 489–503.
- (160) Innova Biosciences. *A Guide to Lateral Flow Immunoassays* https://fnkprddata.blob.core.windows.net/domestic/download/pdf/IBS_A_guide_to_lateral_flow_immunoassays.pdf (accessed 19.01.2021)
- (161) Atkins, P. W.; De Paula, J. *Physikalische Chemie*, 5th ed.; Wiley-VCH: Weinheim, **2020**.

- (162) Mortimer, C. E.; Müller, U. *Chemie: Das Basiswissen der Chemie*; Georg Thieme Verlag: Stuttgart, **2020**; Vol. 5.
- (163) Bugg, T. In *Introduction to Enzyme and Coenzyme Chemistry*; John Wiley & Sons, Ltd: Chichester, UK, **2012**; pp 26–49.
- (164) Lin, Y.; Ren, J.; Qu, X. *Acc. Chem. Res.* **2014**, *47* (4), 1097–1105.
- (165) Cramer, F. *Chem. Ber.* **2006**, *86* (12), 1576–1581.
- (166) Klotz, I. M.; Royer, G. P.; Scarpa, I. S. *Proc. Natl. Acad. Sci.* **1971**, *68* (2), 263–264.
- (167) Manea, F.; Houillon, F. B.; Pasquato, L.; Scrimin, P. *Angew. Chemie Int. Ed.* **2004**, *43* (45), 6165–6169.
- (168) Tokuyama, H.; Yamago, S.; Nakamura, E.; Shiraki, T.; Sugiura, Y. *J. Am. Chem. Soc.* **1993**, *115* (17), 7918–7919.
- (169) Zhang, R.; Fan, K.; Yan, X. *Sci. China Life Sci.* **2020**, *63* (8), 1183–1200.
- (170) Wei, H.; Wang, E. *Chem. Soc. Rev.* **2013**, *42* (14), 6060–6093.
- (171) Zhang, J.; Liu, J. *Nanoscale* **2020**, *12* (5), 2914–2923.
- (172) Gao, L.; Zhuang, J.; Nie, L.; Zhang, J.; Zhang, Y.; Gu, N.; Wang, T.; Feng, J.; Yang, D.; Perrett, S.; Yan, X. *Nat. Nanotechnol.* **2007**, *2* (9), 577–583.
- (173) Comotti, M.; Della Pina, C.; Matarrese, R.; Rossi, M. *Angew. Chemie Int. Ed.* **2004**, *43* (43), 5812–5815.
- (174) Korsvik, C.; Patil, S.; Seal, S.; Self, W. T. *Chem. Commun.* **2007**, No. 10, 1056.
- (175) Gumpelmayer, M.; Nguyen, M.; Molnár, G.; Bousseksou, A.; Meunier, B.; Robert, A. *Angew. Chemie Int. Ed.* **2018**, *57* (45), 14758–14763.
- (176) Maldonado, A. C. M.; Winkler, E. L.; Raineri, M.; Toro Córdova, A.; Rodríguez, L. M.; Troiani, H. E.; Piscioti, M. L. M.; Mansilla, M. V.; Tobia, D.; Nadal, M. S.; Torres, T. E.; De Biasi, E.; Ramos, C. A.; Goya, G. F.; Zysler, R. D.; Lima, E. *J. Phys. Chem. C* **2019**, *123* (33), 20617–20627.
- (177) Meunier, B.; Robert, A. *J. Phys. Chem. C* **2019**, *123* (46), 28513–28514.
- (178) Maldonado, A. C. M.; Winkler, E. L.; Raineri, M.; Toro Córdova, A.; Rodríguez, L. M.; Troiani, H. E.; Piscioti, M. L. M.; Mansilla, M. V.; Tobia, D.; Nadal, M. S.; Torres, T. E.; De Biasi, E.; Ramos, C. A.; Goya, G. F.; Zysler, R. D.; Lima, E. *J. Phys. Chem. C* **2019**, *123* (46), 28511–28512.

- (179) Parolo, C.; de la Escosura-Muñiz, A.; Merkoçi, A. *Biosens. Bioelectron.* **2013**, *40* (1), 412–416.
- (180) Cho, I. H.; Bhunia, A.; Irudayaraj, J. *Int. J. Food Microbiol.* **2015**, *206*, 60–66.
- (181) Duan, D.; Fan, K.; Zhang, D.; Tan, S.; Liang, M.; Liu, Y.; Zhang, J.; Zhang, P.; Liu, W.; Qiu, X.; Kobinger, G. P.; Fu Gao, G.; Yan, X. *Biosens. Bioelectron.* **2015**, *74*, 134–141.
- (182) Cheng, N.; Song, Y.; Zeinhom, M. M. A.; Chang, Y.-C.; Sheng, L.; Li, H.; Du, D.; Li, L.; Zhu, M.-J.; Luo, Y.; Xu, W.; Lin, Y. *ACS Appl. Mater. Interfaces* **2017**, *9* (46), 40671–40680.
- (183) Tominaga, T. *LWT* **2017**, *86*, 566–570.
- (184) Panferov, V. G.; Safenkova, I. V.; Zherdev, A. V.; Dzantiev, B. B. *Microchim. Acta* **2018**, *185* (11), 506.
- (185) Zhang, Y. *High-Entropy Materials*; Springer Singapore: Singapore, **2019**; Vol. 113.
- (186) Miracle, D. B.; Senkov, O. N. *Acta Mater.* **2017**, *122*, 448–511.
- (187) Yeh, J.-W.; Chen, S.-K.; Lin, S.-J.; Gan, J.-Y.; Chin, T.-S.; Shun, T.-T.; Tsau, C.-H.; Chang, S.-Y. *Adv. Eng. Mater.* **2004**, *6* (5), 299–303.
- (188) Cantor, B.; Chang, I. T. H.; Knight, P.; Vincent, A. J. B. *Mater. Sci. Eng. A* **2004**, *375–377* (1-2 SPEC. ISS.), 213–218.
- (189) Zhang, Y.; Zuo, T. T.; Tang, Z.; Gao, M. C.; Dahmen, K. A.; Liaw, P. K.; Lu, Z. P. *Prog. Mater. Sci.* **2014**, *61* (November 2013), 1–93.
- (190) Zhang, W.; Liaw, P. K.; Zhang, Y. *Sci. China Mater.* **2018**, *61* (1), 2–22.
- (191) Gao, M. C.; Miracle, D. B.; Maurice, D.; Yan, X.; Zhang, Y.; Hawk, J. A. *J. Mater. Res.* **2018**, *33* (19), 3138–3155.
- (192) Rost, C. M.; Sachet, E.; Borman, T.; Moballegh, A.; Dickey, E. C.; Hou, D.; Jones, J. L.; Curtarolo, S.; Maria, J.-P. *Nat. Commun.* **2015**, *6* (1), 8485.
- (193) Sarkar, A.; Breitung, B.; Hahn, H. *Scr. Mater.* **2020**, *187*, 43–48.
- (194) Afolabi, A. E.; Popoola, A. P. I.; Popoola, O. M. In *Handbook of Nanomaterials and Nanocomposites for Energy and Environmental Applications*; Springer International Publishing: Cham, **2020**; pp 1–27.
- (195) Chikumba, S.; Rao, V. V. *High Entropy Alloys: Development and Applications* **2015**, 1–5. DOI: 10.15242/IIE.E1115005

- (196) Gludovatz, B.; Hohenwarther, A.; Catoor, D.; Chang, E. H.; George, E. P.; Ritchie, R. O. *Science* **2014**, *345* (6201), 1153–1158.
- (197) Egami, T.; Guo, W.; Rack, P. D.; Nagase, T. *Metall. Mater. Trans. A* **2014**, *45* (1), 180–183.
- (198) Nagase, T.; Rack, P. D.; Noh, J. H.; Egami, T. *Intermetallics* **2015**, *59*, 32–42.
- (199) Chang, S.-Y.; Chen, M.-K.; Chen, D.-S. *J. Electrochem. Soc.* **2009**, *156* (5), G37.
- (200) Li, J.; Huang, Y.; Meng, X.; Xie, Y. *Adv. Eng. Mater.* **2019**, *1900343* (92), 1–27.
- (201) Meghwal, A.; Anupam, A.; Murty, B. S.; Berndt, C. C.; Kottada, R. S.; Ang, A. S. M. *J. Therm. Spray Technol.* **2020**, *29* (5), 857–893.
- (202) Deng, Z.; Olvera, A.; Casamento, J.; Lopez, J. S.; Williams, L.; Lu, R.; Shi, G.; Poudeu, P. F. P.; Kioupakis, E. *Chem. Mater.* **2020**, *32* (14), 6070–6077.
- (203) Wang, X.; Guo, W.; Fu, Y. *J. Mater. Chem. A* **2021**, *9* (2), 663–701.
- (204) Shukunami, Y.; Yamashita, A.; Goto, Y.; Mizuguchi, Y. *Phys. C Supercond. its Appl.* **2020**, *572*, 1–13.
- (205) Sarkar, A.; Velasco, L.; Wang, D.; Wang, Q.; Talasila, G.; de Biasi, L.; Kübel, C.; Brezesinski, T.; Bhattacharya, S. S.; Hahn, H.; Breitung, B. *Nat. Commun.* **2018**, *9* (1), 3400.
- (206) Wang, Q.; Sarkar, A.; Li, Z.; Lu, Y.; Velasco, L.; Bhattacharya, S. S.; Brezesinski, T.; Hahn, H.; Breitung, B. *Electrochem. commun.* **2019**, *100* (January), 121–125.
- (207) Wang, Q.; Sarkar, A.; Wang, D.; Velasco, L.; Azmi, R.; Bhattacharya, S. S.; Bergfeldt, T.; Düvel, A.; Heitjans, P.; Brezesinski, T.; Hahn, H.; Breitung, B. *Energy Environ. Sci.* **2019**, *12* (8), 2433–2442.
- (208) Tomboc, G. M.; Kwon, T.; Joo, J.; Lee, K. *J. Mater. Chem. A* **2020**, *8* (30), 14844–14862.
- (209) Tsai, C. F.; Yeh, K. Y.; Wu, P. W.; Hsieh, Y. F.; Lin, P. *J. Alloys Compd.* **2009**, *478* (1–2), 868–871.
- (210) Wang, A. L.; Wan, H. C.; Xu, H.; Tong, Y. X.; Li, G. R. *Electrochim. Acta* **2014**, *127*, 448–453.
- (211) Chen, X.; Si, C.; Gao, Y.; Frenzel, J.; Sun, J.; Eggeler, G.; Zhang, Z. *J. Power Sources* **2015**, *273*, 324–332.

- (212) Yusenkov, K. V.; Riva, S.; Carvalho, P. A.; Yusenkov, M. V.; Arnaboldi, S.; Sukhikh, A. S.; Hanfland, M.; Gromilov, S. A. *Scr. Mater.* **2017**, *138*, 22–27.
- (213) Zhang, G.; Ming, K.; Kang, J.; Huang, Q.; Zhang, Z.; Zheng, X.; Bi, X. *Electrochim. Acta* **2018**, *279*, 19–23.
- (214) Jia, Z.; Yang, T.; Sun, L.; Zhao, Y.; Li, W.; Luan, J.; Lyu, F.; Zhang, L. C.; Kruzic, J. J.; Kai, J. J.; Huang, J. C.; Lu, J.; Liu, C. T. *Adv. Mater.* **2020**, *32* (21), 1–9.
- (215) Jin, Z.; Lv, J.; Jia, H.; Liu, W.; Li, H.; Chen, Z.; Lin, X.; Xie, G.; Liu, X.; Sun, S.; Qiu, H. J. *Small* **2019**, *15* (47), 1–7.
- (216) Waag, F.; Li, Y.; Ziefuß, A. R.; Bertin, E.; Kamp, M.; Duppel, V.; Marzun, G.; Kienle, L.; Barcikowski, S.; Gökce, B. *RSC Adv.* **2019**, *9* (32), 18547–18558.
- (217) Huang, K.; Zhang, B.; Wu, J.; Zhang, T.; Peng, D.; Cao, X.; Zhang, Z.; Li, Z.; Huang, Y. *J. Mater. Chem. A* **2020**, *8* (24), 11938–11947.
- (218) Qiu, H. J.; Fang, G.; Wen, Y.; Liu, P.; Xie, G.; Liu, X.; Sun, S. *J. Mater. Chem. A* **2019**, *7* (11), 6499–6506.
- (219) Li, S.; Tang, X.; Jia, H.; Li, H.; Xie, G.; Liu, X.; Lin, X.; Qiu, H. J. *J. Catal.* **2020**, *383*, 164–171.
- (220) Yao, Y.; Huang, Z.; Xie, P.; Lacey, S. D.; Jacob, R. J.; Xie, H.; Chen, F.; Nie, A.; Pu, T.; Rehwoldt, M.; Yu, D.; Zachariah, M. R.; Wang, C.; Shahbazian-Yassar, R.; Li, J.; Hu, L. *Science* **2018**, *359* (6383), 1489–1494.
- (221) Xie, P.; Yao, Y.; Huang, Z.; Liu, Z.; Zhang, J.; Li, T.; Wang, G.; Shahbazian-Yassar, R.; Hu, L.; Wang, C. *Nat. Commun.* **2019**, *10* (1), 1–12.
- (222) Nellaiappan, S.; Katiyar, N. K.; Kumar, R.; Parui, A.; Malviya, K. D.; Pradeep, K. G.; Singh, A. K.; Sharma, S.; Tiwary, C. S.; Biswas, K. *ACS Catal.* **2020**, *10* (6), 3658–3663.
- (223) Kaźmierczak-Barańska, J.; Boguszevska, K.; Adamus-Grabicka, A.; Karwowski, B. T. *Nutrients* **2020**, *12* (5), 1501.
- (224) An, Q.; Sun, C.; Li, D.; Xu, K.; Guo, J.; Wang, C. *ACS Appl. Mater. Interfaces* **2013**, *5* (24), 13248–13257.
- (225) Zhang, Y.; Wang, F.; Liu, C.; Wang, Z.; Kang, L.; Huang, Y.; Dong, K.; Ren, J.; Qu, X. *ACS Nano* **2018**, *12* (1), 651–661.
- (226) Tao, Y.; Ju, E.; Ren, J.; Qu, X. *Adv. Mater.* **2015**, *27* (6), 1097–1104.

- (227) Boukhenouna, S.; Wilson, M. A.; Bahmed, K.; Kosmider, B. *Oxid. Med. Cell. Longev.* **2018**, *2018*, 1–9.
- (228) Kunjiappan, S.; Bhattacharjee, C.; Chowdhury, R. *Vitr. Cell. Dev. Biol. - Anim.* **2015**, *51* (6), 630–643.
- (229) Manickam, D. S.; Brynskikh, A. M.; Kopanic, J. L.; Sorgen, P. L.; Klyachko, N. L.; Batrakova, E. V.; Bronich, T. K.; Kabanov, A. V. *J. Control. Release* **2012**, *162* (3), 636–645.
- (230) Dashtestani, F.; Ghourchian, H.; Najafi, A. *Mater. Sci. Eng. C* **2019**, *94*, 831–840.
- (231) Kim, M.; Kim, M. S.; Kweon, S. H.; Jeong, S.; Kang, M. H.; Kim, M. Il; Lee, J.; Doh, J. *Adv. Healthc. Mater.* **2015**, *4* (9), 1311–1316.
- (232) Löffler, T.; Meyer, H.; Savan, A.; Wilde, P.; Garzón Manjón, A.; Chen, Y.-T.; Ventosa, E.; Scheu, C.; Ludwig, A.; Schuhmann, W. *Adv. Energy Mater.* **2018**, *8* (34), 1802269.
- (233) Hagen, J. In *Technische Katalyse*; VCH Verlagsgesellschaft mbH: Weinheim, Germany, **1996**; 96.
- (234) Potapova, E. *Adsorption of Surfactants and Polymers on Iron Oxides: Implications For Flotation and Agglomeration of Iron Ore*, Ph.D. Dissertation, Lulea University of Technology, Lulea, SE, **2011**.
- (235) Zhang, S.; Yang, J.; Lin, J. *Bioelectrochemistry* **2008**, *72* (1), 47–52.
- (236) Josephy, P. D.; Eling, T.; Mason, R. P. *J. Biol. Chem.* **1982**, *257* (7), 3669–3675.
- (237) Rodríguez-López, J. N.; Lowe, D. J.; Hernández-Ruiz, J.; Hiner, A. N. P.; García-Cánovas, F.; Thorneley, R. N. F. *J. Am. Chem. Soc.* **2001**, *123* (48), 11838–11847.
- (238) Costa, R. C. C.; Lelis, M. F. F.; Oliveira, L. C. A.; Fabris, J. D.; Ardisson, J. D.; Rios, R. R. V. A.; Silva, C. N.; Lago, R. M. *J. Hazard. Mater.* **2006**, *129* (1–3), 171–178.
- (239) Fischer, B. E.; Haring, U. K.; Tribolet, R.; Sigel, H. *Eur. J. Biochem.* **1979**, *94* (2), 523–530.
- (240) Gupta, B. S.; Taha, M.; Lee, M. J. *J. Solution Chem.* **2013**, *42* (12), 2296–2309.
- (241) Robbins, M. H.; Drago, R. S. *J. Catal.* **1997**, *170* (2), 295–303.

Acknowledgements

My highest gratitude goes to my supervisor Prof. Dr. Lea Ann Dailey and her husband Dr. Richard Harvey. They both created a working environment, that was a huge pleasure to experience, not only at work, but in various spare-time activities, as well. Prof. Dr. Lea Ann Dailey furthermore provided help with funding proposals, creative ideas, interesting scientific talk and knowledge on structuring research, to help me advance as a researcher. Thank you very much for the great time.

I would like to acknowledge Prof. Dr. Karsten Mäder, for providing cooperation with his group, help with proposals, valuable feedback and nice working atmosphere, in general.

I would also like to thank all past and present members of the biopharmacy and pharmaceutical technology groups for the wonderful cooperation and working environment. Special thanks go to Paul Robert Neumann, with whom I had pleasurable times in lab and office, as well as lots of fruitful conversations.

I would further like to thank the team of Dr. Dieter Ströhl for running the NMR experiments, Kerstin Schwarz for DSC measurements and Dr. Anette Meister for recording the TEM pictures.

Dr. Laura Urbano shared her experience with Si-NP production and Prof. Dr. Yang-Hsiang Chan shared his experience with Pdot conjugation. Thank you very much.

The work on eLFI was an exciting addition to the research and I would therefore like to express my gratitude towards Dr. Ben Breitung and his research group at the Karlsruhe Institute of Technology for the cooperation, specifically for providing the MCM and HEN samples and the fruitful scientific conversations and insights.

I would also like to thank all my friends for a wonderful compensation for work during spare time.

Finally, I would like to thank my Family for an amazing childhood and ongoing support and joy. I love you.

Curriculum vitae

Personal Details

Name: Moritz Schüller
Date of birth: 10.04.1991
Place of birth: Dresden

Education

since 06/2016 PhD student in the group of Prof. Dr. Lea Ann Dailey
Department of Pharmaceutical Technology and Biopharmaceutics
Martin-Luther-Universität Halle-Wittenberg

10.2013 – 01.2016 Master studies in chemistry
Martin-Luther-Universität Halle-Wittenberg
Specialisation in macromolecular chemistry
Thesis on topic “Reactive components for self-healing polymers”

10.2009 – 11.2013 Bachelor studies in chemistry
Martin-Luther-Universität Halle-Wittenberg
Thesis on topic “Synthesis of trivalent polyisobutylene-ionic liquids”

08.2001 – 06.2009 Abitur
Humboldt-Gymnasium Radeberg

Publications

Schüller, M.; Meister, A.; Green, M.; Dailey, L.A. *RSC Adv.*, **2021**, 11, 29816–29825.

Modicano, P.; Neumann, P. R.; Schüller, M.; Holthof, J.; Kyrilis, F. L.; Hamdi, F.; Kastritis, P. L.; Mäder, K.; Dailey, L. A. *Eur. J. Pharm. Biopharm.* **2020**, 154 (July), 297–308.

Declaration of Authorship

I hereby declare that I created this thesis unaided on my own and did not use sources other than listed in the reference section. I further declare that content, that was directly or indirectly used from these sources was appropriately marked as such.

This thesis was neither published, nor submitted to another institution before and is my first attempt to receive a doctorate.

Halle (Saale), _____

Moritz Schüller